UNIVERSITY OF CALIFORNIA

Los Angeles

The Askar'yan Effect and Detection of Extremely High Energy Neutrinos in the Lunar Regolith and Salt

A dissertation submitted in partial satisfaction

of the requirements for the degree

Doctor of Philosophy in Astronomy

by

Dawn Renee Williams

2004

The dissertation of Dawn Renee Williams is approved.

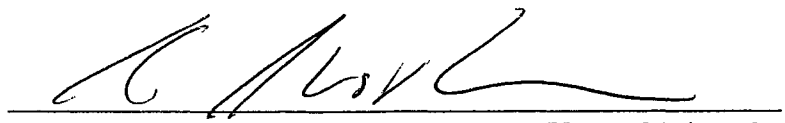

Katsushi Arisaka

Alex Kusenko

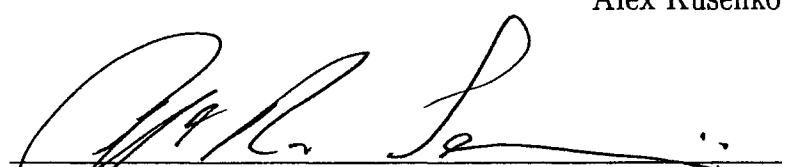

Yahya Rahmat-Samii

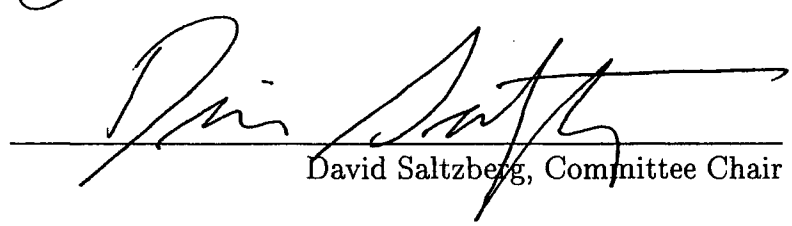

David Saltzberg, Committee Chair

University of California, Los Angeles

2004

To Mom and Dad, your children rise up and call you blessed. I love you both.

Table of Contents

List of Figures

List of Tables

ACKNOWLEDGMENTS

This dissertation would never have been written without the unfailing support and encouragement of my advisor, David Saltzberg.

Chapter 2 (the SLAC beamtest in sand) is a version of a paper co-written by Peter Gorham, David Saltzberg, Dieter Walz, Clive Field, Richard Iverson, Allen Odian, the late George Resch, and Paul Schoessow (Phys.Rev.Lett. 86, 2802-2805, 2001). For the SLAC beamtests, thanks also go to Tom Berger, Dave Besson, Radovan Milincic, Mike Spencer, and the staff at SLAC. For the transition radiation measurements (chapter 3), thanks to Clive Field for shower simulations. For the Argonne beamtest (chapter 3), thanks to Tom Berger, Manoel Conde, Wei Gai, Peter Gorham, Nikolai Lehtinen, and the staff at Argonne National Laboratory.

Chapter 4 (the Goldstone experiment) contains a version of a paper co-authored by Peter Gorham, Christina Hebert, Kurt Liewer, Chuck Naudet, and David Saltzberg (astro-ph/0310232, submitted to Phys. Rev. Lett.) For the Goldstone experiment, thanks also go to M. Klein, T. Kuiper, Radovan Milincic, and the staff at Goldstone Deep Space Tracking Station. For the GLUE calibration and Monte Carlo calculations in chapter 4, thanks to Dave Besson, Amy Connolly, Jay Hauser, Christina Hebert, Kurt Liewer, Joshua Meyers, Dave Seckel and Jean Turner. For the CELENE proposal, thanks to the GLUE team, Ron Ekers, Tim Hankins, Rava Subramanyan, and the Australia National Telescope Facility.

Chapter 5 (salt neutrino detector studies) contains a version of a paper co-authored by Peter Gorham, David Saltzberg, Allen Odian, David Besson, George Frichter, and Sami Tantawi (Nucl. Instrum. Meth., A490, 476 (2002)). For the

salt formation tests, thanks also go to Ray Carrasco and the staff at the Waste Isolation Pilot Plant, and the staff at the Hockley Salt Mine. For the salt Monte Carlo, thanks to Jaime Alvarez-Muniz, Amy Connolly, Dave Seckel.

This work was supported in part by DOE contract DE-FG03-91ER40662 at UCLA.

VITA

1978	Born in Tarzana, CA.
1995	Resident Honors Program and Trustee Scholarship Award, USC.
1999	BS in Astronomy, USC.
1999	Chancellor Fellowship, UCLA.
1999	Teaching Assistant in the Department of Astronomy, UCLA.
2001	MS in Astronomy, UCLA.
2001	Teaching Assistant in the Department of Physics, UCLA.
2003	Teaching Assistant in the Department of Physics, UCLA.

PUBLICATIONS

P. W. Gorham, K. M. Liewer, C. J. Naudet (JPL) ; D. P. Saltzberg, D. R. Williams (UCLA): *Radio limits on an isotropic flux of > 100 EeV cosmic neutrinos*, presented at the First International Workshop on Radio Detection of High Energy Particles (RADHEP 2000), Nov. 16-18, 2000, AIP Conference Proceedings #579, astro-ph/0102435.

David Saltzberg, Peter Gorham, Dieter Walz, Clive Field, Richard Iverson, Allen Odian, George Resch, Paul Schoessow, and Dawn Williams: *Observation of the Askaryan Effect: Coherent Microwave Cherenkov Emission from Charge Asymmetry in High Energy Particle Cascades*, hep-ex/0011001, Phys.Rev.Lett. 86, 2802-2805 (2001).

Peter Gorham, David Saltzberg, Allen Odian, Dawn Williams, David Besson, George Frichter, Sami Tantawi: *Measurements of the Suitability of Large Rock Salt Formations for Radio Detection of High Energy Neutrinos*, hep-ex/0108027, Nucl. Instrum. Meth., A490, 476 (2002).

P. Gorham, K. Liewer, R. Milincic, C. Naudet, D. Saltzberg, D. Williams: *Status of Goldstone Lunar Ultra-High Energy Neutrino Experiment*, SPIE Proceedings vol. 4858, 2002.

D. Saltzberg, D. Besson, P. Gorham, A. Odian, R. Milincic, D. Williams: *Monte Carlo Design Studies for a Next-Generation UHE Observatory Located in a Large Rock Salt Formation*, SPIE Proceedings vol. 4858, 2002.

P. W. Gorham, C. L. Hebert, K. M. Liewer, C. J. Naudet, D. Saltzberg, D. Williams: *Experimental Limit on the Cosmic Diffuse Ultra-high Energy Neutrino Flux* astro-ph/0310232, submitted to Phys. Rev. Lett., 2003.

ABSTRACT OF THE DISSERTATION

The Askar'yan Effect and Detection of Extremely High Energy Neutrinos in the Lunar Regolith and Salt

by

Dawn Renee Williams

Doctor of Philosophy in Astronomy

University of California, Los Angeles, 2004

Professor David Saltzberg, Chair

The origin of the highest energy cosmic rays is an ongoing puzzle in particle astrophysics. Most models for the production of these cosmic rays also predict a flux of extremely high energy (EHE) neutrinos. Gurgen Askar'yan proposed an effect whereby EHE neutrinos could be detected in the radio frequencies. In this dissertation I present the results of beamtests at the Stanford Linear Accelerator Center (SLAC) demonstrating the properties of the Askar'yan effect. I then describe the Goldstone Lunar Ultra-high energy neutrino Experiment (GLUE) which searches for radio pulses from EHE neutrinos in the lunar regolith. The experiment sees no signals consistent with EHE neutrinos in 123 hours of livetime, and sets an upper limit on EHE neutrinos from topological defects models. I also describe concept studies for a possible radio neutrino detector in a salt formation, which could detect neutrinos from EHE cosmic rays interacting with the cosmic microwave background.

CHAPTER 1

Introduction

1.1 The Highest Energy Messengers

In the past century, photon astronomy has been extended out of the optical range from radio to gamma ray energies. However, as their energy increases, gamma rays will interact with the infrared (IR) background via pair production, $\gamma + \gamma \rightarrow e^+e^-$ [1]. The absorption length at $E_\gamma = 80$ TeV constrains the gamma ray source to be within tens of Mpc of Earth.

Cosmic rays are another source of information from the Universe. Victor Hess discovered cosmic rays in 1912 in balloon-flight measurements. Cosmic rays include protons and higher-Z atomic nuclei as well as electrons and positrons. The energy of the cosmic ray spectrum also extends much higher than the ~100 TeV limit on gamma rays. Figure 1.1 shows the observed differential energy spectrum of cosmic rays, which obeys a broken power law: $dN/dE \propto E^{-\alpha}$ above 10 GeV. The spectral index $\alpha = 2.7$ below 10^{16} eV and $\alpha = 3.0$ from 10^{16} to 10^{18} eV [1]. Above 10^{18} eV, the spectral index is uncertain because of low statistics, but cosmic rays have been observed with energies higher than 10^{19}eV.

In addition to being the highest energy messengers in astronomy, cosmic rays have been important in the history of particle physics. The muon, the pion, the positron and particles containing strange quarks were first discovered in air showers induced by cosmic rays. Later, accelerators took over the study of particle

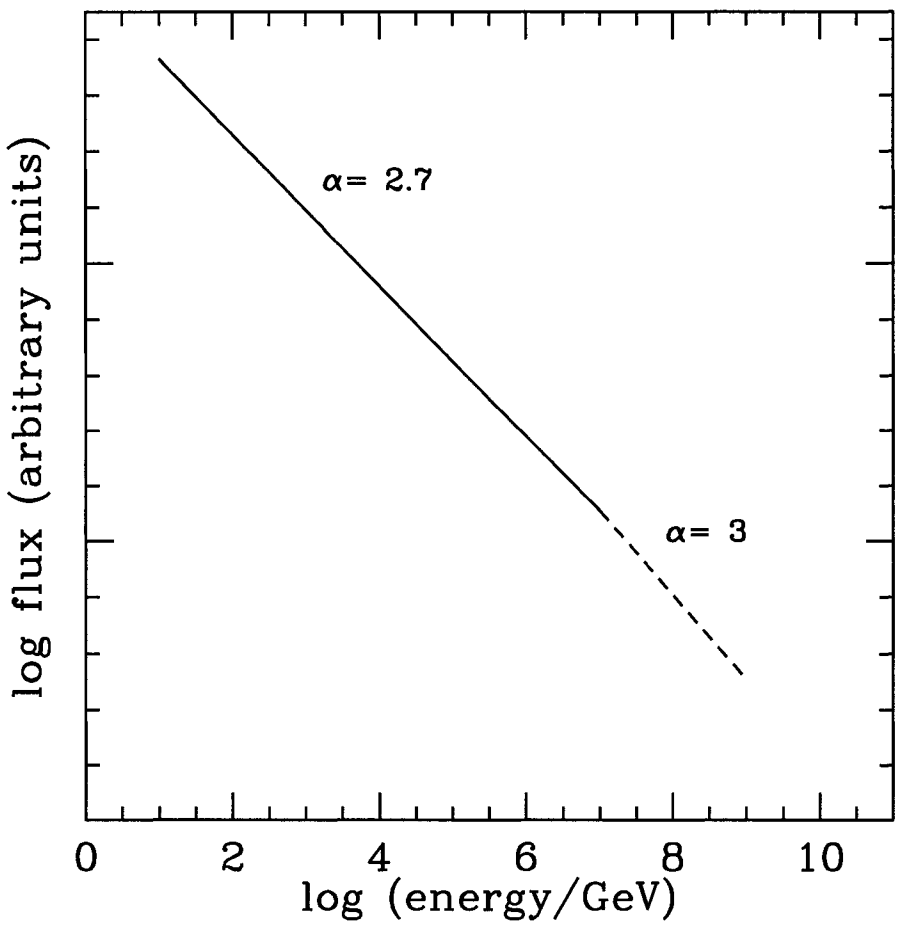

Figure 1.1: The differential energy spectrum [1] of cosmic ray nuclei, based on data from S. Swordy.

interaction. However, accelerators can only achieve beam energies up to ~2 TeV. Therefore cosmic rays are the sources of the highest energy particles.

1.2 The Highest Energy Cosmic Rays

The origin of cosmic rays with energies beyond 10^{15} eV is unknown. Supernova shocks should be able to accelerate particles via the first-order Fermi process, which is an attractive model because it naturally produces the power-law spectrum [2] seen in Figure 1.1. However, the maximum energy from the Fermi process goes linearly with the size and magnetic field of the region. Based on these parameters, supernova remnants should not be able to accelerate particles to energies beyond about 10^{15} eV. Acceleration beyond this energy requires a more energetic astrophysical source, or possibly new physics. Models for extremely high energy (EHE) cosmic-ray production fall into two classes: bottom-up models in which particles are accelerated from a lower energy, and top-down models in which particles decay from a higher energy.

1.2.1 Bottom-up Models: Active Galactic Nuclei

Active galactic nuclei (AGN) are extremely luminous, up to 10^{47} erg/s. The favored model for the central engine of an AGN is a supermassive black hole ($M \sim 10^9 M_\odot$) with a disk of matter accreting onto the black hole [1]. The core of the AGN may be able to accelerate particles to high energies, but the dense environment of the core would prevent particles from escaping. In the radio, AGNs also have nonthermal jets which probably result from synchrotron emission of electrons accelerated along the jet axis, perpendicular to the accretion disk. When an AGN jet is aligned along the line of sight to Earth, it is called a

blazar. Recently, blazars have been observed in gamma rays [3]. These gamma rays may be produced by inverse Compton scattering of low energy photons on jet-accelerated electrons, or by pion decay ($\pi^0 \longrightarrow \gamma\gamma$) resulting from shock acceleration of protons [4].

1.2.2 Bottom-up Models: Gamma-Ray Bursts

Satellites monitoring nuclear weapons testing discovered rapid flares of gamma rays coming from all directions in the 1960s [1]. The Burst And Transient Source Experiment detector aboard the Compton Gamma Ray Observatory discovered that gamma-ray bursts (GRBs) were distributed isotropically [5], and a later optical observation indicated that GRBs originate at cosmological distances [6]. The luminosity of a GRB is as high as 10^{52} erg/s. The mechanism for the generation of these bursts is unknown, but Stanek *et al.* recently observed a supernova signature in the optical afterglow of a GRB [7]. If GRBs result from the collapse of supermassive stars, they may produce extremely energetic shock waves, which may accelerate particles to even higher energies than supernovae.

1.2.3 Top-down Models

So-called "X particles", with energies much higher than 10^{20} eV, occur in certain cosmological and particle physics models. Topological defects (TD) such as monopoles, cosmic strings and domain walls (or some combination of these) occur in phase transitions in the early universe, and can contain X particles. Also, X particles may be supersymmetric gauge bosons. Such particles could decay to produce EHE cosmic rays.

Astrophysical constraints from the cosmic microwave background rule out the simplest (monopole) TD models [8]. Additional constraints from the 100 MeV

gamma ray background [9] restrict X particle masses to $M_X < 10^{16}$ GeV. These constraints do not rule out more complicated and lighter-mass models [10].

1.2.4 Comparison of the Two Classes of Models

Top-down models require physics beyond the Standard Model and their predictions are model-dependent; however, there are many other motivations for such physics. Acceleration models do not require new physics, but it is difficult to accelerate particles to the highest energies in the cosmic ray spectrum for reasonable assumptions about even extreme astrophysical environments, which are also model dependent. Another difficulty with bottom-up models comes from the Greisen-Zatsepin-Kuzmin (GZK) limit.

Most energetic cosmic ray particles lose energy as they travel due to interaction with the 2.73 K cosmic microwave background (CMB). The GZK cutoff [11] is about 5×10^{19} eV. Above this energy, a cosmic ray will not be able to travel more than about 50 to 100 Mpc before losing excess energy to the CMB. The dominant interactions are:

1) photopair production: $p_{CR}\gamma_{CMB} \longrightarrow pe^+e^-$

2) photoproduction of pions: $N_{CR}\gamma_{CMB} \longrightarrow N\pi$ where N is a neutron or proton.

No astrophysical sources such as AGNs or GRBs exist within 50 Mpc of Earth, which tends to favor top-down models if the GZK cutoff is not observed. The experimental evidence for the GZK cutoff is not certain at this time. The HiRes and AGASA experiments disagree about whether the cutoff is seen [12], and the statistics are too low and the systematic errors too large to be certain. The Auger experiment [13] will measure the EHE cosmic ray spectrum with better statistical precision and better control of systematic errors.

1.3 EHE Neutrinos

Only two astronomical sources have been observed in neutrinos: the Sun and Supernova 1987A in the Large Magellanic Cloud. However, most models for the production of the EHE cosmic rays also predict a flux of EHE neutrinos.

As discussed above, the observed flux of gamma rays from AGN blazars may result from proton acceleration, rather than electron acceleration. In that case, the protons would create neutrinos as a result of photoproduction of pions. The same process would occur if protons were accelerated in shocks associated with GRBs. Waxman and Bahcall (WB) [14] have set an upper limit on EHE neutrinos from astrophysical sources, assuming that all neutrinos are produced in regions optically thin to protons, in which case the protons are also responsible for the observed EHE cosmic ray flux. Higher neutrino fluxes can be obtained from optically thick regions, but in this case the protons would not contribute to the EHE cosmic ray flux and the WB bound does not apply. Topological defect models [15] for cosmic rays produce much higher fluxes of neutrinos (compared to protons) than astrophysical models. These models are not subject to the WB bound.

Another source of neutrinos is the GZK process itself, which is the only "guaranteed" flux of EHE neutrinos. Assuming that EHE cosmic rays come from astrophysical sources, Engel *et al.* [16] propagate EHE protons through the cosmic ray background and calculate the resulting neutrino fluxes from photoproduction of pions.

Figure 1.2 shows the predicted neutrino spectra from the WB bound [14], two TD models [15] and the GZK flux [16]. Neutrinos have several advantages over cosmic rays as sources of astronomical information. They are electrically

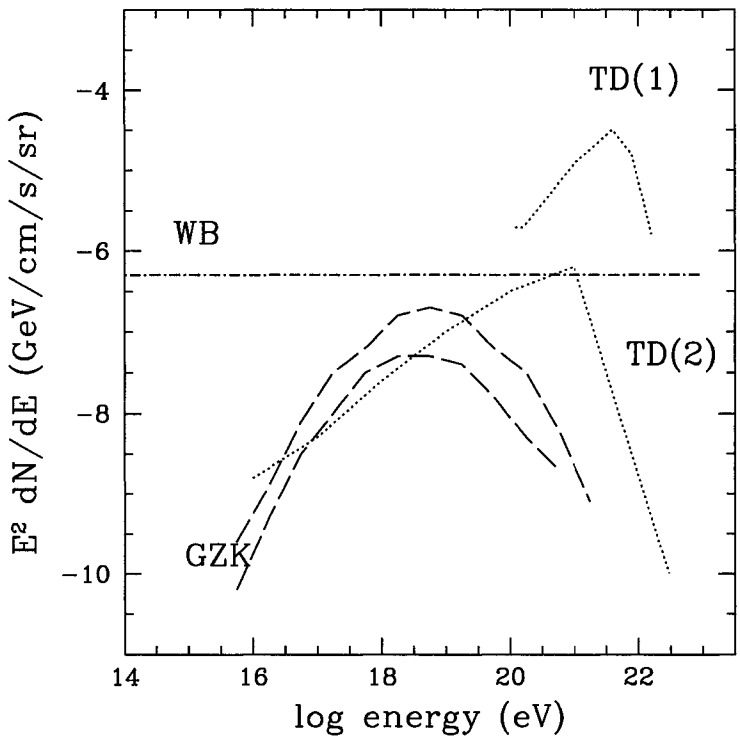

Figure 1.2: Fluxes of neutrinos from topological defects (dotted) [15], GZK (dashed) [16] and the WB upper bound (dots and dashes) [14].

neutral, so they point back to their sources, whereas all but the highest energy ($E \sim 10^{20}$ eV) cosmic rays are bent in intergalactic magnetic fields. Since they only interact weakly, neutrinos do not suffer from GZK attenuation or attenuation at their sources like cosmic ray protons. And at the highest energies, neutrinos actually have very high cross sections for interaction.

The predicted fluxes from EHE neutrino models are extremely low compared to fluxes of solar or atmospheric neutrinos. Figure 1.3 compares fluxes and cross sections for 10 MeV ^{8}B solar neutrinos at SNO [17], 1 GeV atmospheric neutrinos at Super-Kamiokande [18], and GZK neutrinos at 10^{18} eV [16], using the cross section from Gandhi *et al.* [19]. Although the cross section of a GZK neutrino is more than 10 orders of magnitude higher than the cross section for solar neutrinos, the flux is more than 20 orders of magnitude lower. Such low fluxes require a cubic kilometer or larger scale detector, which is too large to build. Therefore a neutrino telescope requires a large natural volume which is transparent to the radiation produced in the neutrino interaction.

Most cosmic-ray experiments use Cherenkov radiation to detect EHE particles. A particle traveling through a medium at a speed greater than the speed of light in that medium produces Cherenkov radiation. It propagates in a cone with a half-angle θ_c where $\cos(\theta_c) = n\beta^{-1}$, n is the index of refraction and $\beta = v/c$. The Cherenkov radiation power spectrum goes as $dP \propto \nu d\nu$, producing an equal number of photons per unit bandwidth. Therefore most detectors search for optical Cherenkov radiation, since the frequency and bandwidth in the optical regime are much larger than in the radio. Water, air and ice, which are optically transparent and occur in large volumes in nature, are used in optical Cherenkov searches for EHE neutrinos. The Auger experiment, an air-shower experiment which is primarily sensitive to cosmic rays, may be sensitive to tau neutrinos

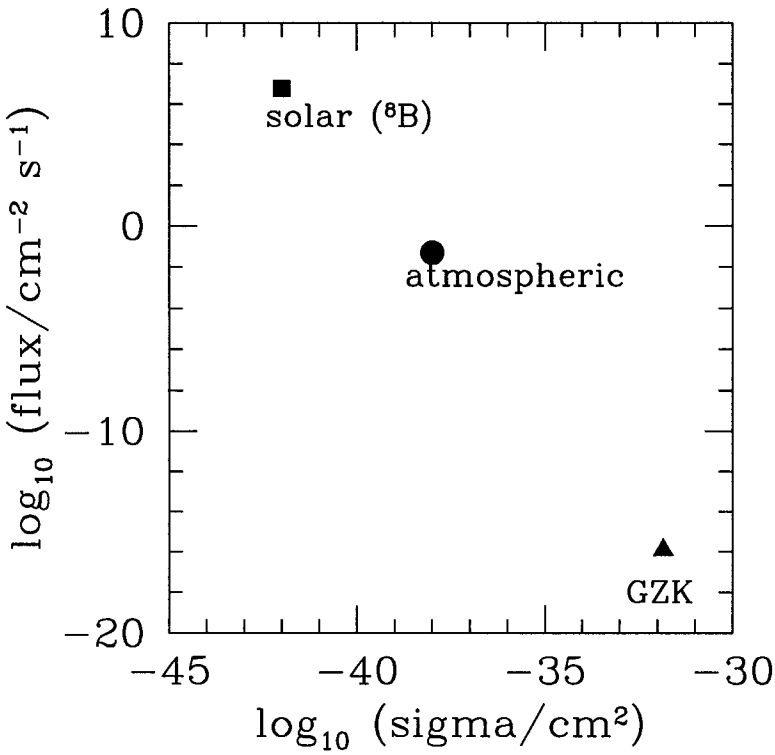

Figure 1.3: Cross sections and predicted fluxes for solar neutrinos at SNO [17], atmospheric neutrinos at Super-Kamiokande [18] and GZK neutrinos [16, 19].

producing up-going air showers [21]. The Antares experiment [20] is deploying strings of photomultiplier tubes (PMTs) in the Mediterranean to search for EHE neutrinos in the water. The AMANDA experiment [22] and its proposed extension IceCube [23] deploy PMTs in the Antarctic ice sheet.

In conclusion, detection of EHE neutrinos has the potential to provide information concerning extreme astrophysical environments, physics beyond the standard model, cosmology, and the origin of the highest energy cosmic rays. Efforts to detect optical signatures from EHE neutrinos are underway. However, there is an effect which makes it advantageous to search for radio signals as well, which is the subject of this dissertation.

CHAPTER 2

The Askar'yan Effect and the SLAC Beamtest

2.1 The Theory of Radio Detection

In 1962 G.A. Askar'yan [24] proposed an effect that would make radio detection of EHE neutrinos practicable. When a neutrino interacts with matter, its energy forms a cascade of electrons and positrons. Compton scattering, δ-ray production, and annihilation of positrons create a $\sim 20\%$ excess of electrons over positrons. Since this charge excess is traveling at essentially the speed of light in vacuum, it creates a flash of Cherenkov radiation in the dielectric medium of the target. At wavelengths much longer than the shower bunch size, this radiation is coherent; that is, its power scales as the square of the shower energy. At the highest energies, the radio emission will carry off a large fraction of the cascade energy. Askar'yan mentioned the possibility of detecting showers in solid radio-transparent dielectrics such as ice, very dry rock and salt. In particular he mentioned the outer layer of the moon (the regolith) as a potential target. For these materials the coherent regime corresponds to frequencies up to several GHz, at which these materials are transparent.

The Askar'yan effect was never unambiguously measured in air showers because of competing effects from geomagnetic dipole separation and/or synchrotron radiation [25]. In 1999, Gorham and Saltzberg *et al.* performed a beamtest of the Askar'yan effect at Argonne [26], using pulsed bunches of electrons to simulate the

charge excess. However, electrons form transition radiation when passing through an interface, which obscures the presence of Cherenkov radiation. In 2000, another beamtest took place at Stanford Linear Accelerator Center (SLAC), which directly observed the formation of the excess and the resulting Cherenkov radiation. The experiment and results are described in the following section.

2.2 SLAC Beamtest in Sand, 2000

The key to the SLAC beamtest is to use photons rather than electrons. Neutral particles do not emit transition radiation when passing through an interface. When the charge excess forms it is entirely within the target, so there should be only Cherenkov radiation. Also, the electron energy at SLAC was a factor of 100 higher than at Argonne, so many more shower particles are produced.

2.2.1 Experimental Setup

The beamtest took place at SLAC's Final Focus Test Beam (FFTB) facility in August 2000. The target was placed 30 m downstream of thin bremsstrahlung radiators providing a photon beam from 28.5 GeV electrons. When passing through the radiators, the energy lost to bremsstrahlung as a function of the distance x traveled is given by

$$E_{\text{lost}}(x) = E_0 \left[1 - \exp\left(\frac{x}{X_0}\right)\right] \tag{2.1}$$

In the case of a thin radiator ($x \ll X_0$), $E_{\text{lost}}(x) \approx \frac{E_0 x}{X_0}$. We employed radiators with $\frac{x}{X_0} = 1\%$, 2.7%, and 3.7%. The electron beam current ranged from $(0.2 - 1.0) \times 10^{10}$ electrons per bunch. Therefore the equivalent shower energy ranged from $(0.06 - 1.1) \times 10^{19}$ eV.

The target was a box containing 3200 kg of silica sand. The refractive index

and radio frequency (RF) attenuation properties of sand are similar to those of the lunar regolith. The index of refraction of dry silica sand is $n = 1.6$, corresponding to a Cherenkov angle of 51°. The target geometry is shown in Figure 2.1. The box is constructed of plywood, except for the wall through which the radiation was observed, which is made of low-loss polypropylene plastic. The polypropylene wall is slanted at an angle of 10° with respect to the beam axis to avoid total internal reflection of the Cherenkov radiation. (The angle of total internal reflection is complementary to the Cherenkov angle.) Given the geometry, reflections arrive later than the primary pulse from the beam axis. We lined the far side and the bottom of the box with microwave absorber to minimize reflections. Simulations prior to the experiment predicted that bulk of the shower would be contained upstream of 200 cm, so the box is 3.6 m long to allow for the corresponding Cherenkov radiation path.

We used standard gain S-band and C-band pyramidal horns to measure the RF pulses outside the box. We also buried six dipole antennas in the sand along the wall opposite the polypropylene wall. One of these dipoles was borrowed from the Radio Ice Cherenkov Experiment (RICE) which is currently looking for RF pulses from the Askar'yan effect in the Antarctic ice [27]. The properties of the antennas are listed in Table 2.1. The effective height of an antenna is the ratio of the voltage induced in the antenna to the incident electric field, $h_{eff} = V/E$. Note that V is the $open-circuit$ voltage, the voltage across the source with no load attached. The directivity (gain) is related to the effective area A_e of the antenna:

$$G = \frac{4\pi}{\lambda^2} A_e \tag{2.2}$$

. Typical pulses seen in the antennas are shown in Figure 2.2. The width of the pulses are approximately equal to the inverse bandwidth of the antennas,

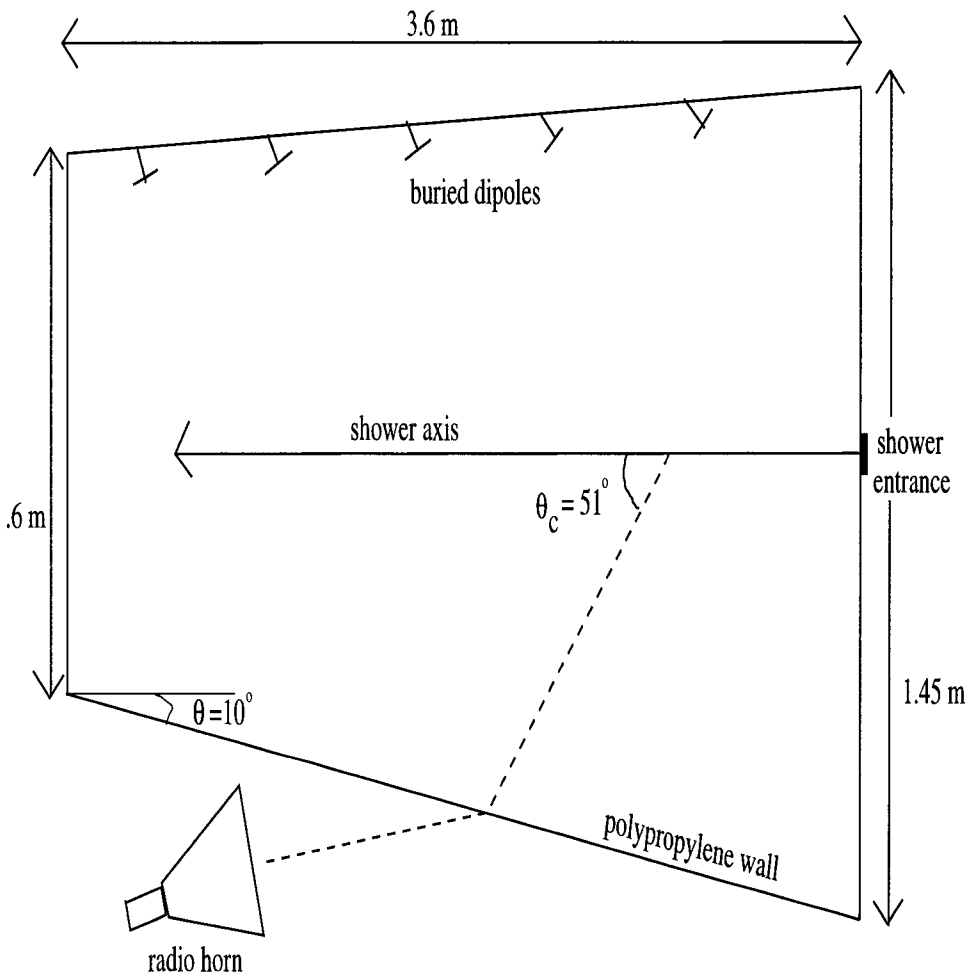

Figure 2.1: The SLAC sandbox target geometry as seen from above. Not to scale.

Table 2.1: Antenna properties

antenna type	location	frequency range	effective height	directivity
unbalanced dipole	buried	1 - 1.5 GHz	5 cm	1.5 dBi
RICE dipole	buried	0.2 - 1 GHz	10 - 36 cm	1.5 dBi
balanced dipole	buried	1 - 1.5 GHz	7 cm	1.5 dBi
S-band horn	external	1.7 - 2.6 GHz	18 cm	15.5 dBi
C-band horn	external	4.4 - 5.6 GHz	5.7 cm	14.3 dBi

meaning that the pulses are bandwidth-limited.

We used two data acquisition systems. The information from the S-band horns and the dipoles was sent via low loss heliax cable to a Tektronix 694C real-time digital sampling oscilloscope with 3 GHz bandwidth and a maximum sampling rate of 10 GSa/s. A GPIB cable connected the oscilloscope to a Sun workstation which recorded the data. A dipole placed in the electron beam dump triggered the oscilloscope. This trigger was stable to within a few picoseconds.

For the C-band horn, whose frequency range is outside the range of the 3 GHz oscilloscope, we used a Tektronix 1180 series 50 GHz bandwidth oscilloscope connected to a laptop running Labview. A dipole set in a foil tent in an airgap of an experiment well upstream of the target triggered this oscilloscope. This oscilloscope could only collect one sample at a time, so the data trace was reconstructed from many pulses.

In both cases the signals were run through variable attenuators ($0 - 50$ dB) to reduce the input pulse to less than 5 volts RMS as required by the instrument specifications. No amplification was necessary.

We measured the ambient magnetic field and found it to be of geomagnetic

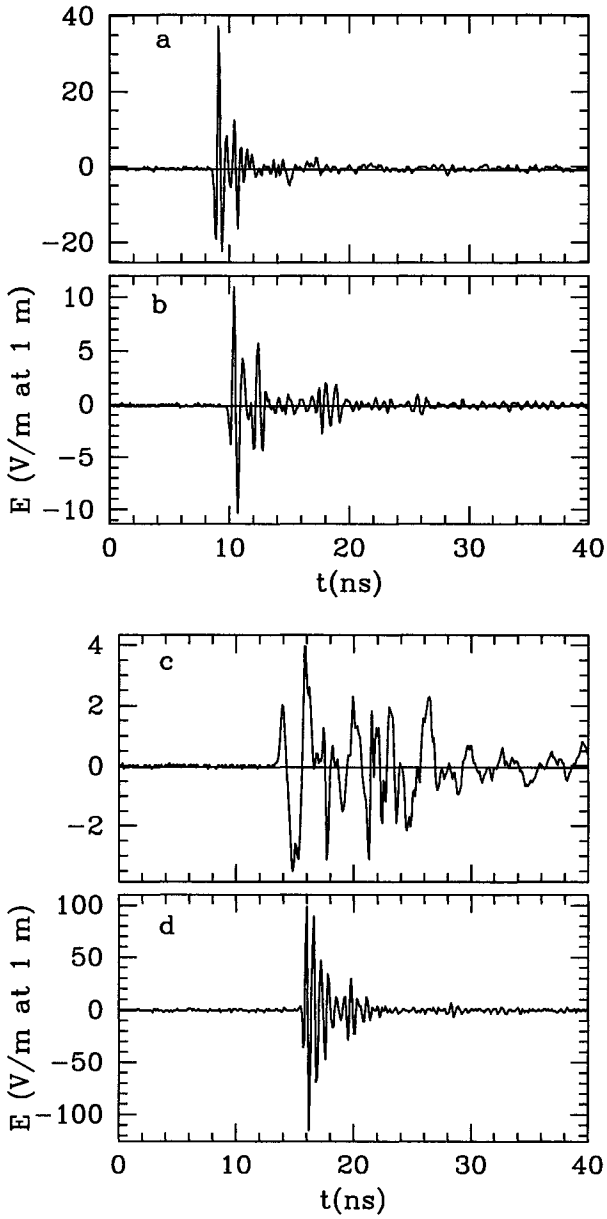

Figure 2.2: Typical antenna pulses: (a) unbalanced dipole (b) balanced dipole (c) RICE dipole (d) S-band horn.

strength, which does not induce significant charge separation in the shower. The background RF signal when the beam is run with 0% radiator is a few mV RMS, which is negligible compared to the 10 - 100 V RMS signals obtained when the radiators are in place.

By moving the horns in position along the shower axis and in angle, we measured the following properties of the shower: its development, coherence, spectral dependence, degree of linear polarization, the existence of the Cherenkov shockwave, and the behavior of the radiation around the Cherenkov angle.

2.2.2 Shower Profile

We measured the longitudinal shower profile with both the S-band and C-band horns. We placed the horns with the E-plane (flaring of the horn in the plane of the electric field) parallel to the floor, which was assumed to be the plane of polarization (later verified). The horn axis made an angle of 29° with respect to the beam axis. This corresponds to radiation emitted at the Cherenkov angle (51°) and then refracted from sand into air at an interface slanted at 10° with respect to the beam axis. Measurements were taken at 8 positions along the beam axis.

The results for the S-band horn are shown in Figure 2.3 a. The curve is the expected total number of particles in the shower with respect to the position along the shower axis [28]. The plotted points are the peak field strengths at each position, which is the center of the antenna beam refracted onto the beam axis. The C-band horn profile is shown in Figure 2.3 b. We only took five positions with this horn because the 50 GHz oscilloscope is much slower than the 3 GHz oscilloscope. The development of the shower is similar in both frequency bands.

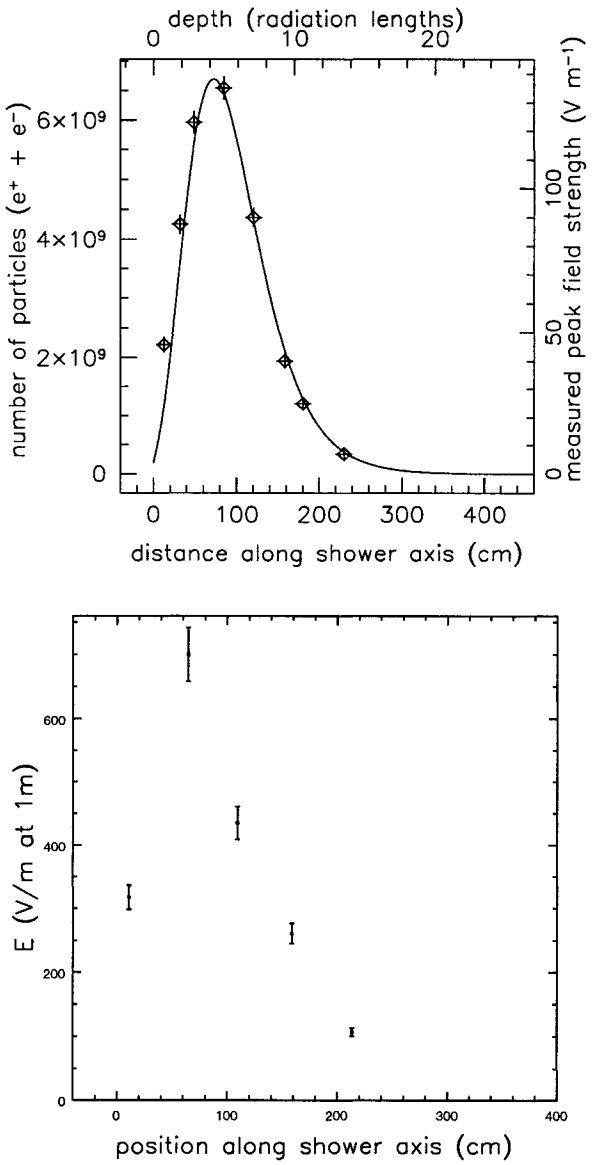

Figure 2.3: a) S-band horn profile. b) C-band horn profile.

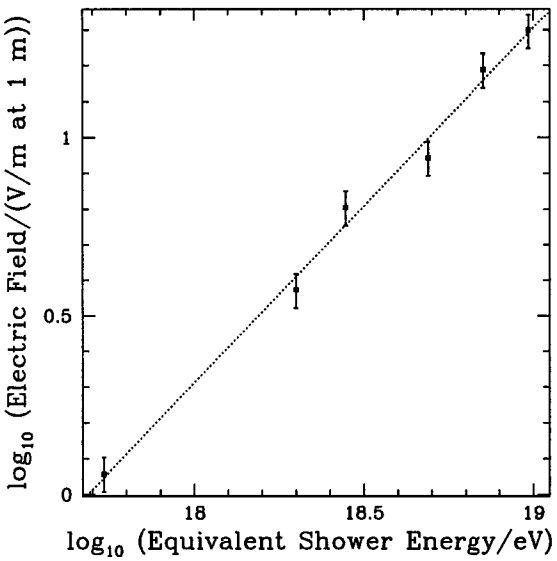

Figure 2.4: Electric field as a function of equivalent shower energy. The linear dependence means that the radiation is coherent.

2.2.3 Coherence

Figure 2.4 shows the peak field strengths as a function of the different shower energies, using different combinations of radiators and beam currents. The dotted line on the plot is a least-squares fit with a slope of $\alpha = 0.99 \pm 0.03$. Therefore the number of particles (or electric field) rises linearly with the input energy, meaning that the power in the shower rises quadratically with the input energy.

2.2.4 Spectral Dependence

Figure 2.5 shows the dependence of the peak field strengths on frequency, using different antennas. The predicted field strength as a function of frequency is [29]

$$E = \frac{A_0 K \epsilon}{R} \left(\frac{W_T}{1\text{TeV}}\right) \frac{\nu}{\nu_0} \left(\frac{1}{1 + 0.4(\frac{\nu}{\nu_0})^{\delta}}\right) (\text{Vm}^{-1}\text{MHz}^{-1}) \qquad (2.3)$$

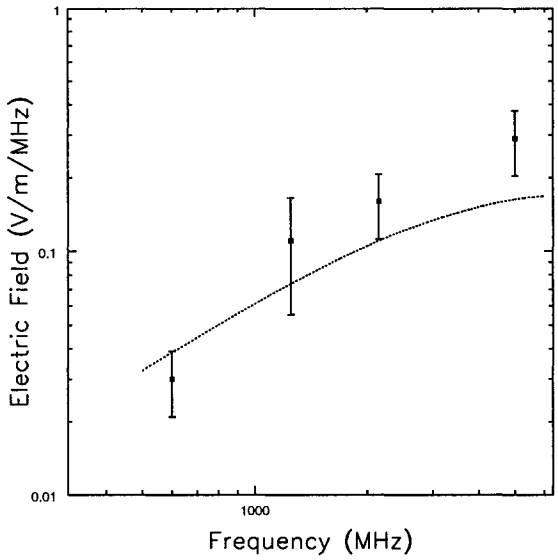

Figure 2.5: Electric field as a function of frequency. Solid line is the Monte Carlo prediction [29].

where R is the distance to the source, ν is the frequency, $\nu_0 = 2500$ MHz in sand, $W_T = N_e \eta W_e$ is the shower energy as a function of the number of electrons N_e, the thickness of the radiator in terms of radiation length η, and the electron energy W_e. The factor of K = 0.47 accounts for the fact that this equation was originally calculated for ice and has been modified for sand. The factor of $\epsilon = 0.5$ accounts for the antenna being so close to the shower that it sees only half of the electric field. The values of the parameters $A_0 = 2.53 \times 10^{-7}$ and $\delta = 1.44$ are determined by Monte Carlo [29]. This curve is plotted with the data points in Figure 2.5, showing excellent agreement.

2.2.5 Linear Polarization

We measured the polarization properties of the shower in S-band and C-band. We pointed the S-band horn near the nominal shower max point. The horn axis was pointed at a 29° angle with respect to the beam axis. The horn was rotated so that the E-plane would be at an angle of 45°, 90°, and 135° with respect to the floor of the box. We did the same with the C-band horn, except that we did not take a 135° measurement, again due to time constraints.

The Stokes parameters I, Q and U are given by [30]:

$$I = I(0°, 0) + I(90°, 0) \tag{2.4}$$

$$Q = I(0°, 0) - I(90°, 0) \tag{2.5}$$

$$U = I(45°, 0) - I(135°, 0) \tag{2.6}$$

where $I(0°, 0)$ is the intensity at 0°, etc. The zero in the second argument denotes no relative phase difference between the orthogonal components of the electric field. Because the data were sampled at a rate much faster than the bandwidth of the S and C bandpasses, the raw data was averaged over approximately the inverse bandpass before analysis.

We had no device for measuring phase retardation so we assumed the circular polarization parameter V to be zero. In the case of the C-band horn, where we did not measure a value of $I(135°, 0)$, it can be shown that, if you assume zero circular polarization,

$$U = 2I(45°, 0) - I \tag{2.7}$$

Then the measure of polarization as a function of the Stokes parameters is given by:

$$p = \frac{\sqrt{Q^2 + U^2}}{I} \tag{2.8}$$

The polarization angle is

$$\gamma = \frac{1}{2}\mathrm{Tan}^{-1}\frac{U}{Q} \tag{2.9}$$

Figure 2.6 a shows the results for the S band data. The S-band shows 100% linear polarization over several nanoseconds. The polarization is lost after this due to interference from reflections. The polarization angle is close to zero over that region, so it appears that the plane of polarization is parallel to the plane of the floor, as expected.

Figure 2.6 b shows the C-band data. Note that these are band-limited pulses, so the C-band pulse is shorter than the S-band pulse as is the time over which nearly 100% polarization holds. The polarization angle is off by 10° which may be due to flaws in the C-band horn.

2.2.6 The Cherenkov Shockwave

We used the buried dipoles to look for the presence of the Cherenkov shockwave. This would be a cone with an angle of 51° propagating along the beam axis at the speed of light in vacuum. In that case, assuming the dipoles were all at equal distances from the beam axis, a plot of the dipole positions along the beam axis versus the time of the pulse would have a slope of $c = 3 \times 10^{10}$ cm/s.

The dipoles were buried along the far wall of the sandbox (opposite the polypropylene wall, see Figure 2.1), which has an angle of 3° with respect to the beam axis. The measured position of the dipoles is given by their perpendicular distance from the wall (d_w) and their distance along the wall from the downstream end of the box (d_d). The perpendicular distance (in centimeters) from the beam axis (x) and the distance (in centimeters) along the beam axis

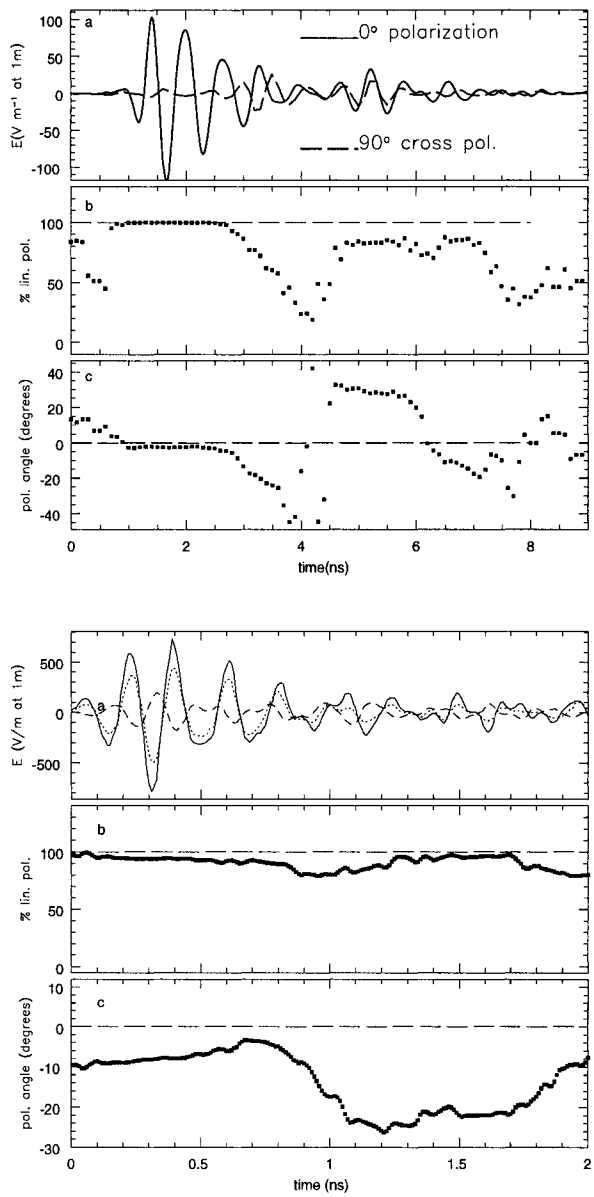

Figure 2.6: a) S-band horn polarization data. b) C-band horn polarization data. Note the difference in horizontal scale.

from the beam entrance point (z) are given by:

$$x = 50.95 - d_w \cos(3°) - (368.26 - d_d) \sin(3°)$$

$$z = (368.3 - d_d) \cos(3°) - d_w \sin(3°)$$

The time traveled by the Cherenkov radiation (propagating at the speed on light in sand) from the beam axis to the dipole is given by

$$t_r = \frac{x}{\sin(51°)} \frac{n}{c}$$

The other major correction is for cable delay (t_c). We measured a spread of 1 – 2 ns in the length of the heliax cables connecting the dipoles to the oscilloscope. If the measured time of the pulse received by the dipole is t, then the corrected time is $t_{correct} = t - t_r - t_c$.

Figure 2.7 shows the plot of z vs $t_{correct}$. The solid line is the least-squares fit to these points, which has a slope of $(2.9 \pm 0.4) \times 10^{10}$ cm/s. For this fit, $\chi^2/dof = 4.5/3 = 1.5$. The uncertainty in the distance (z) for this fit is $\sigma_z =$ 16.4 cm, which is the length of the error bars.

2.2.7 The Cherenkov Angle

The calculation above assumes the Cherenkov angle is 51°, or $n = 1.6$. Our most complicated measurement was to try and see if the signal actually showed a peak around 51°. To do this, we moved the S-band horn along the beam axis and changed its angle with respect to the axis. We pointed the horn at the shower max in such a way that the center of the antenna beam would coincide with radiation leaving the beam axis at $51° \pm \Delta\theta$, accounting for refraction into air at the polypropylene wall. The values of $\Delta\theta$ ranged from +8 to -6 degrees. Further measurements were impossible because of the constricted space and the large size of the horn.

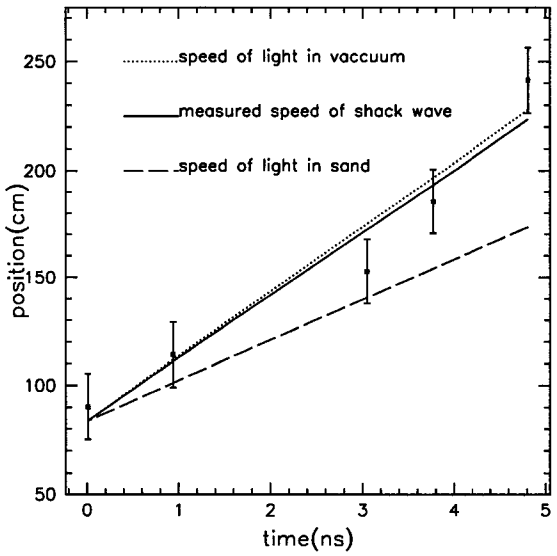

Figure 2.7: Position of the dipoles along the wall versus time of the pulse received by the dipole.

This data was corrected for the slight variation in beam current (2% over the whole run) and for the fact that the antenna beam (from +10° to -10°) projected on the beam axis, becomes larger as the antenna is moved downstream. Therefore the downstream points (which correspond to negative $\Delta\theta$) will see a larger signal. Figure 2.8 shows the corrected peak voltages against the nominal value of $\Delta\theta$. It shows a peak near 0°. The large error bars are due to scatter in the beam current, and error in pointing the antenna and measuring its position. The high point at $\Delta\theta = -4°$ may be due to anomalous amplification from one of the fins in the polypropylene wall, or it may just be a variation expected within the systematic uncertainty.

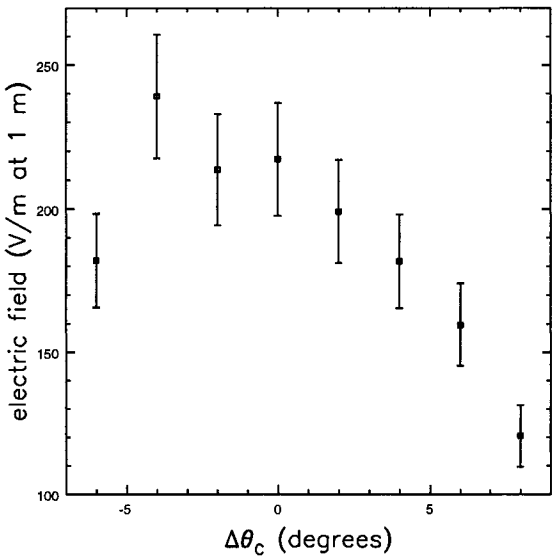

Figure 2.8: Electric field as a function of deviation from the Cherenkov angle.

2.2.8 Conclusions

The beam test at SLAC confirmed that a pulse of Cherenkov radiation is formed in a 10^{19} eV shower which is: bandwidth-limited, completely linearly polarized, and coherent, with the predicted intensity. Knowing the properties of the radiation are as predicted enables us to construct a suitable detector for neutrino events. Chapters 4 and 5 discuss such detectors, but first I discuss several additional beamtest results.

CHAPTER 3

Other Beamtests

3.1 SLAC Beamtest, 2002

Transition Radiation Measurement

We performed a second beamtest at SLAC in 2002. During this test we took the opportunity to make a measurement of the transition radiation (TR) produced by a target in the beam. The previous measurement at Argonne [26] had shown a discrepancy between the predicted and measured power in transition radiation. In the following sections I discuss the comparison between the Argonne and SLAC measurements and predicted values for the electric field.

3.1.1 Theoretical Calculation

The forward spectrum of transition radiation is [31]

$$\frac{d^2W_{TR}}{d\omega d\Omega} = \frac{h\alpha}{2\pi^3}\frac{\sqrt{\epsilon_2}\sin^2\theta\cos^2\theta}{1-\beta^2\epsilon_2\cos^2\theta}|\zeta|^2, \tag{3.1}$$

where ζ is given by

$$\zeta = \frac{(\epsilon_2-\epsilon_1)(1-\beta^2\epsilon_2-\beta\sqrt{\epsilon_1-\epsilon_2\sin^2\theta})}{(\epsilon_1+\sqrt{\epsilon_2}\sqrt{\epsilon_1-\epsilon_2\sin^2\theta})(1-\beta\sqrt{\epsilon_1-\epsilon_2\sin^2\theta})}, \tag{3.2}$$

where $d\omega$ is the bandwidth of the antenna ($d\omega = 2\pi d\nu$), and $d\Omega$ is the solid angle subtended by the horn, given by $\Omega = A/d^2$ where d is the distance from

the horn to the source, and A is the area of the horn. The angle θ is between the beamline and the line to the horn, and ϵ_1 and ϵ_2 are the upstream and downstream dielectric constants, respectively. For these two experiments, the upstream medium is aluminum ($|\epsilon_1| = 10$) and the downstream medium is air ($\epsilon_2 = (1.00035)^2$).

The energy is obtained by multiplying the RHS of Equation 3.2 by the bandwidth and solid angle. To convert to power, divide the energy by the typical time of the pulse (about the inverse bandwidth of the antenna). The power delivered to the load, P_L, is this power multiplied by the horn efficiency, about 0.5.

It is useful to look at the electric field E as well as the power. The Poynting flux S is given by $S = P_L/A_{eff} = E^2/Z_0$, where A_{eff} is the effective area of the antenna and $Z_0 = 377\ \Omega$. Therefore $E = \sqrt{Z_0 P_L/A_{eff}}$. We wish to look at the peak electric field, so we multiply E by a factor of $2\sqrt{2}$, since $E_{peak} = 2\sqrt{2}E_{rms}$ for a perfectly triangular envelope.

The finite beam size introduces coherence corrections. The corrected power is given by [32]

$$P = N_e(1 + N_e f_L f_T \chi)P_0, \tag{3.3}$$

where f_L, f_T, and χ are the longitudinal, transverse and angular form factors, respectively. If the distribution of the electrons is Gaussian, then Shibata *et al.* [33] give the form factors as:

$$f_L = \exp[-(\pi\sigma_L \cos\theta/\lambda)^2] \tag{3.4}$$

$$f_T = \exp[-(\pi\sigma_T \sin\theta/\lambda)^2] \tag{3.5}$$

$$\chi = \left(\frac{2\theta^2}{\pi\Omega^2} \int_0^{\pi/2\theta} x[(1-x)K(y) + (1+x)E(y)] \exp\left\{ -\frac{\theta^2}{\Omega^2} x^2 \right\} dx \right)^2, \qquad (3.6)$$

where σ_L and σ_T are the longitudinal and transverse divergence parameters, Ω is the angular divergence parameter, and $K(y)$ and $E(y)$ are the complete elliptic integrals of the first and second kinds, where $y = 2\sqrt{x}/(1+x)$:

$$K(y) = \int_0^{\pi/2} (1 - y^2 \sin^2 \omega)^{-1/2} d\omega \qquad (3.7)$$

$$E(y) = \int_0^{\pi/2} (1 - y^2 \sin^2 \omega)^{1/2} d\omega. \qquad (3.8)$$

In the perfectly coherent limit, $f_L = f_T = \chi = 1$ and since $N_e \gg 1$, $P = N_E^2 P_0$, as expected.

To compare the measured power to the calculated power, we take the average of V^2 over the measured pulse and divide by 50Ω. The measured voltage must be corrected for the attenuation in the circuit: $V_{correct} = V_{meas} 10^{atten(dB)/20}$.

To obtain the measured electric field, take the peak electric field

$$E_{peak} = 2V_{peak}/h_{eff} \qquad (3.9)$$

where h_{eff} is the effective height and V_{peak} is the measured peak voltage. Note that V_{peak}, the voltage in the load, is only half the open-circuit voltage if the load is perfectly matched to the source. Therefore $h_{eff} = 2V_{load}/E_{peak}$, but the usual definition is the equivalent $h_{eff} = V_{oc}/E$ where V_{oc} is the open-circuit voltage. The factor of 2 accounts for voltage dividing. The form of Equation 3.9 is used throughout the section.

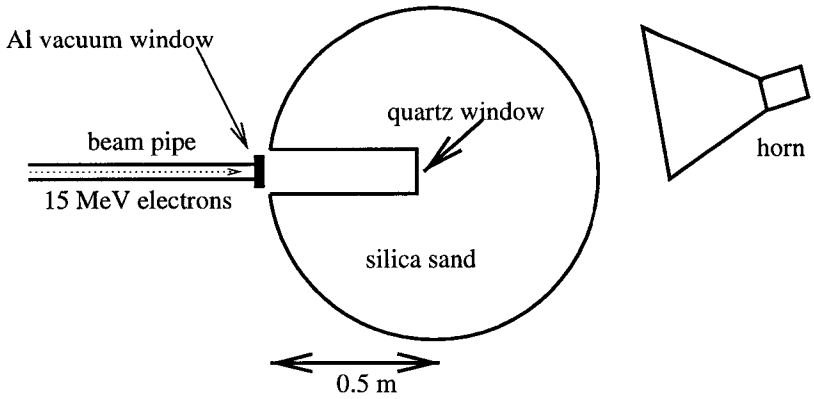

Figure 3.1: Experimental setup of Argonne 1999 run.

3.1.2 Argonne

At Argonne, the electron beam produced TR when it exited the aluminum vacuum window. The experimental setup is shown in Figure 3.1. We measured TR with an S-band horn (h_{eff} = 18 cm, λ = 13.9 cm, $d\nu$ = 900 MHz, area = 1036 cm^2). We measured the TR at $\theta = 8.5°$ and 16.6°. The electron energy was 15.2 MeV, so $\beta = .9994$. The longitudinal and transverse divergence parameters are $\sigma_L = 1.2$ cm and $\sigma_T = 0.7$ cm; therefore $f_L = 0.75$ and $f_T = 0.998$. We do not have an estimate of χ but assume it to be equal to 1, which is close to the correct value.

The measured voltage is corrected for 48.6 dB of attenuation. The typical time of the pulse is 1 ns. The results of the calculation for the two TR runs are shown in Table 3.1. The calculated power is approximately 100 times greater than the measured power. In the Argonne paper [26], the calculated power was quoted as being 27 times higher than the measured power, but there was a factor of 4 error in the calculation so the discrepancy was actually a factor of 108. The predicted electric field is about a factor of 15 too high. I discuss the reason for the discrepancy in the conclusion to this section.

Table 3.1: Results of Argonne TR run.

angle	distance (cm)	$d\Omega$ (sr)	N_e	P_L (W) calc.	P_L (W) meas.	E (V/m) calc.	E (V/m) meas.
8.5°	183	0.0309	9.99e10	2200	18	113	7.6
16.6°	178.4	0.0325	7.78e10	370	3.8	45	3.1

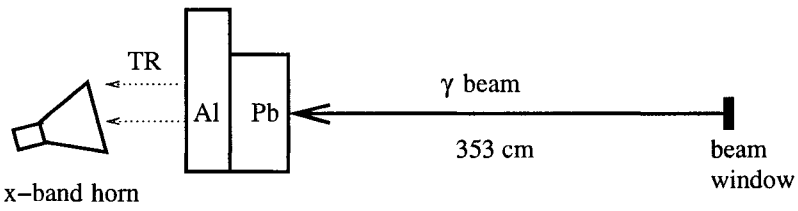

Figure 3.2: Experimental setup of SLAC 2002 TR run.

3.1.3 SLAC

During the SLAC beamtest in 2002, we used the photon beam to produce an electron-gamma shower in a 2 cm block of lead, followed by a 1.3 cm block of aluminum. The excess electrons from the shower produced TR as they exited the aluminum. We measured the TR with an X-band horn (h_{eff} = 2.4 cm, λ = 4.2 cm, $d\nu$ = 2 GHz, effective area = 18.87 cm^2). The experimental setup is shown in Figure 3.2. An Electron-Gamma Shower (EGS) simulation provided us with an estimate of the number of electrons, their energy, and their angular and transverse distributions, which are shown in Figure 3.3. The transverse and angular divergence parameters are estimated to be σ_T = 6 mm and Ω = 0.053 sr, respectively; therefore χ = 0.08 and f_T = 0.996. I assume f_L = 1. Most of the electrons are in the highest energy bin ($0.975 < \beta < 1$), so I use only the electrons in that bin for this calculation, setting β = .9875.

Table 3.2: Results of the SLAC TR run.

angle	distance (cm)	$d\Omega$ (sr)	N_e ($\times 10^6$)	$P_{L,calc}$ (mW)	$P_{L,meas}$ (mW)	E (V/m) calc.	E (V/m) meas.
10°	135.5	0.00103	531	0.26	0.5	0.28	0.31

The measured voltage is corrected for 31.5 dB of attenuation. The typical time of the pulse is .45 ns. The results of the TR run are in Table 3.2. Here, the calculated power is about half the measured power, much closer than the Argonne result. The calculated electric field is 90% of the measured electric field. We would expect it to be about 70% of the measured electric field based on the factor of 2 difference in the power, but the electric field calculation assumes a perfectly triangular envelope, which is not true. In the following section I determine the actual relationship between the peak and rms voltages.

3.1.4 Relationship Between Peak and RMS Voltage

We have two methods of describing the transient signal seen by an antenna matched to a load: the energy and the peak electric field. The energy transferred to the load is given by Energy $= \langle V^2 \rangle \Delta T / 50\Omega$, where ΔT is the duration of the pulse, comparable to the inverse bandpass of the antenna. The peak electric field is $E_p = 2V_p/h_{eff}$, from Equation 3.9.

A typical band-limited pulse shape is a sine wave modulated by some envelope. Therefore the rms voltage $V_{rms} = \sqrt{\langle V^2 \rangle - \langle V \rangle^2} = \sqrt{< V^2 >}$, since V averages to zero. We want to relate the rms voltage to the peak voltage, thus relating the energy to the peak electric field.

If the signal were a pure sine wave, then $V_{rms} = V_p/\sqrt{2}$. Since there is

Table 3.3: The k factor for Argonne and SLAC antennas.

antenna	bandpass	% bandpass	k
log periodic w/filter	3.3 - 6.6 GHz	50%	1.4
log periodic w/filter	6.16 - 7 GHz	12%	1.4
log periodic w/filter	17.5 -18.5 GHz	5%	1.5
X-band horn	5.85 - 8.2 GHz	29%	1.4
S-band horn (Argonne) (TR)	1.7 - 2.6 GHz	35%	1.2
S-band horn (SLAC) (CR)	1.7 - 2.6 GHz	35%	1.7
C-band horn	4.4 - 5.6 GHz	21%	1.3
unbalanced dipole	1 - 1.5 GHz	33%	1.2
balanced dipole (in sand)	1 - 1.5 GHz	33%	1.2
balanced dipole (in air)	1.6 - 2 GHz	20%	1.0
RICE dipole	0.2 - 0.6 GHz	67%	1.6
bowtie 12 (in salt)	0.13 - 0.6 GHz	78%	1.3
bowtie 5 (in salt)	0.13 - 0.6 GHz	78%	1.4

also an envelope, the rms voltage may be further reduced from the peak voltage by some factor. For a triangular envelope, that factor would be 1/2, so that $V_{rms} = V_p/2\sqrt{2}$. In general, we define a factor k such that

$$V_{rms} = \sqrt{\langle V^2 \rangle} = \frac{kV_p}{2\sqrt{2}} \tag{3.10}$$

In Table 3.3 I list the k factor for various antennas that we have used at Argonne and SLAC. I take the average of V^2 over the inverse bandpass of the antenna. There is not any apparent correlation between k and bandwidth. The average value of k is 1.4.

Table 3.4: The transition radiation results from Argonne and SLAC, using both methods.

run	meas. energy (Joules) method 1	meas. energy (Joules) method 2
Argonne	1.8×10^{-8}	2.1×10^{-8}
SLAC	2.6×10^{-13}	2.8×10^{-13}

3.1.4.1 Energy Comparison

I compared the energy measurement for two TR pulses from Argonne (S-band horn) and SLAC (X-band horn), made in different ways:

1) Using the average power: $Energy = (\langle V^2 \rangle / 50\Omega)\Delta T = (V_{rms}^2/50)\Delta T$, where ΔT is the inverse bandwidth.

2) Using the peak electric field: $Energy = (E_p^2 A_{eff}/Z_0)\Delta T$, noting that $E_p = 2V_p/h_{eff}$, from Equation 3.9. This should then be multiplied by a factor of $(k/2\sqrt{2})^2 = k^2/8$ since $V_p = 2\sqrt{2}V_{rms}/k$.

I take $k = 1.4$. Table 3.4 shows the results. These agree well, so it is necessary to take the factor of k as well as $1/2\sqrt{2}$ into account when going between these two methods of getting the energy. Therefore the peak and rms voltages are related by $V_{rms} = kV_p/2\sqrt{2}$, where $k \approx 1.4$.

3.1.5 Conclusions

The SLAC TR data agrees with prediction far better than the Argonne data. The SLAC experiment was performed several years after the Argonne experiment and benefited from experience, and a better measurement of the beam current at SLAC. The SLAC TR, coming from a shower in a material, is closer to what we

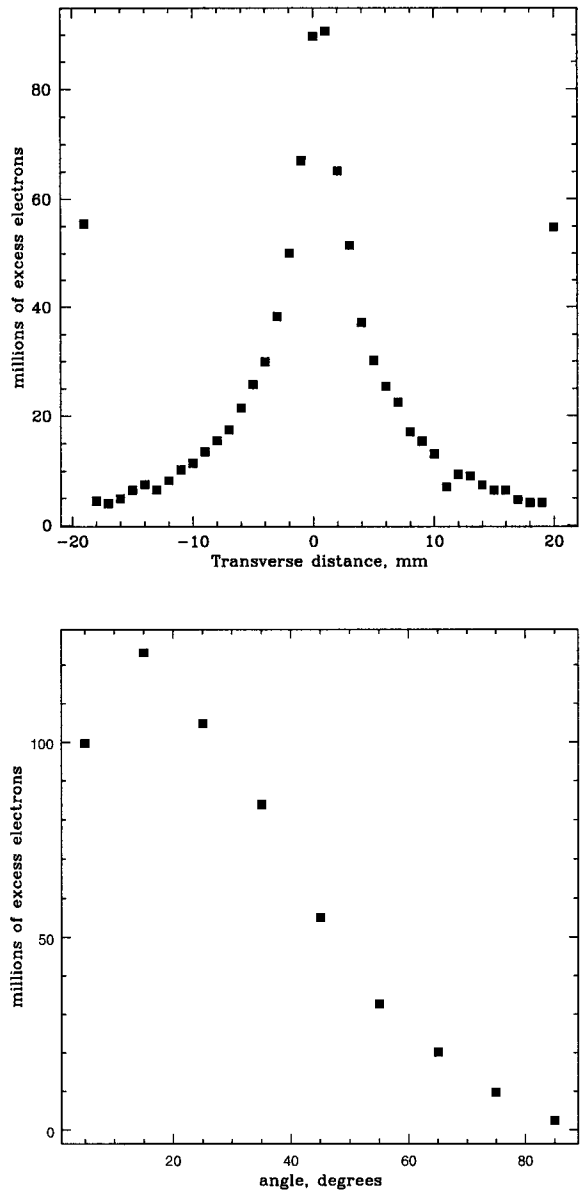

Figure 3.3: Top: Transverse spread in electron shower. The extreme left and right points are overflow bins. Bottom: angular spread in electron shower, for the highest energy bin ($0.975 < \beta < 1$). Shower simulation data provided by Clive Field.

would expect to see in an actual observation.

3.2 Argonne Beamtest, 2003
Potential for Radio Calorimetry

This section describes data taken on June 26, 2003 at Argonne Wakefield Accelerator (AWA). When a beam of high energy particles interacts with a solid medium such as salt, it creates a plasma of ionization electrons. The plasma frequency ν_p (in SI units) is given by

$$\nu_p = \frac{1}{2\pi}\sqrt{\frac{n_e q_e^2}{\epsilon_0 m_e}} \tag{3.11}$$

The plasma frequency for salt is estimated to be in the 10-100 GHz range (see below for more precise calculation). A signal with $\nu < \nu_p$ should reflect off the plasma, if the wavelength of the signal is smaller than the size of the plasma. If the wavelength of the signal is larger than the size of the plasma, then the signal might pass through the plasma as an evanescent wave rather than reflecting. The purpose of this experiment is to explore the possibility of RF calorimetry, since the plasma frequency depends on the energy deposited by the incident particle.

3.2.1 Setup

The AWA apparatus is shown in Figure 3.4. We ran two half-inch heliax cables from the control room into the beam vault and attached them via a T junction to one end of a DRG 250 waveguide, which was filled with non-iodized table salt. The other end of the waveguide was capped with a 50 Ω load. In the control room, we split a continuous wave (CW) signal from an HP 8350A signal generator providing frequencies from 2.8 to 8.4 GHz. One half of the CW

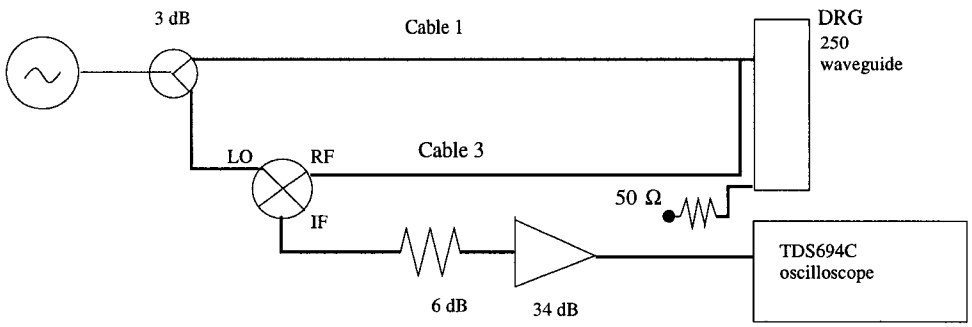

Figure 3.4: Cabling setup for T-to-waveguide runs. For T-to-load runs, replace waveguide with 50 Ω load.

signal was sent down one heliax, designated cable 1, to the waveguide. The other half was sent into a mixer as the local oscillator (LO) signal. The other heliax, designated cable 3, was attached to the mixer as the RF signal. The output or IF signal was read by a 3 GHz TDS 694C oscilloscope. The oscilloscope was triggered by a dipole suspended in front of the beampipe window. For some runs, as a control, we detached the waveguide from the T junction, and put a 50 Ω load on the T junction instead, leaving everything else the same.

We took data with the waveguide in two positions. The first position was 5 cm downstream of the beampipe window. This is upstream of a large copper box (the apparatus of a different experiment). The second position was 193 cm downstream of the beampipe window, which was downstream of the copper box. Runs taken upstream of the copper box are designated "upstream", and runs taken downstream of the box are designated "downstream". Figure 3.5 shows the mixer output for a T-to-load run compared to a T-to-waveguide run when the LO is set at 2.8 GHz for a downstream run.

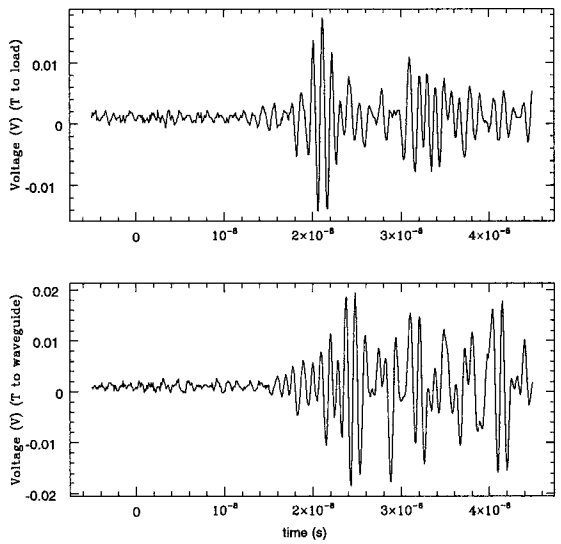

Figure 3.5: Top: mixer output for T-to-load run. Bottom:mixer output for T-to-waveguide run. LO is set at 2.8 GHz, waveguide is downstream.

3.2.2 Analysis: Upstream Frequency Scan

We set the local oscillator to 2.8, 4.8, 6.8 and 8.4 GHz. For each frequency we took a T-to-load and a T-to-waveguide run. We recorded 25 shots separately in each configuration. Since the beam intensity varied during each run, we consider all 25 shots to compare the load output to the waveguide output. We use the trigger dipole as the measure of the beam intensity.

To compare the load and waveguide runs, we define a ratio

$$\eta = \frac{\Sigma V^2_{mixer}}{\Sigma V^2_{dipole}}$$

where the sum is taken over the whole pulse.

We then compare a histogram of η_{load} to a histogram of $\eta_{waveguide}$ for each frequency. The results are shown in figure 3.6. The mixer output for T-to-waveguide in the upstream position shows a stronger average signal than for

T-to-load for all frequencies. Presumably, transition radiation and Cherenkov radiation are being produced inside the waveguide by the $\sim$ 1 cm beamspot.

3.2.3 Analysis: Downstream Frequency Scan

We repeat the procedure for the runs taken downstream of the copper box. Figure 3.7 shows the histograms of η_{load} and $\eta_{waveguide}$ for the same set of frequencies.

For 2.8 and 4.8 GHz, the waveguide still shows a stronger signal than the load. However, for 6.8 and 8.4 GHz, there is no separation between the load and the waveguide signal. If the waveguide is seeing TR and CR from a shower inside the salt, then the loss of separation at higher frequencies may be due to the coherence rolloff. There would be less TR and CR downstream, where the beam is less focused.

3.2.4 Discussion

We looked for a reflection signal, independent of any coherent CR or TR, when we are looking below the plasma frequency. The electron beam at Argonne produced bunches of 14 MeV electrons with a beam current of 10 nC $= 6.25 \times 10^{10}$ electrons per bunch. The electron beam then passes through a tungsten radiator, where 20% of the electrons are converted to photons with an average energy of 8 MeV, so the total photon energy per bunch is 1×10^{17} eV. We estimate that about 30% of the photon energy is deposited in the salt inside the waveguide.

Downstream, the loss of coherence after 5 GHz indicates a lateral spread (in salt, $n = 1.5$) of about 4 cm. The height of the waveguide is 2.5 cm and the length traversed by the beam is 5 cm, so the volume in which the energy is

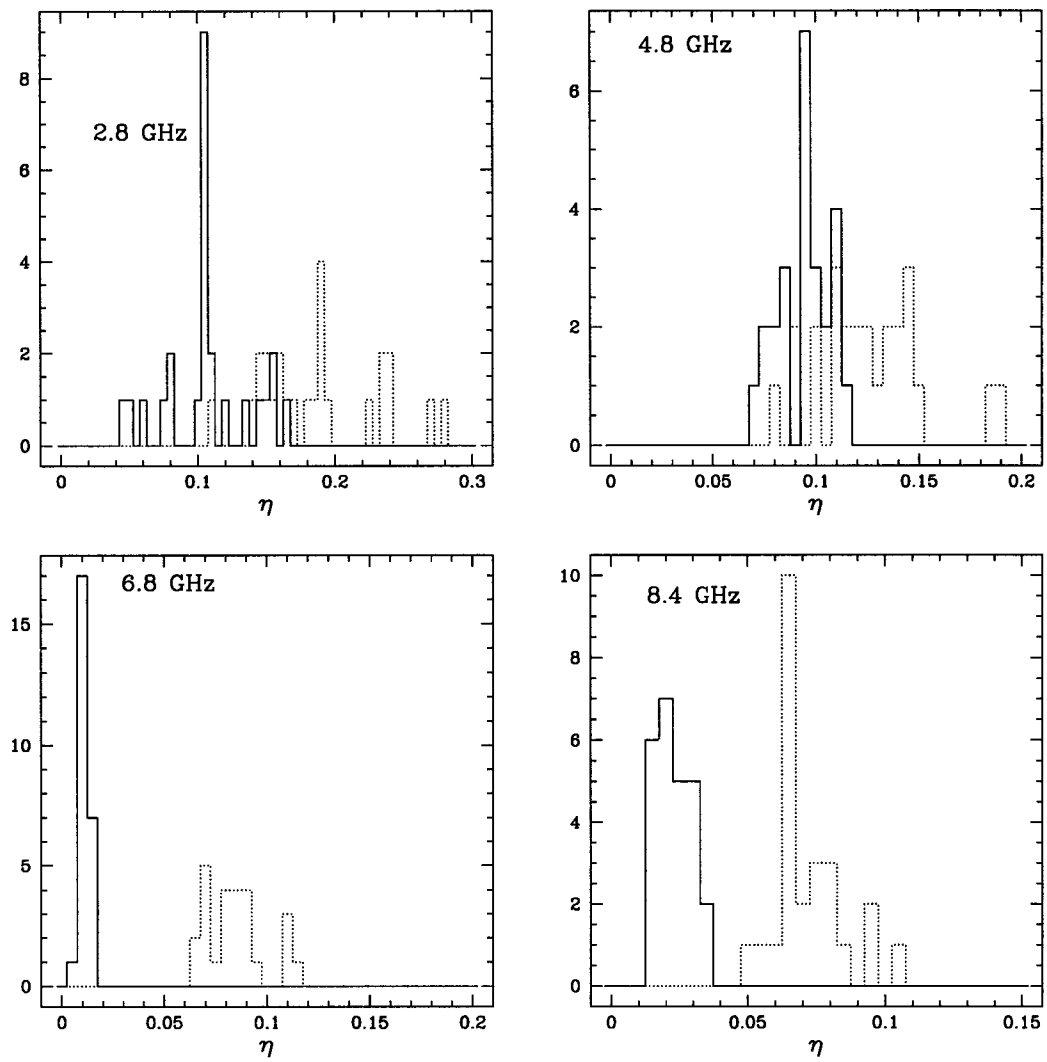

Figure 3.6: Histograms of η_{load} (solid) and $\eta_{waveguide}$ (dotted) for all frequencies. Top left: 2.8 GHz. Top right: 4.8 GHz. Bottom left: 6.8 GHz. Bottom right: 8.4 GHz.

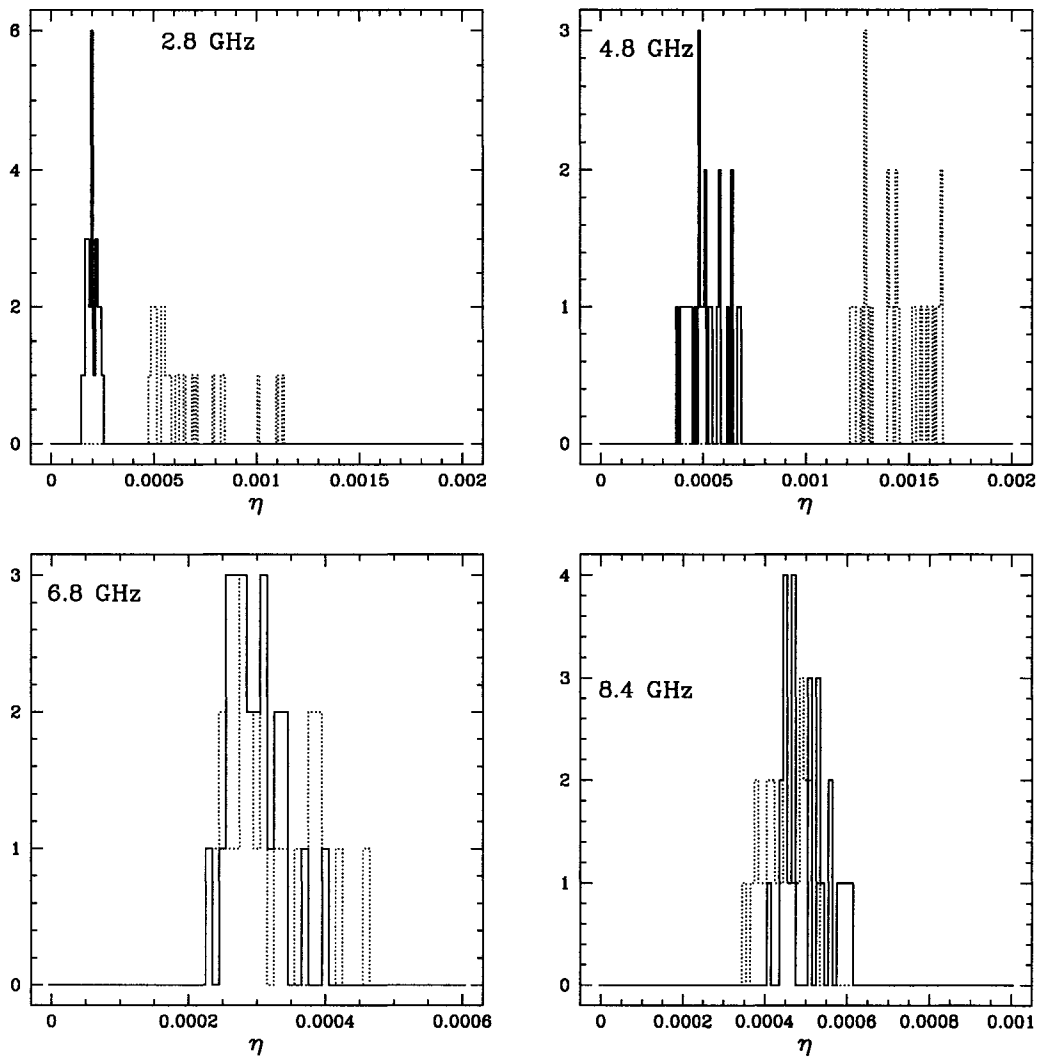

Figure 3.7: Histograms of η_{load} (solid) and $\eta_{waveguide}$ (dotted) for all frequencies. Top left: 2.8 GHz. Top right: 4.8 GHz. Bottom left: 6.8 GHz. Bottom right: 8.4 GHz.

deposited is 50 cm^3. Assuming 1 ionization electron produced per 30 eV of energy deposited, the number density of ionization electrons produced is 2.3×10^{13} cm^{-3} or 7×10^{19} m^{-3}. All numbers are approximate. Plugging these values into Equation 3.11, the plasma frequency is about 40 GHz for the plasma produced by this beam in the waveguide. The frequencies which we used were below the plasma frequency.

3.2.5 Conclusions

We see the expected loss of coherence in CR and TR emission downstream for frequencies above 6.8 GHz. There is no evidence for a signal from the RF reflecting off the plasma at these high frequencies. It should be noted that we intended to measure frequencies up through 18 GHz, but the signal generator was damaged in shipment and we had to use a signal generator with a much lower frequency cutoff.

In order to make a thorough investigation, we should look at a higher frequency which is still below the plasma frequency, because the wavelength at 8 GHz is comparable to the size of the beam spot and the resulting plasma, in which case the reflection might be suppressed by the evanescence effect. A clear signal of the effect we are looking for would be to see the drop in emission vs. frequency shown here, due to loss of coherence, followed by an increase at even higher frequencies as the evanescence effect no longer suppresses the reflected signal.

CHAPTER 4

Radio Detection of EHE Neutrinos Using the Lunar Regolith: The Goldstone Lunar Ultra-High Energy Neutrino Experiment

4.1 The Lunar Regolith as a Neutrino Target

In his original paper [24], Askar'yan suggested directly instrumenting the lunar regolith with radio antennas to search for EHE neutrinos. The lunar regolith is an aggregate layer of fine particles and small rocks, thought to be the accumulated ejecta of meteor impacts with the lunar surface. It consists mostly of silicates and related minerals, with meteoritic iron and titanium compounds at an average level of several per cent, and traces of meteoritic carbon. It has a typical depth of 10 to 20 m in the maria and valleys, but may be hundreds of meters deep in portions of the highlands [34]. The raw volume is approximately 200,000 km^3 water equivalent. It has a mean dielectric constant of $\epsilon \simeq 3$ and a density of $\rho \simeq 1.7$ g cm^{-3}, both increasing slowly with depth. Measured values for the loss tangent vary widely depending on iron and titanium content, but a mean value at high frequencies is $\tan\delta \simeq 0.003$, implying a field attenuation length at 2 GHz of $(\alpha)^{-1} = 9$ m [35], which is comparable to the depth of the regolith.

The cost of instrumenting the regolith directly, as Askar'yan suggested, would

be prohibitive. Instead, Dagkesemanskii and Zhelezykh [37] suggest using Earth-based radio telescopes, which have the advantage of being able to see much of the regolith at once. Based on the peak electric field strength of a neutrino shower in the regolith [36], we estimate an energy threshold of about 10^{19} eV for a 6σ voltage at Earth, using typical telescope parameters from the Goldstone experiment described in Section 4.2. I make a detailed estimate of the energy threshold in Section 4.6.4.

In Fig. 4.1 I illustrate the neutrino signal emission geometry. At 10^{20} eV the interaction length of a neutrino for the dominant deep inelastic hadronic scattering interactions (averaging over the charged and neutral current processes) is about 60 km [19]. The lunar radius is 1740 km, so neutrinos "skimming", or traveling on shallow chords, would be most likely to produce detectable showers. Note that cosmic rays would shower immediately upon entering the moon, as shown in Fig. 4.1, and therefore any shower radiation would totally internally reflect in the limit of a smooth moon (see Section 2.2.1). Therefore we expect any signal from cosmic ray showers to be strongly suppressed. Neutrinos could shower on downgoing chords after traveling a very short distance since the moon is not perfectly smooth.

Hankins *et al.* undertook the first radio search for neutrinos interacting in the regolith [38]. They used the Parkes 64 m telescope in Australia and observed in the frequency band from 1175 to 1675 MHz, for 10 hours. At these frequencies, there should be a 30–50 ns ionospheric delay across the band. The Parkes telescope observed in two orthogonal circular polarizations, expecting that the linearly polarized Cherenkov signal would exhibit equal amplitudes in both polarizations. They used the ionospheric delay signature to distinguish a possible signal from the moon from local radio frequency interference (RFI), which would

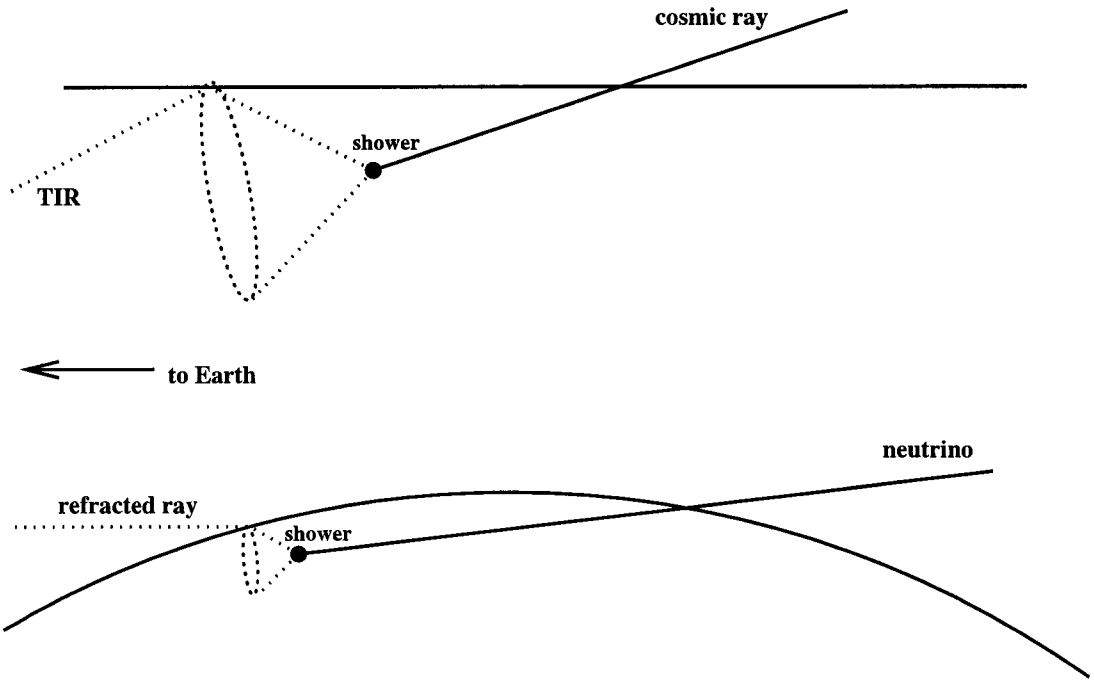

Figure 4.1: Top: cosmic ray shower, which occurs immediately after the cosmic ray enters the moon; all Cherenkov radiation totally internally reflects. Bottom: neutrino shower, on a shallow chord, where the Cherenkov radiation is refracted towards Earth.

have no delay across the band. No events passed all of their criteria.

The Parkes telescope was pointed at the moon center for most of the experiment, which has a higher system temperature than when the telescope is pointing at the moon limb. That, and the fact that most detectable events should occur in the limb as "skimming" events, make it advantageous to point at the moon limb. However, this decreases the amount of the regolith in the telescope's beam spot. This tradeoff will be discussed further in Section 4.6. Another disadvantage to the Parkes experiment is that a single dish is subject to local RFI.

In 1999, a long-term radio neutrino search began at the Goldstone Deep Space Tracking Station, part of the NASA Deep Space Network (DSN). The Goldstone Lunar Ultra-high energy neutrino Experiment (GLUE) is based in the RARG room at the Mars Site antenna (DSS14). In September 2000, the experimental configuration was stable and we begin data analysis at that point. GLUE uses two antennas, which act as a simple interferometer, and are less sensitive to local RFI.

4.2 Goldstone Data Set

In this section I describe the data flow in GLUE, and how the trigger is formed of local coincidences at the two antennas and a global coincidence between them. I discuss the thermal trigger rate, and the methods employed to reduce RFI triggers. Finally I summarize the GLUE data set from September 2001 through the last run in August 2003.

4.2.1 Data Channels

Figure 4.3 shows the data channels in GLUE, as well as the data acquisition system. The antennas employed in our search are the shaped-Cassegrainian 70 m antenna DSS14, and the beam waveguide 34 m antenna DSS13, both part of the DSN and separated by 22 km. The S-band (2.2 GHz) right-circular-polarization (RCP) signal from DSS13 is filtered to 150 MHz bandwidth and down-converted to an intermediate frequency (IF) near 300 MHz. We subdivide the band into high and low frequency halves with no overlap (denoted DSS13 Hi and DSS13 Lo). Prior to early 2002, these IF signals were sent separately via an analog fiber-optic link to DSS14, and since that time, the signals are split after the analog fiber link. The DSS14 dual polarization S-band signals are down-converted to the same 300 MHz IF, using bandwidths of 150 MHz (RCP) and 40 MHz (LCP). The different bandwidths are due to the two polarizations being sent through different amplifiers. Since late 2001, we also split the DSS14 RCP channel into two 75 MHz bands (DSS14 RCP Hi and DSS14 RCP Lo) to improve the trigger performance by ensuring a broadband signal. Figure 4.2 shows the bandpasses of the RCP and LCP channels at DSS14 and the high and low bandpasses at DSS13. At DSS14, a 1.8 GHz (L-band) feed, pointed off-axis by $\sim 0.5°$, produces a 40 MHz bandwidth monitor of terrestrial interference signals that we record along with the other signals.

4.2.2 Local Triggers

Fig. 4.3 shows the layout of the trigger. The four (or five if the DSS14 split RCP is used) triggering signals from the two antennas are converted to unipolar pulses using tunnel-diode square-law detectors with a $\sim$ 10 ns integration time. We discriminate these pulses to a roughly constant singles rate: 30 kHz for both

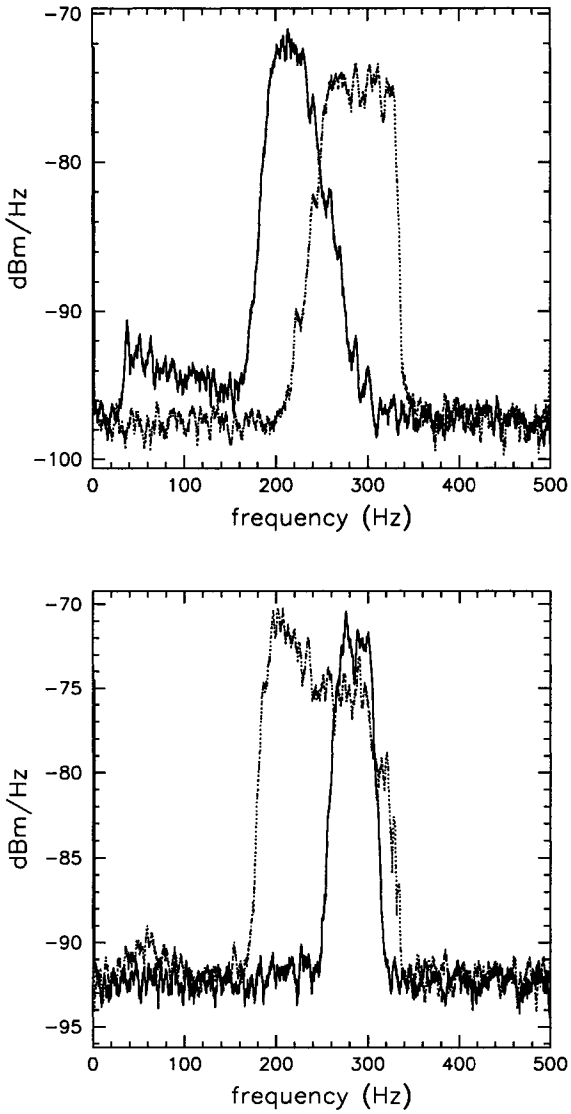

Figure 4.2: Bandpasses of Goldstone channels. Top: DSS13 low band (solid) and high band(dashed). Bottom: DSS14 LCP (solid) and RCP (dashed).

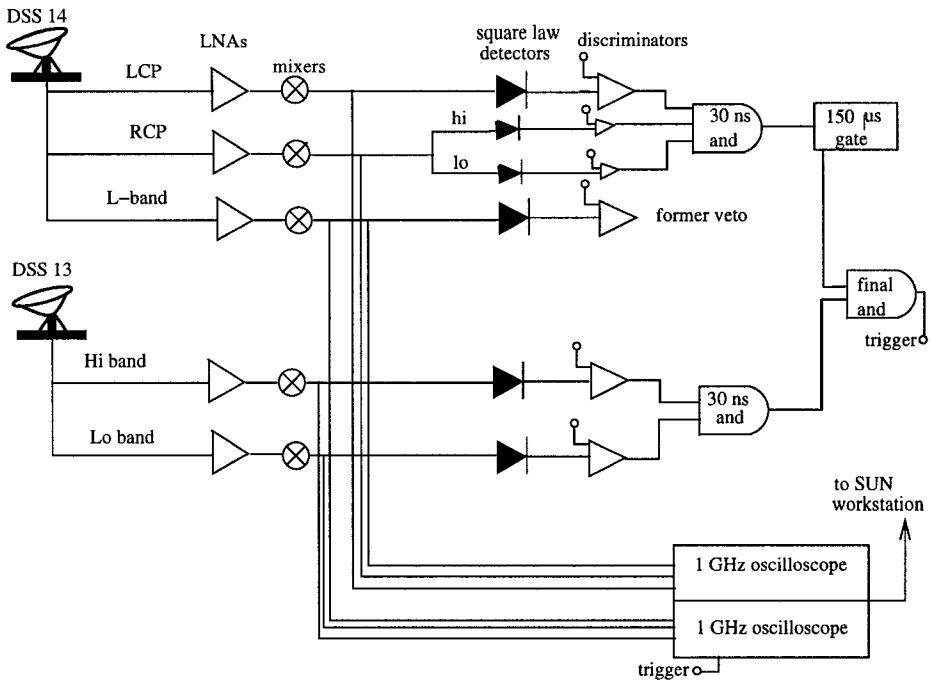

Figure 4.3: The GLUE trigger system used for the lunar neutrino search.

DSS13 channels, 30 kHz for both DSS14 RCP channels, and 45 kHz for the DSS14 LCP channel. The higher singles rate in the LCP channel compensates for the lower bandwidth. A local coincidence within 30 ns is formed between each antenna's channels. The DSS14 coincidence between both circular polarizations ensures that the signals are highly linearly polarized, and the DSS13 and DSS14 split-channel coincidence helps to ensure that the signal is broadband.

4.2.3 Global Trigger

The local coincidence from DSS14 opens a 150 μs window after a 63 μs delay. A local coincidence from DSS13 within this window forms the global trigger. The delay and the size of the window take into account the fact that the time difference between a signal at DSS14 and a signal at DSS13 includes the cable

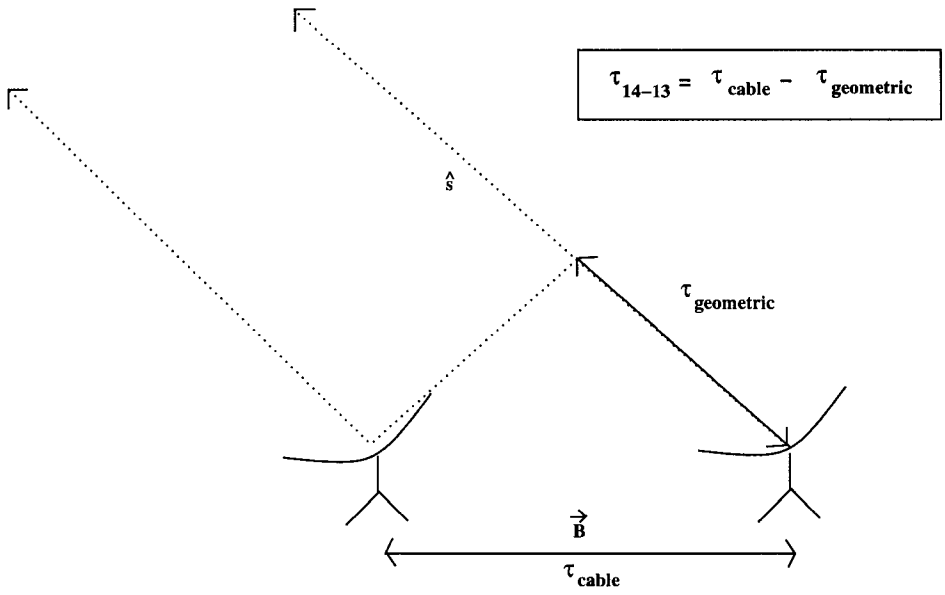

Figure 4.4: Geometric and cable delay diagram.

delay from DSS13 to DSS14 and the geometric delay τ_{geo}, which is the difference in path lengths of a ray from the moon to each telescope. Figure 4.4 illustrates the relation between the delays. In this figure, $\hat{s}$ is a unit direction vector to the Moon, and $\vec{B}$ is the baseline vector between the two antennas. The projected baseline is $B_\perp = \vec{B} \cdot \hat{s}$, and the relative delay between the two antennas is $\tau_{geo} = B_\perp / c = c^{-1} |\vec{B}| \cos\theta$ where θ is the apparent angle of the Moon with respect to the baseline vector. For our 22 km baseline, we have a delay range of $\tau_{geo} = \pm 73$ μs. The cable delay is within 1 μs of 136 μs (see Section 4.3.2), so the minimum total time delay from DSS13 to DSS14 is $136 - 73 = 63 \mu$s and the window size is $2 \times 73 = 146$ μs, which we set to a 150 μs window. Therefore the time window encompasses the possible geometric delay range for the Moon throughout the year. Although use of a smaller window is possible, a tighter coincidence is required offline and the out-of-time events provide a large background sample.

Detectable events can occur anywhere on the Moon's surface within the an-

tenna beam. This produces a possible spread in the differential delay of the received pulses at the two antennas, which has the maximum value $\Delta\tau_{geo} = c^{-1}|\vec{B}| \sin\Delta\theta \simeq 637$ ns, given that the angular diameter of the Moon is $\Delta\theta = 0.5°$.

The global coincidence triggers two sampling oscilloscopes. A Sun workstation, connected to the oscilloscopes via GPIB, records a 250 μs record, sampled at 1 GSa/s.

4.2.4 Thermal Trigger Rate

The singles rates of individual channels and the width of the coincidence gates determine the trigger rate from (Gaussian) random thermal fluctuations. At DSS14, the LCP singles rate is 45 kHz and the two RCP singles rates are 30 kHz, with a 30 ns local coincidence gate. Noting that the coincidence window is twice the gate width, the local coincidence rate at DSS14 is then

$$\Gamma_{14} = 45\text{kHz} \times (30\text{kHz})^2 \times (60\text{ns})^2 = 0.1458\text{Hz}$$

At DSS13, the singles rates is 30 kHz in both channels with a 30 ns local coincidence gate. The local coincidence rate at DSS13 is then

$$\Gamma_{13} = (30\text{kHz})^2 \times (60\text{ns}) = 54\text{Hz}$$

The global coincidence gate is 150 μs, so the global thermal trigger rate is

$$\Gamma = \Gamma_{13} \times \Gamma_{14} \times 300\mu\text{s} = 0.0024\text{Hz}$$

which is approximately the observed trigger rate on a quiet night.

4.2.5 RFI Triggers

Terrestrial RFI triggers are a few percent of the total, but can occasionally increase in number when a large burst of interference occurs at either antenna.

To avoid recording large bursts of terrestrial noise, a 6 s holdoff is employed after each trigger. We maintain > 90% livetime during a run.

On rare nights with extremely heavy RFI, we employ an active L-band veto in the trigger. We convert the off-axis L-band signal to a unipolar pulse and discriminate it in the same manner as the S-band signals from DSS13 and DSS14. The output triggers an updating discriminator with a 500 ns gate, which vetoes the DSS14 local coincidence unit. This veto can reduce the trigger rate from one every six seconds (maximum deadtime) to one every two minutes.

4.2.6 GLUE Run Summary

We used three pointing configurations: limb, which corresponds to moon center plus an elevation of 0.25°; half-limb, which corresponds to moon center plus an elevation of 0.125°; and moon center. The system temperature, and therefore the thermal noise level, depend on the pointing configuration, since more of the beam is filled with the moon when pointed at the center. The approximate system temperatures are 180 K at moon center, 160 K at half-limb and 110 K at the limb.

We also used DSS14 in both a focused and a defocused mode. The antenna beamwidths for a frequency of 2.2 GHz, between the first Airy nulls, are nominally 0.27° for the 70 m, and 0.56° for the 34 m. For the observations from mid-2001 to mid-2002 in which we point at the center or half-limb position, we intentionally defocused the DSS14 beam to provide a better match to the DSS13 beam (with some loss of efficiency), hence we account for the entire 637 ns window when determining whether a triggered event has a delay that is appropriate for lunar origin.

I summarize all runs used in data analysis from 2000 – 2003 in Tables 4.1, 4.2,

Table 4.1: Run Summary 2000

Date	Events	Hours	Live Hours	Pointing	Focus
1 September	104	4.77	4.60	Limb	focused
8-9 September	74	3.68	3.56	Limb	focused
30 September	24	1.78	1.54	Limb	focused
1 October	35	2.77	2.71	Limb	focused
2 October	134	5.22	5.00	Limb	focused
11 December	149	8.19	7.94	Limb	focused

4.3, and 4.4. Each table shows the number of events in a given run, the livetime, the pointing configuration and the focus of DSS14. The tables show whether the DSS14 beam is focused or defocused, and what the pointing configuration is on any given night. In all, we have 40 hours of data in the half-limb, defocused position, 10 hours in the center, defocused position, and 73 hours in the limb, focused position. The total livetime is 123 hours.

4.3 Timing and Amplitude Calibration

The data analysis depends critically on knowing the timing of the system, and the amplitude response. Timing and amplitude calibration are accomplished by a series of interlocking methods. We calibrate the local timing at DSS13 and DSS14 individually, then calibrate the global timing difference.

Table 4.2: Run Summary 2001

Date	Events	Hours	Live	Pointing	Focus
12 March	97	3.68	3.52	Limb	focused
13 March	99	3.92	3.76	Center	beam defocused
14 March	109	4.37	4.17	Center	defocused
11 May	155	2.68	2.42	Center	defocused
12 May	85	3.31	3.17	half-limb	defocused
13 May	75	4.23	4.11	half-limb	defocused
22 June	262	8.49	8.05	half-limb	defocused
30 September	50	3.64	3.56	half-limb	defocused

Table 4.3: Run Summary 2002

Date	Events	Hours	Live	Pointing	Focus
3 March	100	3.09	2.92	half-limb	defocused, active veto
4 March	145	4.14	3.89	half-limb	defocused,active veto
17 April	148	4.89	4.64	half-limb	defocused
2 May	165	5.40	5.13	half-limb	defocused
4 May	82	4.52	4.38	half-limb	defocused
28 May	153	6.84	6.63	Limb	focused
10 November	175	5.01	4.72	limb	focused
16-17 November	169	5.36	5.36	limb	focused
18 November	150	6.49	6.24	limb	focused

Table 4.4: Run Summary 2003

Date	Events	Hours	Live	Pointing	Focus
8 April	243	9.29	8.89	limb	focused
25 May	419	6.20	5.50	limb	focused
24-25 August	262	7.68	7.24	limb	focused

Table 4.5: Local Calibration 2000

Date	14 LR monocycle	14LR rim	13 H monocycle	13 HL quasar
1 October	–	–	–	–
2 October	–	-2	–	-1
11 December	–	–	–	–

4.3.1 Local Timing Calibration

We internally calibrate the back-end trigger system using a synthesized IF pulse signal, giving precision of order 1 ns. In addition, we use a 2.2 GHz monocycle pulse generator aimed at the antennas to calibrate the cross-channel delays of each antenna to a precision of 2 ns. Figure 4.5 shows the monocycle pulse at DSS14. We also check the cross-polarization timing at DSS14 using thermal radiation from the limb of the Moon which is significantly linearly polarized due to differential Fresnel effects [39, 40]; this introduces a positive LCP-to-RCP correlation that is easily detected. Tables 4.5, 4.6, 4.7 and 4.8 show the local calibration data from all methods for all runs that were used in the final analysis. Where no local calibration data is available for a given run, we use the calibration data from the nearest run.

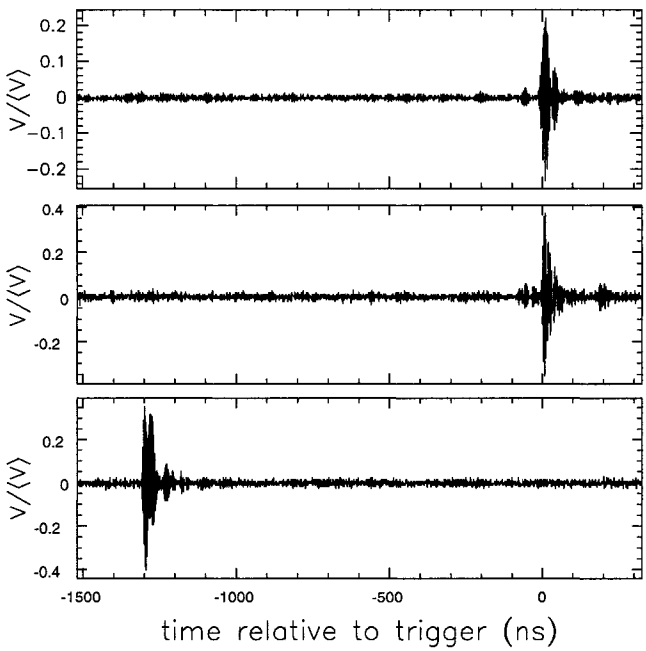

Figure 4.5: Monocycle pulse at DSS14. From the top: DSS14 LCP, DSS14 RCP, and the off-axis L-band feed.

Table 4.6: Local Calibration 2001

Date	14 LR monocycle	14LR rim	13 HL monocycle	13 HL quasar
12 March	—	-4.6	—	0.9
13 March	—	–	–	4
14 March	—	-2.8	–	3.8
11 May	—	—	–	-2
12 May	—	—	–	-5.1
13 May	—	—	–	7
22 June	-12.8	–	3.4	4
30 September	–	-12.6	–	7.2

Table 4.7: Local Calibration 2002

Date	14 LR monocycle	14LR rim	13 HL monocycle	13 HL quasar
2 March	–	0.79	–	-4.53
3 March	–	–	–	3.96
4 March	–	–	–	2.3
17 April	–	7	–	2.8
2 May	-6.9	-2.9	–	-2.1
4 May	-7.5	–	–	-2
28 May	-8	-2	–	-2
10 November	-2.4	–	1.6	1.8
16-17 November	-13.9	-6.8	9.2	3.1
18 November	—	—	—	—

Table 4.8: Local Calibration 2003

Date	14 LR monocycle	14LR rim	13 HL monocycle	13 HL quasar
8 April	–	-5	–	-7.1
25 May	-3.3	-6.9	-1.9	-1.9
24-25 August	-3.6	-7.7	–	3.6

4.3.2 Global Timing Calibration

To determine the total time difference between DSS13 and DSS14, we point both antennas at an unresolved quasar and cross-correlate the DSS13 and DSS14 RCP signals. The total time difference between the DSS14 and DSS13 signals is equal to the cable delay minus the geometric delay, as shown in Figure 4.4.

Fomalont and Wright [42] give the formula for calculating the geometric delay between the arrival of a plane wave from the quasar at DSS13 and DSS14.

$$\tau_{geo} = \frac{1}{c}(B_x \cos\delta \cosh + B_y \cos\delta \sinh + B_z \sin\delta), \tag{4.1}$$

where B_x, etc. are the components of the baseline between the two telescopes ($\vec{B} = \vec{r}_{DSS14} - \vec{r}_{DSS13}$) and δ is the declination of the source. The DSN website [43] gives the Cartesian coordinates of DSS13 and DSS14 in the ITRF93 frame. Note that this is a left-handed coordinate system, so I have changed the sign of y in table 4.3.2 to be opposite the sign quoted on the website. Therefore $B_x = -2508.76$ m, $B_y = -14189.172$ m, and $B_z = 16139.583$ m.

Next, I calculate the hour angle h of the quasar in question. The following formula holds true in 2001 [41]:

$$\text{GMST} = 6.6486056 + 0.0657098244d + 1.00273791t \tag{4.2}$$

Table 4.9: Cartesian coordinates of DSS13 and DSS14 in the ITRF93 reference frame.

telescope	x(m)	y(m)	z(m)
DSS13	-2351112.491	4655530.714	+3660912.787
DSS14	-2353621.251	4641341.542	+3677052.370

Table 4.10: Quasar coordinates (J2001.5 epoch).

quasar	right ascension	declination
3c84	3h 19m 51.37s	41°30′46.83″
3c147	5h 42m 43.3s	49°51′9″
3c48	1h 37m 46.5s	33°10′2″
3c273	12h 29m 11.3s	2°2′38″
3c286	13h 31m 12.5s	30°30′4″
3c454	22h 54m 3.561s	16°9′23.34″

where GMST is the Greenwich Mean Sidereal time, d is the day number, and t is the Universal Time (UT) in hours. Then, the hour angle h is given by [41]

$$h = \text{GMST} + \text{equation of equinoxes} - \alpha \tag{4.3}$$

where α is the right ascension of the source and the equation of equinoxes is tabulated in the Astronomical Almanac.

We have used a total of six quasars throughout the experiment. Their coordinates are given in Table 4.3.2. I show the quasar and cable delay data for single-quasar nights in Tables 4.11, 4.12, 4.13, and 4.14. Data from multiple quasar nights is shown in Tables 4.15, 4.16, 4.17, and 4.18. The data in these tables shows that the delays for different quasars are no more than 7 ns apart for

Table 4.11: Cable delay and cross-correlation for single-quasar runs,2000

Date	quasar	UT	cross correlation (μs)	geometric delay (μs)	cable delay (μs)
9 September	3C273	00:35:45	138.394	1.983	136.411
30 September	3C273	17:18:27	90.357	-46.072	136.429
1 October	3C273	20:41:09	110.751	-25.684	136.435

Table 4.12: Cable delay and cross-correlation for single-quasar runs,2001

Date	quasar	UT	cross correlation (μs)	geometric delay (μs)	cable delay (μs)
12 March	3C273	09:40:06	106.252	-30.202	136.454
13 March	3C273	07:39:16	92.840	-43.615	136.455
14 March	3C273	07:58:48	94.642	-41.809	136.451
11 May	3C273	06:18:40	111.824	-24.588	136.412
12 May	3C273	06:13:07	111.593	-24.871	136.464
13 May	3C273	07:47:32	130.672	-5.798	136.470

any given night. The maximum differential delay from the moon is 637 ns, which is far larger than our timing resolution.

4.3.3 Amplitude Calibration

We calibrate the amplitude by the standard methods of radio astronomy, referencing to a thermal noise source (noise diode) at a calibrated temperature. The measured system temperature during a run fixes the value of the noise level and therefore the electric field scale. We also check linearity of the transient response

Table 4.13: Cable delay and cross-correlation for single-quasar runs,2002

Date	quasar	UT	cross correlation (μs)	geometric delay (μs)	cable delay (μs)
3 March	3C273	06:51:54	90.273	-46.032	136.305
4 March	3C273	10:33:36	109.399	-26.900	136.299
17 April	3C147	16:55:06	165.004	28.672	136.332
2 May	3C273	08:31:46	130.495	-5.808	136.303
4 May	3C273	08:21:00	129.900	-6.410	136.310
16 November	3C273	21:26:16	154.707	18.392	136.315

Table 4.14: Cable delay and cross-correlation for single-quasar runs,2003

Date	quasar	UT	cross correlation (μs)	geometric delay (μs)	cable delay (μs)
8 April	3C84	21:59:27	143.130	6.815	136.315
25 May	3C286	09:58:09	177.330	41.017	136.313
24 August	3C273	19:32:49	90.191	-46.107	136.298

Table 4.15: Cable delay and cross-correlation from 22 June 2001.

quasar	UT	cross correlation (μs)	geometric delay (μs)	cable delay (μs)
3c84	13:09:1.731	138.776	2.288	136.488
3c147	14:22:2.263	153.658	17.175	136.483
3c48	14:40:2.831	129.908	-6.573	136.481

Table 4.16: Cable delay and cross-correlation from 01 October 2001.

quasar	UT	cross correlation (μs)	geometric delay (μs)	cable delay (μs)
3c273	00:31:30	155.173	18.677	136.498
3c286	00:42:15	169.303	32.808	136.497

Table 4.17: Cable delay and cross-correlation from 28 May 2002.

quasar	UT	cross correlation (μs)	geometric delay (μs)	cable delay (μs)
3c273	05:33:27	115.440	-20.865	136.305
3c454	13:57:58	112.114	-24.196	136.311

Table 4.18: Cable delay and cross-correlation from 10 November 2002.

quasar	UT	cross correlation (μs)	geometric delay (μs)	cable delay (μs)
3c273	18:34:00	114.918	-21.399	136.317
3c286	18:51:57	136.989	0.677	136.312

by varying the attenuation of the monocycle generators (see Section 4.3.1), ensuring that the entire system has the dynamic range required to see large pulses.

4.4 RFI Elimination

The first step in the analysis is to eliminate RFI events. I developed cuts for RFI using the data sample from September 2000 to March 2002, described in the following sections.

4.4.1 T-closest

The oscilloscopes used to record the data have a 6 second holdoff or deadtime after a trigger in order to record the data. This holdoff is much smaller than the mean expected time between thermal triggers (two minutes or more, depending on the singles rates). We observe that during runs with heavy RFI, triggers tend to come in at a rate much faster than the thermal rate. The fastest possible trigger rate is one every six seconds.

Figure 4.6 shows histograms of the values of "t-closest", which is defined as the time between any given trigger and its closest neighboring trigger, either earlier or later. Figure 4.6 shows a histogram of all t-closest values for all good data from September 1, 2000 to November 27, 2001 (73 hours livetime, over half of the full 123 hour data set). Figure 4.6 also shows the histogram for the first minute only, with one second per bin; there is an excess of events at 6 and 7 seconds.

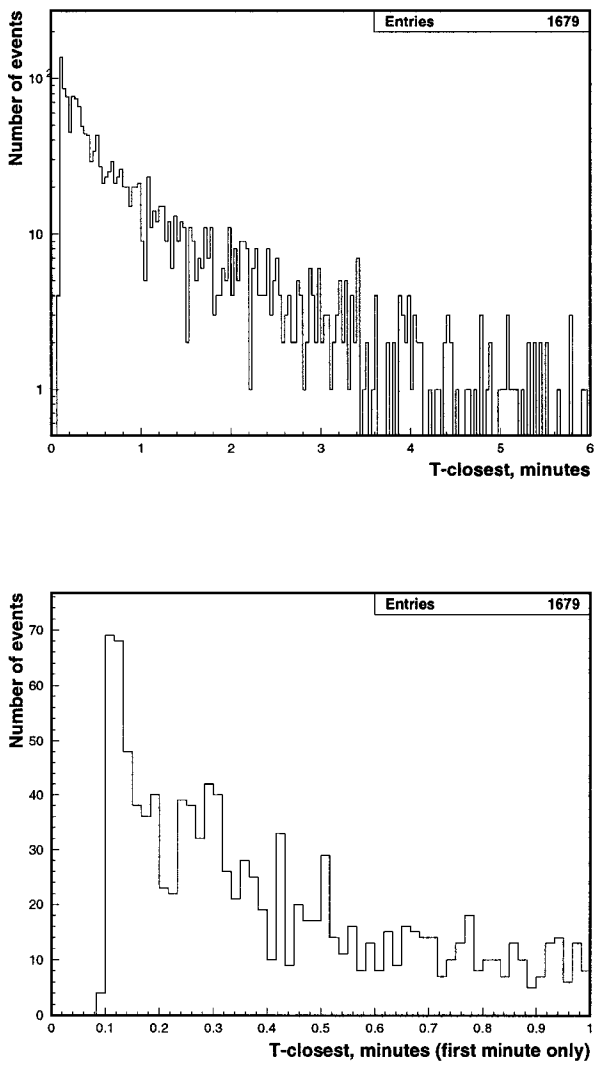

Figure 4.6: Histograms of t-closest. Top: all events, 2 seconds per bin. Bottom: first minute only, one second per bin.

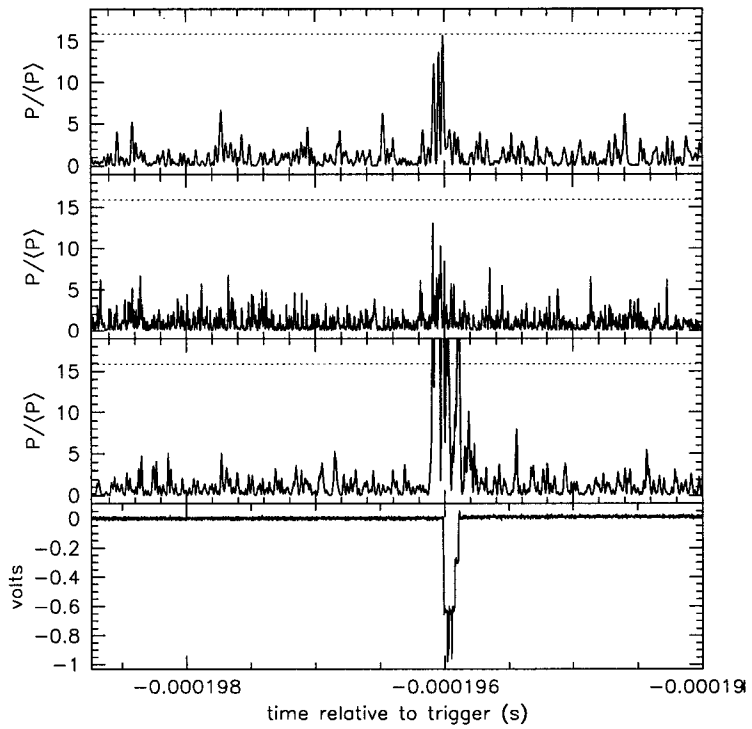

Figure 4.7: Typical RFI event at DSS14. From the top: DSS14 LCP, DSS14 RCP, L-band and the sum of the local triggers at DSS13 and DSS14. Note that the L-band signal is inherently 1.3 μs early compared to the LCP and RCP signals.

4.4.2 L-band Power

The L-band arrives 1.36 μs earlier than the master trigger for all 2001 runs. I calculated the normalized L-band power for any given event by summing the L-band power in the first 1000 ns after the beginning of the L-band event (defined as 1.36 μs prior to the master trigger), and dividing by the sum of the L-band power in the first 1000 ns of the window. An event with no unusual amplitude in L-band ought to have a normalized L-band power value around 1. Figure 4.7 shows a typical RFI event at DSS14, with the corresponding strong L-band signal.

Figure 4.8 shows a plot of normalized L-band power vs. t-closest for various runs from March, May and June 2001. The solid points are visually confirmed to be RFI; the open points are not visually obvious RFI. For some RFI events, the normalized L-band power is well above 1. For others, the t-closest value is very small (in fact, six seconds) although the normalized L-band power is not especially high.

Figure 4.9 shows all events from 03 March 2002. This was an RFI-heavy run with an active L-band veto. Approximately 50% of the events from this run are RFI. The plot of normalized L-band power vs. t-closest shows a clear separation between RFI and non-RFI events in L-band power, with no RFI event having an L-band value less than 2. Note that no RFI event in either plot has a t-closest greater than 3 minutes.

Based on these plots, I make the following cuts:

- I cut all events with t-closest of less than 8 seconds.
- For t-closest less than three minutes, I cut all events with a normalized L-band power of 2 or greater.
- For t-closest greater than three minutes, I make no cut, just in case a neutrino event has an L-band signal, since there is no RFI with a t-closest that high and a large t-closest indicates an RFI-quiet time in general. Any remaining RFI would probably not be in time with the moon.

4.4.3 Efficiency

The average trigger rate from 01 September 2000 to March 2002 is one trigger every 2 minutes. This implies that the efficiency of the proposed t-closest cut, which eliminates two one-second intervals, is (120-2)/120, or 98%.

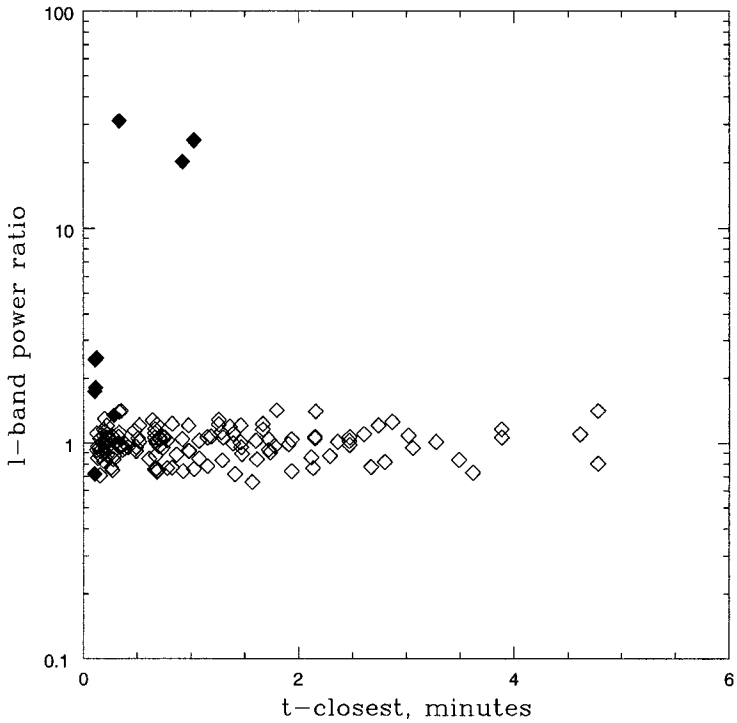

Figure 4.8: L-band power vs. t-closest for selected March, May and June 2001 runs. Filled dots are visually confirmed RFI events at DSS14.

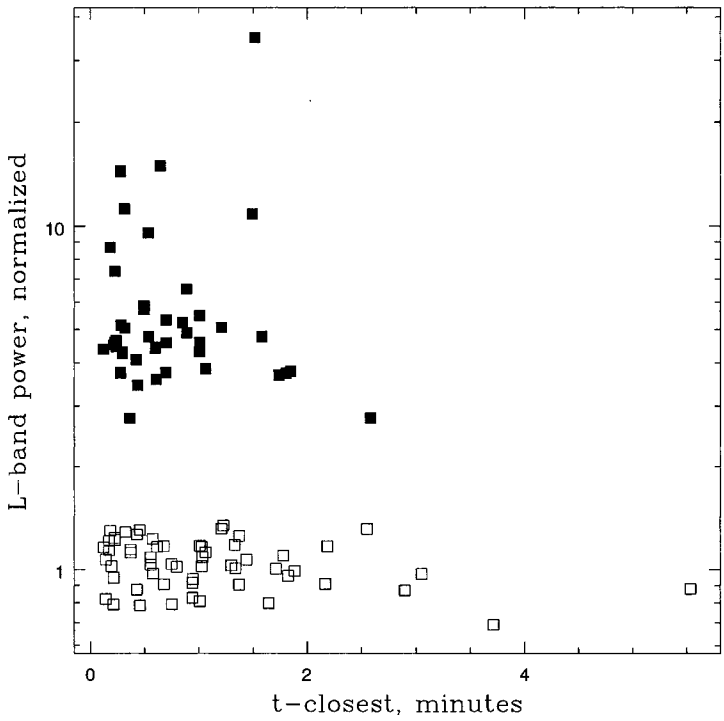

Figure 4.9: L-band power vs. t-closest for 03 March 2002 run. This was a heavy-RFI run with an active L-band veto, resulting in about half RFI and half non-RFI triggers. Filled dots are visually confirmed RFI events at DSS14.

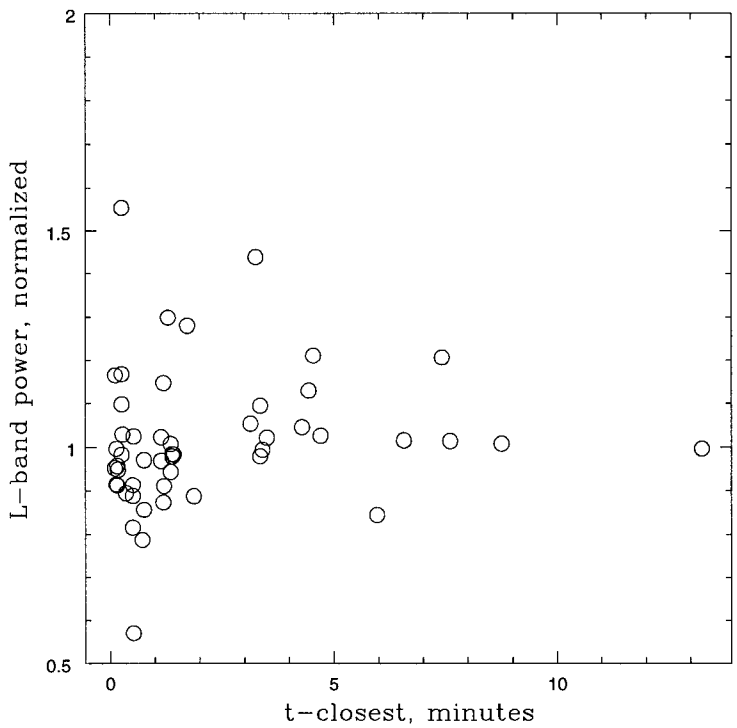

Figure 4.10: L-band power vs. t-closest for 30 September 2001 run. This run was chosen for its very low RFI activity.

To study the efficiency of the L-band cut, I looked at the 50 events from 30 September/ 01 October 2001, which was a very low RFI run. Figure 4.10 shows the plot of normalized L-band power vs. t-closest for this run. None of the events have a normalized L-band power greater than 2, so none of these events would be cut, implying 100% efficiency. At a 90% confidence level, the efficiency is greater than 95%.

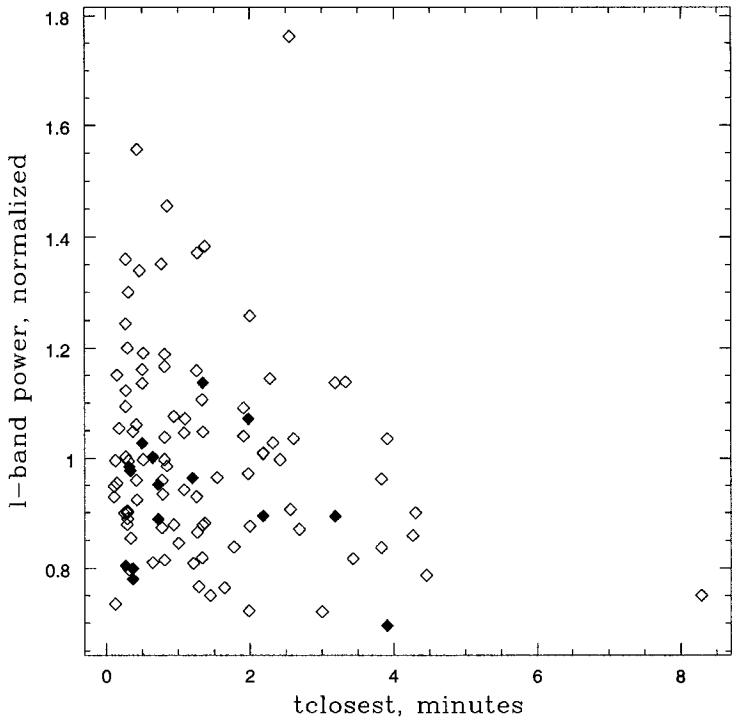

Figure 4.11: L-band power vs. t-closest for 14 March 2001 run. This run was chosen for heavy RFI activity at DSS13. Filled dots are visually confirmed RFI at DSS13.

4.4.4 RFI at DSS13

The RFI cut on L-band and t-closest is not efficient at eliminating RFI events at DSS13. Figure 4.11 shows a plot of L-band power vs. t-closest for 14 March 2001, a night with heavy RFI at DSS13. The filled dots are visually obvious RFI events at DSS13. None of them make the t-closest or L-band power cut.

At DSS13, there is no independent RFI monitor as there is at DSS14. We want to cut RFI without eliminating potential neutrino events. To that end, I make use of the band-limited property of Askar'yan's effect. We expect that a

neutrino pulse would be band-limited. The bandwidths of DSS13 Hi and DSS13 Lo are about 60 MHz, which means that a neutrino pulse should be on the order of tens of nanoseconds long. A typical RFI pulse, by contrast, is often several hundred nanoseconds long.

Figure 4.12 shows a typical RFI event at DSS13. The pulse begins about 100 ns before the trigger (t = 0) and ends about 300 ns after. The plot shows P/P_{av} vs. time. We would expect an RFI pulse to have more bins above a given value of P/P_{av} in that window than a thermal pulse. Figure 4.13 shows plots of the number of bins above four values of P/P_{av} for DSS13 Lo from 14 March 2001. The window is from -200 to +300 ns with respect to t = 0. There is good separation between obvious RFI and non-RFI events for $P/P_{av} = 10$ or 15. Therefore I cut events with more than 10 bins where $P/P_{av} > 15$. Figure 4.14 shows the plot of number of bins above $P/P_{av} = 15$ for 30 September 2001, an RFI-quiet run. None of the events make the cut of 10, implying 100% efficiency or greater than 95% efficiency at the 90% confidence level.

The final RFI cut is therefore:

- I cut all events with t-closest less than 8 s.
- I cut all events with t-closest between 8 s and 3 minutes.
- At DSS14, I cut all events with L-band power greater than 2.
- At DSS13, I cut all events with more than 10 bins that have P/P_{av} greater than 15.
- No cuts are made on events with t-closest greater than 3 minutes.

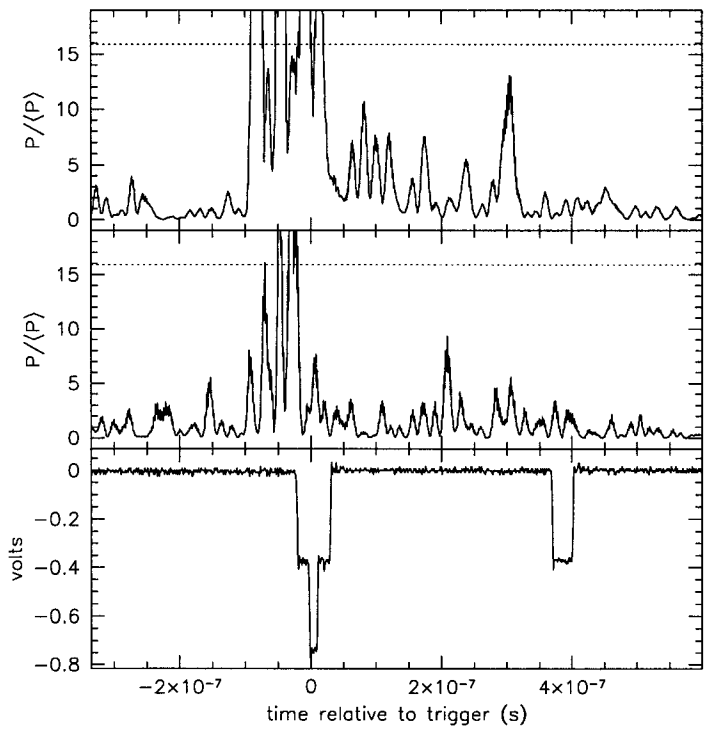

Figure 4.12: RFI event at DSS13. From the top: DSS13 Lo, DSS13 Hi, L-band and the local trigger at DSS13.

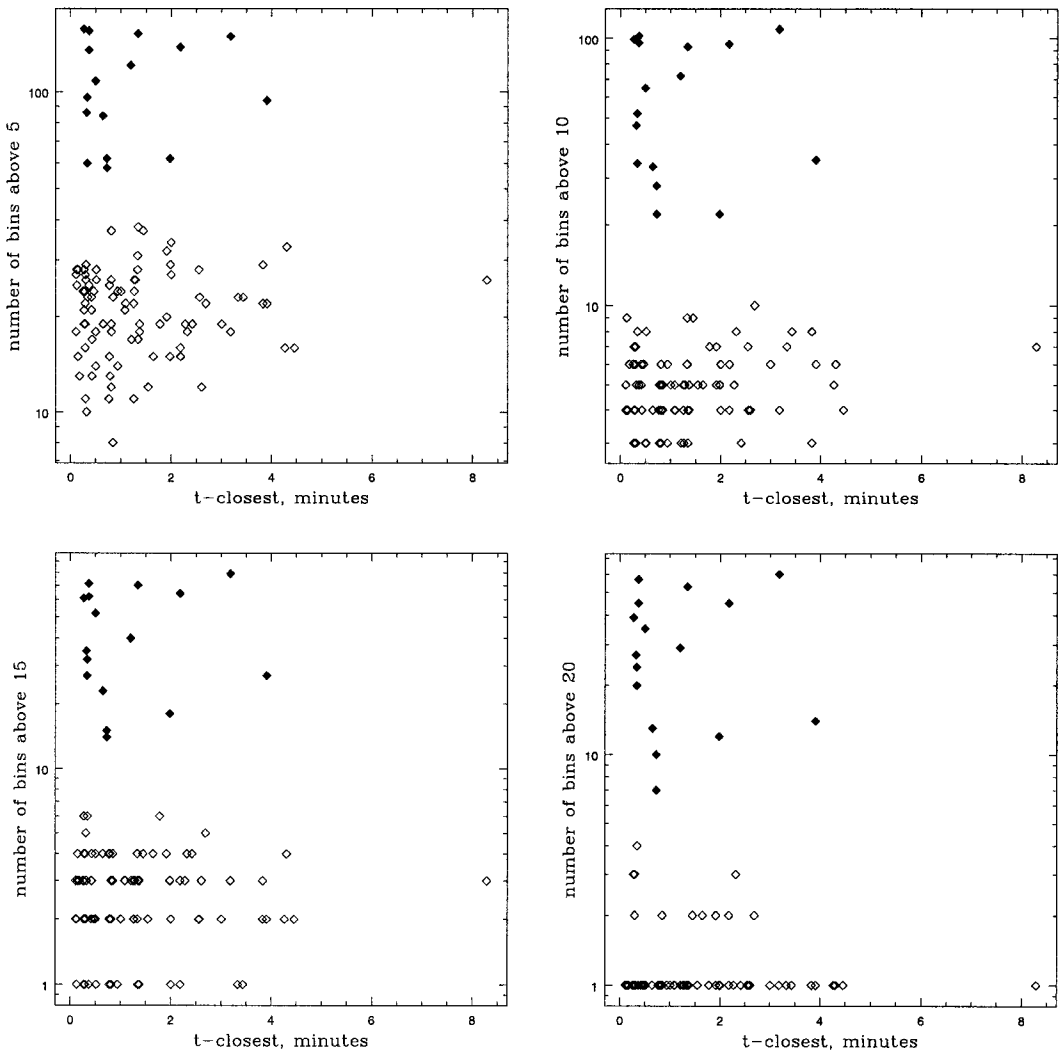

Figure 4.13: Clockwise from top left: number of bins above 5, 10, 15 and 20 in normalized power, vs. t-closest, for DSS13 Lo on 14 March 2001. Filled dots are visually confirmed RFI at DSS13. A cut will be made on the number of bins above 15 greater than 10 at DSS13.

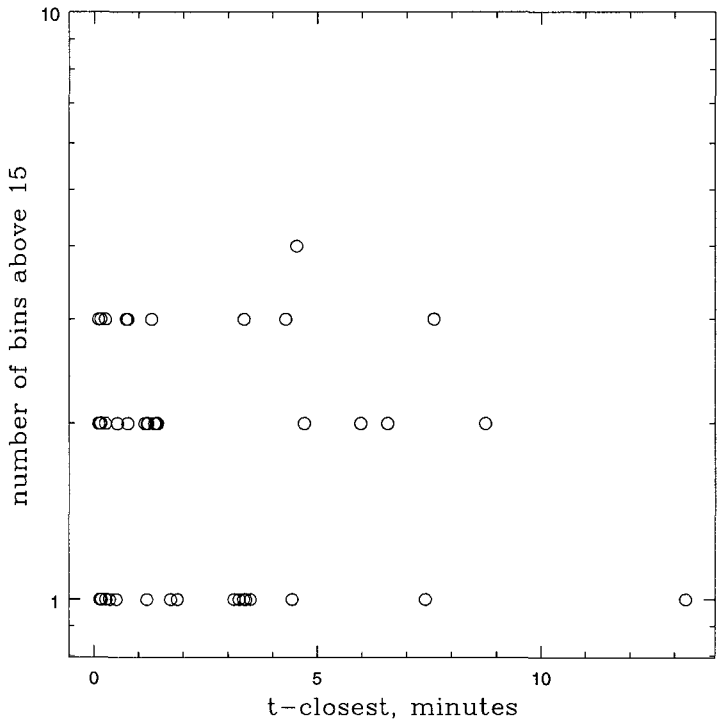

Figure 4.14: Number of bins above 15 for 30 September 2001, the RFI-quiet run.

4.5 Event Analysis

Having made the RFI cuts, I proceed to the final data reduction of the thermal events. Figure 4.15 shows the squared voltage trace for typical thermal events at DSS13 and DSS14. The top figures have been smoothed with a boxcar smoothing function over 7 ns for DSS14 LCP, 4 ns for DSS14 RCP. The times correspond to the inverse of the center frequency of the bandpasses. This eliminates the "jitter" from the IF frequency, seen in the un-smoothed data (bottom). Smoothing also makes the signal which triggered the system visually clearer. (In both DSS13 and DSS14, the signal appears about 100 ns before the trigger in the bottom panel.) I then cut on local timing and amplitude.

4.5.1 Local Timing Cut

I measured the relative timing between local signals (DSS13 Hi and Lo, DSS14 LCP and RCP) by looking for the peak power value in a 125-ns window before the trigger. I used the smoothed data for this measurement since the timing of the smoothed pulse is cleaner. Smoothing only affects the amplitude of the peak, not the relative timing. I correct for inherent timing difference between the signals, which is measured with monocycles (DSS13 Hi and Lo) and the moon rim (DSS14 LCP and RCP). Typically the local timing difference is less than 10 ns. Different calibration methods are consistent to within 10 ns.

Ideally, the relative timing of the signal in DSS13 Hi and DSS13 Lo or DSS14 LCP and DSS14 RCP should have a flat distribution limited by the size of the local coincidence window. However, linear polarization can cause overlap in LCP and RCP, and there is some overlap in the bandwidths of DSS13 Hi and DSS13 Lo. Figure 4.16 shows relative timing distribution histograms for DSS13 and

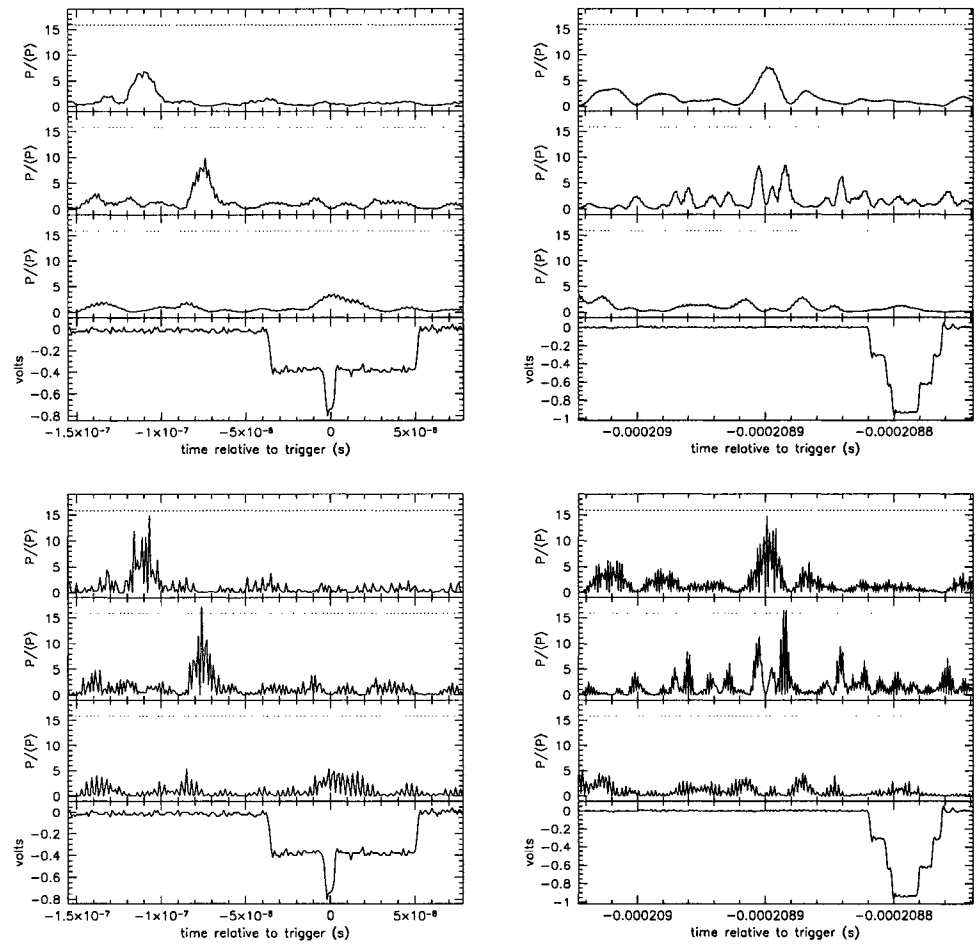

Figure 4.15: Top: thermal events at DSS13 (left) and DSS14 (right), smoothed. Bottom: the same events, unsmoothed. The panels in DSS14 are (from the top) DSS14 LCP, DSS14 RCP, L-band and the sum of local triggers at DSS13 and DSS14. The panels in DSS13 are (from the top) DSS13 Lo, DSS13 Hi, L-band and the local trigger at DSS13.

DSS14, with a possible peak near t = 0 which may come from the overlap. I cut on t < 20 ns.

4.5.2 6σ Cut

To look for DSS14 RCP-equivalent 6 σ thermal events, I used the unsmoothed voltages, since smoothing reduces the amplitude and unsmoothed data has simpler statistical properties. I looked for the peak absolute value of the voltage in the same 125-ns window that I used for the timing cut, and divided by the root-mean-square voltage from the first microsecond at the beginning of the event trace.

The definition of a 6 σ event depends on the bandwidth of the channel. The bandwidths of DSS14 LCP, DSS14 RCP, DSS13 Hi and DSS13 Lo are 40, 150, 75 and 75 MHz respectively. The signal-to-noise ratio is proportional to the square root of the bandwidth, so a 6 σ event in DSS14 RCP would be a 3 σ event in DSS14 LCP and a 4 σ event in DSS13 Hi and Lo. I found no events over 6 σ anywhere in the data sample. This includes events whose timing is not consistent with the moon. This shows that this technique is background-free, and the sensitivity increases linearly with time. In Section 4.6 I calculate the sensitivity in units of km^3-sr and set a physics limit on the isotropic neutrino flux based on the negative result.

4.5.3 Small Event Analysis

If we see no large neutrino events and eliminate RFI, then we expect to see a fairly flat background of uncorrelated thermal signals from DSS13 and DSS14 when we loosen the amplitude cut. An early analysis (50 hours livetime) of 4σ and larger events shows a peak of 10 events between -1 and -2 μs with respect

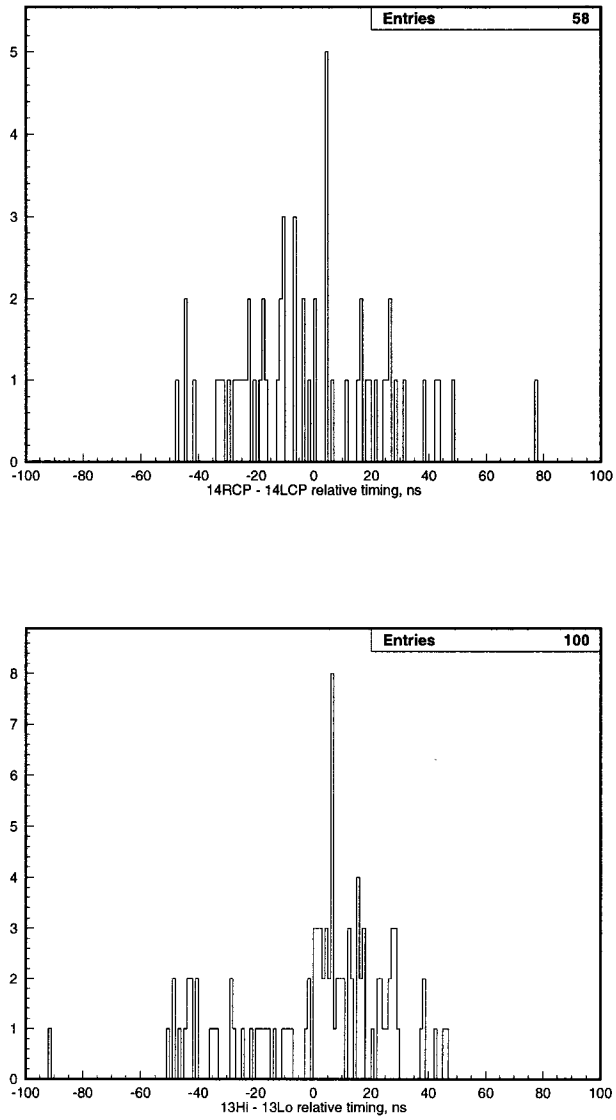

Figure 4.16: Top: timing distribution for DSS13 (Hi - Lo). Bottom: timing distribution for DSS14 (RCP - LCP).

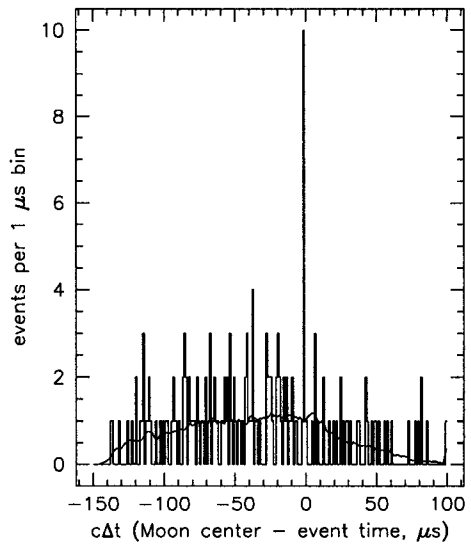

Figure 4.17: Small event analysis histogram for 50 hours of data. The overlain histogram (solid line) is the expected background level. Courtesy of Chuck Naudet.

to zero moon delay. Figure 4.17 shows the histogram from this analysis [44], along with the expected background level. We obtain the expected background by randomizing the time of the event sample. However, the events in this peak nearly all occur prior to June 2001. Figure 4.18 shows two histograms, one for September 2000 to June 2001, the other for runs after June 2001. At this time we began running GLUE in the half-limb defocused configuration, but in 2002 we returned to running in the limb focused configuration. Therefore the change in configuration does not seem to be responsible for the disappearance of the peak.

I performed a small event analysis using my own RFI cut and my own timing analysis. For comparison, I also did an analysis which eliminated RFI visually. My RFI cut includes two cuts which are not in the first analysis, based on the time difference between any event and its closest neighbor within a given run,

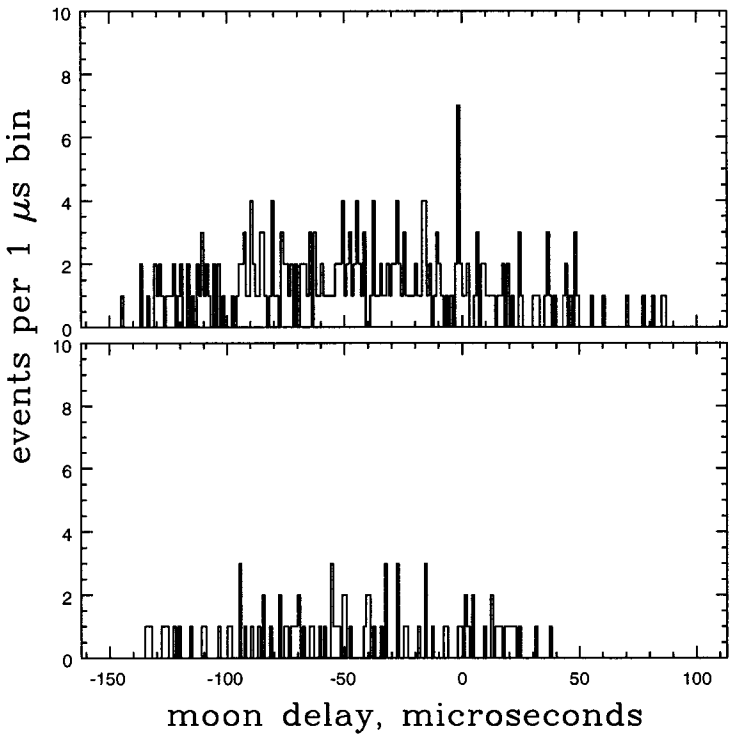

Figure 4.18: Top: small event analysis for September 2000 through June 2001. Bottom: small event analysis for June 2001 through August 2003.

called t-closest. Since RFI sometimes comes in bursts limited only by the six-second holdoff in the oscilloscopes, I eliminate any event which is closer than 8 seconds to its nearest neighbor. I also do not perform any RFI cut on an event which is more than three minutes away from its nearest neighbor. This does allow some events with RFI characteristics into the sample. The other RFI cuts are based on L-band amplitude at DSS14 and pulse width at DSS13.

Figure 4.19 shows my small event analysis using the RFI cut both with and without the t-closest cuts, as well as the visual RFI cut, for September 2000 through June 2001. All three plots also have identical local timing and amplitude cuts. The amplitude cut is a cut on the sum of the DSS14RCP + DSS14LCP normalized power amplitude (cut any event with sum less than 22, which corresponds to a 4σ event). The local timing cut is on time difference greater than 27 ns for DSS14 RCP and LCP, and greater than 20 ns for DSS13 hi-band and lo-band, in order to agree with the first analysis. Tightening the amplitude cut or loosening the local timing cuts causes the peak to fall and the background to rise.

The visual RFI plot, and the plot with no t-closest cut, show the same 8 events in the -1 to -2 μs bin. The two events which are in the first analysis but not in mine show up slightly outside the -1 to -2 bin in my analysis, with times 30 to 50 ns different than in the first analysis, due to individual differences in calculating the moon delay. The plot with the t-closest cut has 7 events in this bin, as one of the ten events in the first analysis fails the t-closest cut. Freezing the cuts there and expanding the analysis to use all good data, the background rises considerably with respect to the peak. Figure 4.20 shows the plot using my RFI cut with my t-closest cut, for all data so far.

In conclusion, I see the -1 to -2 μs peak in my analysis, but with smaller

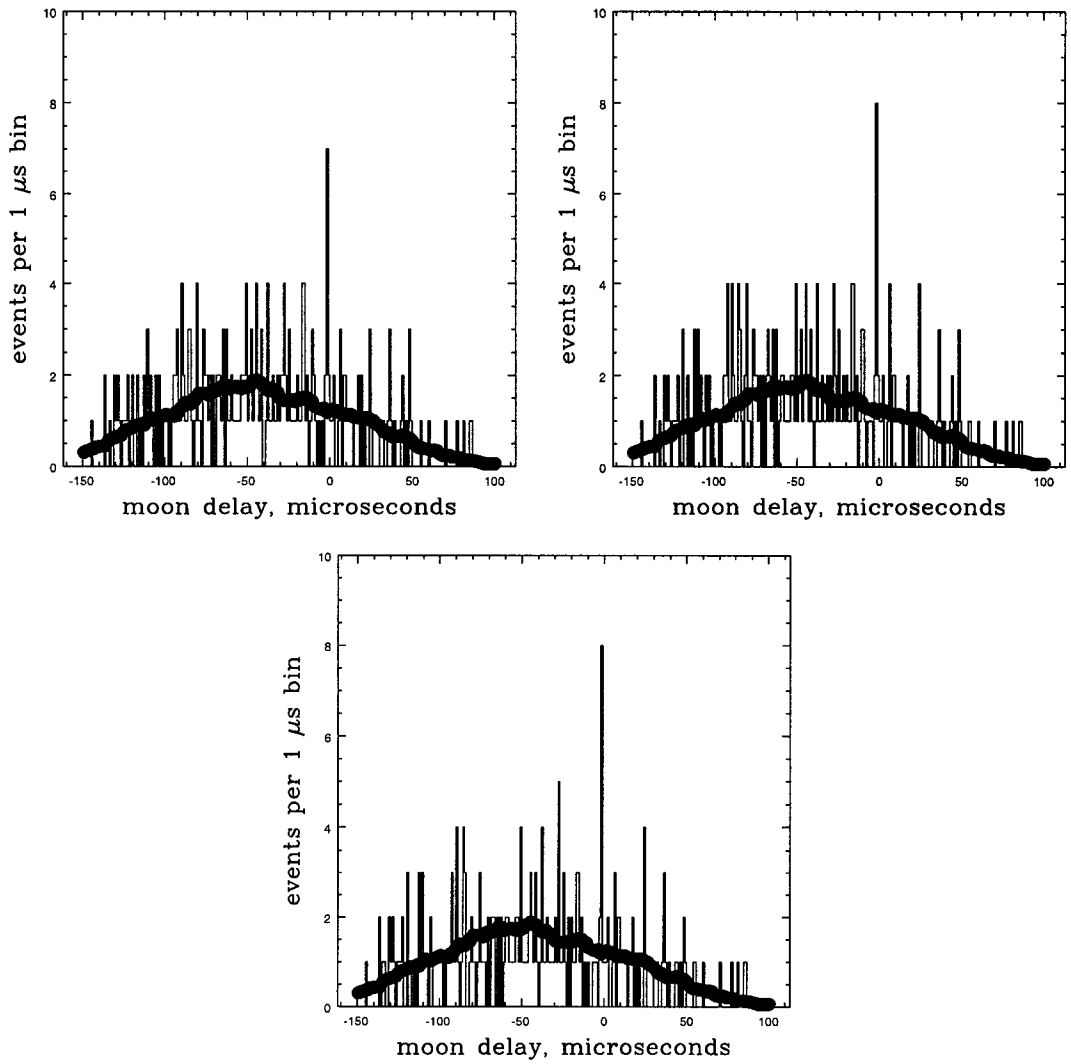

Figure 4.19: Small event analysis for September 2000 through June 2001. Top left: RFI cut with t-closest cuts. Top right: RFI cut without t-closest cuts. Bottom: visual RFI cut. Expected background level is the heavy solid line.

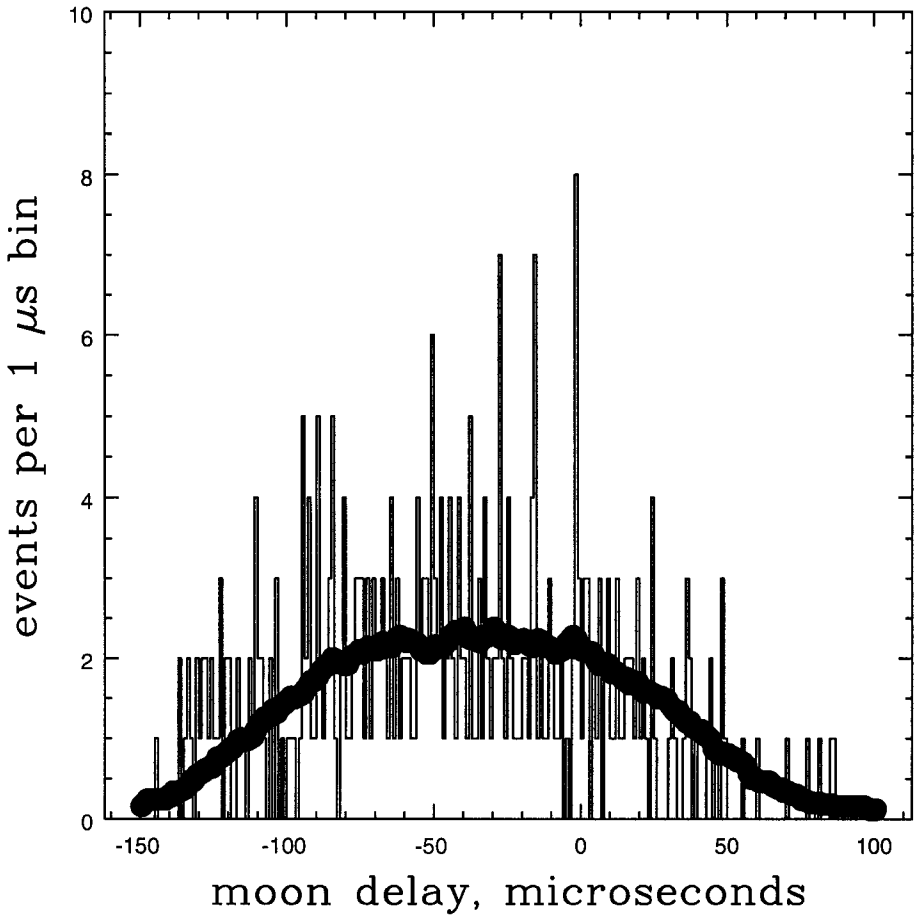

Figure 4.20: Small event analysis for September 2000 through August 2003, using my RFI cut without the t-closest cut. Expected background level is the heavy solid line.

statistical significance than the original peak. It is not robust to differences in cuts and moon delay timing. With increased data taking, the peak disappears as the background rises.

4.6 Goldstone Monte Carlo

From the 6σ analysis, we see no evidence of bandlimited, linearly polarized signals consistent with neutrinos interacting in the lunar regolith. In order to set an upper limit on isotropic neutrino fluxes, we must determine the aperture of the detector. This requires a Monte Carlo (MC), since the geometry is complicated. The aperture calculation has two pieces: the efficiency and the normalization. The efficiency is the number of events seen by Goldstone per number of neutrinos interacting in the moon, and the normalization is the aperture of the moon if it were equal to that of a perfect "black sphere".

4.6.1 Efficiency

We treat the moon as a sphere bathed in an isotropic flux of neutrinos. The neutrino's entrance point into the Moon is chosen flat in surface area, *i.e.*, it is flat in $d\cos\theta_m\ d\phi_m$ where θ_m is the lunar co-latitude and ϕ_m is the lunar longitude of the entrance point. We place the Earth and the Moon in a selenocentric coordinate system: Cartesian, centered on the moon center. The z-direction is upward, the Earth is in the positive y-direction and the x-direction is such that the coordinate system is right handed.

The neutrino direction vector is generated flat in $d\theta d\phi$ where θ is measured down from the z axis and ϕ from the x axis in the xy plane. Each event is then weighted by a factor of $\sin\theta\cos\theta$, which is equivalent to generating the neutrino

direction flat in $\cos\theta d(\cos\theta)d\phi$. This is the probability density function for an isotropic flux on a flat patch of surface. The z axis in this case is the surface normal of the entrance point on the moon, so we rotate the neutrino direction vectors through the matrix that sends (0,0,1) to ($\cos\phi_m \sin\theta_m$, $\sin\phi_m \sin\theta_m$, $\cos\theta_m$). Given the entrance point and direction, we calculate the exit point and chord length c. At this point if the neutrino is heading out of the "dark side" of the moon (*i.e.*, $n_y < 0$) then we generate a new neutrino. We multiply the weight for all events by 0.5 correspondingly.

For each MC run, we generate neutrinos for a single energy. The other running parameters are the pointing (limb, half-limb, or center) and the DSS14 antenna radius (17 m for defocused, 35 m for focused). The program is properly weighted with the proportion of each configuration in the final data set.

The chord length in kg/m^2 is calculated by stepping along the moon in 50 km steps from x_{in}, y_{in}, z_{in} to $x_{out}, y_{out}, z_{out}$. The moon density profile is taken to be:

$$\begin{aligned}
\rho &= 7870 \text{ kg/m}^3 && |r| < 500\text{km} \\
\rho &= 3700 \text{ kg/m}^3 && 500\text{km}|r| < 1000\text{km} \\
\rho &= 3300 \text{ kg/m}^3 && 1000\text{km} < |r| < 1670\text{km} \\
\rho &= 2900 \text{ kg/m}^3 && 1670\text{km} < |r| < 1750\text{km} \\
\rho &= 1800 \text{ kg/m}^3 && \text{(regolith)}
\end{aligned}$$

Note that this integrates to 0.97 of the total moon density which is better known than the density of each layer, so the densities of the layers are actually renormalized by this factor.

Given the chord length c, we can calculate the interaction length if the cross

section is known. We use the total cross section formula from Gandhi *et al.* [19]:

$$\sigma = 7.80 \times 10^{-40} \mathrm{m}^2 (\frac{E_\nu}{10^9 \text{ eV}})^{0.363}$$

We determine, based on the chord length (in $\mathrm{kg/m^2}$) and interaction length (in $\mathrm{kg/m^2}$), if this neutrino interacts in the moon. If not, the event counts as a miss and we get a new event. However, at these high energies the neutrino always interacts. Now that we know we have a chord with an interaction along it, we choose an interaction location. For energies above 10^{20} eV, this can be done with a rejection technique. We choose an interaction point d along the chord according to an exponential $\exp(-d/\tau)$, where τ is the interaction length. The maximum shower position is taken to be the neutrino interaction location. Figure 4.21 shows the position of the events along the chord for three energies. As energy increases, events are less likely to happen toward the end of the chord.

We then find the angle at which the event is viewed inside the regolith, *i.e.*, after refraction. We also need the distance, d, traveled by the radio emission in regolith. First note that any shower we will see is very near to the surface compared to the Earth-moon distance. Hence we can use $x_{out}, y_{out}, z_{out}$ as a good approximation to where the RF emerges (*i.e.*, the curvature of the moon's surface is small over several meters scale). We put the antenna on the surface of the Earth at Goldstone's latitude and assume the moon is at moon noon in longitude. We draw a vector from the antenna to the exit point on the moon. Assuming the moon's surface is flat for now (we randomize later) only one refraction angle is possible. Since the location of the shower is known and the angle it is viewed from is known one can solve for both: d and the real emergent point of the radio emission. In principle this process could be iterated but the Earth-moon distance is so large compared to the depth of the regolith that it is not necessary.

The normal vector to the surface found above assumes the Moon is a smooth

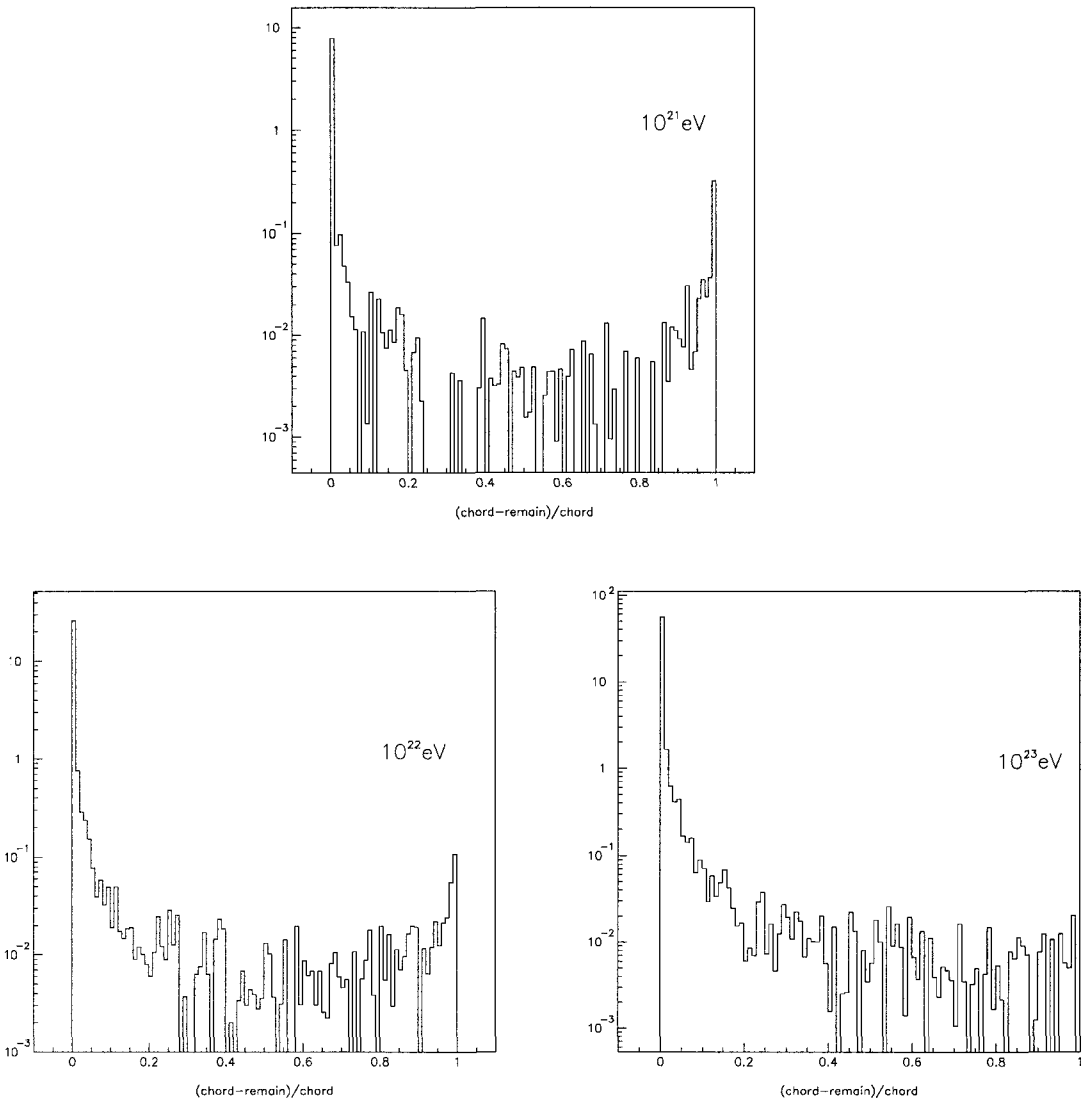

Figure 4.21: Clockwise from top: position of shower along chord 10^{21}, 10^{22}, and 10^{23} eV.

sphere. We randomize each component of the direction vector by 20% and renormalize, which gives a 10° average roughness [45]. The refraction is done as a 3-dimensional problem using the following formula [46]:

$$\mathbf{n}_{refr} = -\left(n^{-1}\cos\theta_i - \sqrt{1-(n^{-1}\sin\theta_i)^2}\right)\mathbf{n}_s + n^{-1}\mathbf{n}_{dss}$$

where $\mathbf{n}_{refr}$ is the refracted vector, n is the index of refraction, $\mathbf{n}_s$ is the surface normal vector, θ_i is the angle between the surface normal and the normal vector to the telescope, and $\mathbf{n}_{dss}$ is the normal vector to the telescope. The viewing angle, θ_V, is the angle between $\mathbf{n}_{refr}$ and the neutrino direction.

Upon refraction, the image of the Cherenkov cone is magnified. The incident electric field is multiplied by a factor of

$$\sqrt{\frac{\tan\theta_I}{\tan\theta_T}(1-r^2_{\|,\perp})} \tag{4.4}$$

where $r_{\|}$ is the Fresnel coefficient for the "pokey" case:

$$r_{\|} = \frac{\tan(\theta_I - \theta_T)}{\tan(\theta_I + \theta_T)} \tag{4.5}$$

I defer a discussion of Equation 4.4 to the appendix of this dissertation.

Using the parameterization for the regolith given by Alvarez-Muniz and Zas [36], we calculate the radio emission for the center frequency (2.25 GHz).

$$\text{V/m/MHz @ 1m} = (1.5\times10^{-7})\times\frac{E_\nu}{1.\times10^{12}\text{eV}}\times\left(\frac{\nu}{\nu_0}\right)\times\frac{1.}{(1.+(\nu/\nu_0)^{1.44})} \tag{4.6}$$

where $\nu_0 = 2.7$ GHz. We convert the V/m/MHz @1m to V/m/MHz at the antenna by dividing by the distance between the antenna and shower. We also account for the attenuation in the regolith:

$$\text{V/m/MHz} = \text{V/m/Mhz}\times\exp(-\text{distance/attenlength})$$

where the attenuation length $= 9.0 * (2.25\times10^9/\nu)$, where $\nu = 2.25$ GHz.

Before calculating the angular thickness of the cone we need to know the neutrino flavor and interaction type so we know if the LPM correction applies or not. We take an equal mix of ν_e, ν_μ and ν_τ. We take 70.64% of the interaction to be charged-current and the rest to be neutral-current. The inelasticity spectrum is taken as a rough parameterization of the spectrum in Gandhi *et al.* [47] with some license in the functional form to make the random selection from the distribution fast. We assume the τ produced by ν_τ CC is so energetic that it interacts before decaying and therefore is like a muon and we do not see its energy.

- Electromagnetic (EM) Showers:

  For EM showers, we calculate the LPM energy, E_{LPM} [48]:

  $$E_{LPM} = 7.7 \times 10^{14}\text{eV/m} \times_0 (rego)$$

  Then the angular thickness of the cone is given by [49]

  $$\Delta\theta = 2.7^\circ \frac{\nu_0}{\nu} \left(\frac{E_{LPM}}{0.14E_\nu + E_{LPM}} \right)^{0.3}$$

  where $\nu = 2.25$ GHz. Note that this ν_0 is different from ν_0 in Equation 4.6. We scale ν_0 from [49], where ν_0 is given for water ice, and scale by the radiation lengths to obtain ν_0 for the regolith:

  $$\nu_0 = 500 \times 10^6 \frac{X_0(\text{water})}{X_0(\text{rego})}$$

  i.e., the cone gets fatter as the shower gets shorter, which happens for shorter radiation lengths.

- Hadronic Showers: For hadronic showers, the angular thickness of the cone is given by a fairly complex formula from Alvarez-Muniz and Zas [50] that we only write here for the energies in question:

  $$\epsilon = \log_{10}(\frac{E}{1\text{TeV}})$$

$$\Delta\theta = 1^\circ \frac{\nu_0}{\nu}(4.23 - 0.785\epsilon + 0.055\epsilon^2)$$

Again we scale ν_0 as above. It is not clear that this parameterization works beyond 10^{19} eV, so we take the value at 10^{19} eV and increase it by 7.5% per decade in energy, which is the observed slope [50]. It is a small correction which we are getting mostly right.

Given that we know the Cherenkov angle, θ_C and viewing angle θ_V from above, we use the parameterization of the cone thickness (modeled by Alvarez-Muniz and Zas [51] as a Gaussian) to obtain the electric field seen:

$$\text{V/m/MHz} \rightarrow \text{V/m/MHz} \times \exp(-\ln(2)(\frac{\theta_C - \theta_V}{\Delta\theta})^2)$$

We sum the electric field from the electromagnetic and hadronic energies after accounting for different roll-off with viewing angle.

We then calculate the angular response of the antenna. The MC can be set for the antenna to be pointing at the upper limb, half-limb or moon center, which fixes a direction vector. The angle θ_{off} between this vector and the line between the antenna location on earth and the shower position measures how far off-beam the shower is. The electric field response is then given by the Airy pattern:

$$x = \frac{2\pi}{\lambda} R \sin(\theta_{off})$$
$$\text{E-resp} = \frac{J_1(x)}{x}$$

where J_1 is BESJ1 in CERNLIB and R is the radius of the antenna, taken to be 17 m (defocused) or 35 m (focused) and λ is 0.136 m. We multiply the electric field by E-resp to account for how far off-beam the shower is.

We convert V/m/MHz to V/m by multiplying by the bandwidth of each channel.

We need to convert V/m to V by using the effective height of the antenna. We take the effective aperture, A_{eff} to be $0.75\pi R^2$ where R is the antenna radius and 0.75 is the aperture efficiency (*i.e.*, that part of the efficiency accounting for blocking of the aperture and ohmic losses. Phase errors are included in the gain which gives the A_{eff}.) Then A_{eff} is converted to h_{eff} by following Kraus [60]: $h_{eff} = 2.\sqrt{(50/Z_0)A_{eff}}$.

To account for viewing a linearly polarized signal with circularly polarized antennas, we divide the observed voltage by $\sqrt{2}$.

To emulate the 6σ cut we need to know the rms voltage due to thermal noise. In our 50 Ω oscilloscopes:

$$V_{rms} = \sqrt{k_{boltz} T_{sys} \Delta\nu 50.}$$

which accounts for voltage dividing between the source and the load, where $T_{sys} = 185, 170, 105$ K respectively pointing at the Moon center, half-limb and limb and $\Delta\nu$ is the bandwidth. We account for the effect of thermal fluctuations in the system on the observed voltage, since the signal and the fluctuations add via superposition. We choose a ΔV from a Gaussian with mean 0 and $\sigma = V_{rms}$ and add it to V.

If $V > 6V_{rms}$ in DSS14 RCP, $V > 3V_{rms}$ in DSS14 LCP, and $V > 4V_{rms}$ in DSS13 high and low, we call this a "hit" and add the event weight to a running sum we call *hits*. The efficiency η is therefore *hits* divided by the original number of neutrinos. We multiply this by the "black sphere" aperture, described in the next section, to obtain the effective aperture.

4.6.2 Normalization of the Monte Carlo

It is not immediately clear what the aperture of a perfect black sphere is, so we ran a series of "toy" Monte Carlos to examine this problem.

4.6.2.1 Aperture of a Flat Paddle

First we consider a flat surface bathed in an isotropic intensity (/cm^2/sr/s). To determine the rate of hits on the surface, integrate the intensity over the surface area and solid angle. The integral over solid angle ($d\Omega = d(\cos\theta)d\phi$) has an additional factor of $\cos\theta$ from the projection of the flux onto the surface. The integral over the surface area and solid angle "above" the surface is then

$$\int A_{proj} d\Omega = \int_0^1 A\cos\theta d(\cos\theta) \int_0^{2\pi} d\phi = \frac{1}{2}\int_0^1 A d(\cos^2\theta) \int_0^{2\pi} d\phi = A \times \pi \quad (4.7)$$

where A is the area of the flat surface. Multiply by 2 to obtain the solid angle from above and below. Therefore, the aperture for the flat surface in an isotropic flux is $A \times 2\pi$.

4.6.2.2 Aperture of a Sphere

There are two ways of looking at the aperture of a sphere. One way is to consider each area element on the sphere as a small patch that sees a solid angle π from Equation 4.7, since the flux is only coming from above for a "black sphere". The aperture is then $4\pi r^2 \times \pi$.

The other way is to consider that the flux from any given direction is perpendicular to some circular cross-section of the sphere. For a flux perpendicular to a surface, the solid angle is 4π and the surface area of a circular cross-section is πr^2, so the aperture of the sphere is $4\pi \times \pi r^2$, which is the same result as the first method.

4.6.2.3 Toy Monte Carlo

We wrote a toy Monte Carlo to compare the aperture of a sphere ($4\pi r^2 \times \pi$) to the aperture of a flat surface ($A \times 2\pi$). We choose a large flat circular disk of radius R ($A = \pi R^2$), with a small sphere of radius $r \ll R$ at the center of the disk. We choose a point in the large disk for the flux to intersect, and a direction for the flux which is flat is $\cos^2\theta$ and ϕ, according to Equation 4.7.

It is elementary to calculate whether or not any given line will intersect a sphere. If the line corresponding to the direction vector chosen above for the large disk intersects the small sphere, we count it as a "hit". The number of hits divided by the total number of events is the efficiency ϵ, and the effective apertures of the disk (efficiency = 100% by definition) and the sphere are related by

$$4\pi^2 r^2 = \epsilon \times 2\pi^2 R^2 \tag{4.8}$$

And in fact we do find that when we divide the RHS by the LHS from the toy MC, where r = 1 and R = 100, we obtain 1.0002 ± 0.0001.

4.6.2.4 Gray Sphere Monte Carlo

To test Equation 4.8, we modify the MC of a sphere in an isotropic flux to approximate a gray sphere. The density of the entire sphere is taken to be the density of water, and the cross section is such that only a small fraction of the incident flux will interact in the sphere. The direction vector of the flux is chosen as above, flat in $\cos^2\theta$ and ϕ. The aperture is given by

$$\text{Aperture}(\text{km}^2 - \text{sr}) = 4\pi^2 r^2 \times \frac{\text{interactions}}{\text{total number}} \tag{4.9}$$

We compare this to an alternate aperture which we get from the approximate km^3-sr, which is the volume of the sphere times 4π. To get km^2-sr, we divide

this km^3-sr by the interaction length (see Section 4.6.3). The alternate aperture is then

$$\text{km}^2\text{-sr}(alternate) = \frac{4}{3}\pi r^3 \times 4\pi \frac{\rho_{H_2O}\sigma}{1\text{amu}} \tag{4.10}$$

where $\frac{\rho_{H_2O}\sigma}{1\text{amu}}$ is $1/l_{int}$. Dividing Equation 4.9 (the MC result) by equation 4.10, where $l_{int} = 2 \times 10^4 r$, we get 1.0060 ± 0.0001. The discrepancy from 1 is due to the fact that the sphere is not perfectly light gray.

Therefore, we verify that the ultimate aperture A of the perfect black sphere bathed in an isotropic flux is $4\pi r_{moon}^2 \times \pi$.

4.6.3 Volumetric Aperture

The aperture in km^2-sr is given simply by $A \times \eta$ (see Section 4.6.2.1). However, for comparison with experiments that quote a volumetric aperture (such as IceCube), we wish to know the volumetric aperture in km^3-sr. The two quantities are related via the interaction length by the following argument.

The rate of interactions Γ is the intensity times the aperture. The aperture is the area A times the solid angle Ω, so $\Gamma = I_0 A\Omega$. However, in the thin target approximation, $I = I_0 \exp(-n\sigma d) \approx I_0(1 - n\sigma d) = I_0(1 - d/l_{int})$, where n is the number density in the target, σ is the cross section, d is the thickness, and l_{int} is the interaction length. Therefore

$$I_0 A\Omega = \left(I + \frac{I_0 d}{l_{int}}\right) A\Omega \tag{4.11}$$

$$\left(1 - \frac{I}{I_0}\right) A\Omega = \frac{(dA)\Omega}{l_{int}} \tag{4.12}$$

$$\frac{N}{N_0} A\Omega = \frac{V\Omega}{l_{int}} \tag{4.13}$$

or

$$\text{Aperture}(\text{km}^2 - \text{sr}) = \frac{\text{Volumetric Aperture}(\text{km}^3 - \text{sr})}{l_{int}} \tag{4.14}$$

4.6.4 GLUE Energy Threshold

We can determine the absolute minimum detectable energy by starting with a 6 σ signal in the antenna and then following it backward through the Monte Carlo, assuming the most favorable conditions at each step.

1. Begin with a 6 σ signal. A 6 σ signal V is

$$V = 6v_{noise} = 6\sqrt{50k_bT\Delta\nu} \tag{4.15}$$

where k_b is the Boltzmann constant, T is the system temperature (minimum is 100 K at the limb), and $\Delta\nu$ is the bandwidth (140 MHz; the 6σ signal is based on the channel with the highest bandwidth).

2. $V = \sqrt{2} \times V$ to account for polarization.

3. Now we convert to V/m/MHz (observed).

$$\text{V/m/MHz (observed)} = \frac{V}{0.5h_{eff}\Delta\nu(\text{MHz})} \tag{4.16}$$

where $h_{eff} = 2\sqrt{\frac{50a_{eff}}{Z_0}}$. The effective area $a_{eff} = G\lambda^2/4\pi$ where G is the gain, λ the wavelength. The gain is 63.34 dBi.

4. We assume maximum electric field response, so V/m/MHz = V/m/MHz (observed).

5. We account for the Fresnel coefficient and magnification. The highest value of $t = E_{vacuum}/E_{regolith}$ is .74 (see the Appendix), so

$$\text{V/m/MHz}|_{rego} = \frac{1}{0.74} \times \text{V/m/MHz}|_{vacuum} \tag{4.17}$$

6. We then convert to V/m/MHz at 1 m by multiplying by the distance to the moon:

$$\text{V/m/MHz at 1 m} = \text{V/m/MHz} \times d_{moon} \tag{4.18}$$

Table 4.19: MC Minimum Detectable Energy Calculation

step	quantity	value
1	V	1.865×10^{-5}
2	V	2.637×10^{-5}
3	V/m/MHz(observed)	9.14×10^{-9}
4	V/m/MHz	9.14×10^{-9}
5	$\text{V/m/MHz}\vert_{vacuum}$	1.23×10^{-8}
6	V/m/MHz at 1m	4.69
7	V/m/MHz at 1m	4.69
8	E_ν	6.6×10^{19} eV

where $d_{moon} = 3.8 \times 10^8$ m.

7. We assume the viewing angle is the Cherenkov angle, so there is no correction from the width of the Cherenkov cone.

8. Finally, convert to a minimum neutrino energy:

$$E_\nu = \frac{10^{12}(1 + (\frac{\nu}{\nu_0})^{1.44})(\text{V/m/MHz at 1 m})}{1.5 \times 10^{-7}(\frac{\nu}{\nu_0})} \tag{4.19}$$

where $\frac{\nu}{\nu_0} = 2.25\text{GHz}/2.7\text{GHz} = 0.833$.

Table 4.19 shows the values of these quantities at each step. The final result is a minimum energy of 6.6×10^{19} eV. However, this minimum energy assumes the most optimistic geometry. The effective energy threshold, at which the MC generates a statistically significant number of events, is 3×10^{20} eV.

Table 4.20: MC Result Comparison

log energy(eV)	log aperture (km^3-sr) JPL/UH MC	log aperture(km^3-sr) UCLA MC
20.5	1.75	0.987
21	2.75	2.19
21.5	3.13	2.84
22	3.55	3.35
23	3.97	4.01

4.6.5 Comparison to Other Monte Carlo Results

Another Monte Carlo, based on ray-tracing the full Cherenkov cone out of the moon, was developed at JPL and the University of Hawaii at Manoa. Table 4.20 compares the results of the JPL/UH MC to the UCLA MC.

These numbers agree to within a factor of 2 above 10^{21} eV.

4.6.6 Pointing Configuration Comparison

Figure 4.23 shows the apertures for all three pointing configurations that we used: limb focused, U/2 (half-limb) defocused, and center focused. The aperture is highest at the limb, although at high energies the apertures for all three choices converge.

4.6.7 Scaling with Various Parameters

The aperture increases with bandwidth, but not very steeply. Figure 4.24 shows scaling with bandwidth for two energies. The change with bandwidth is

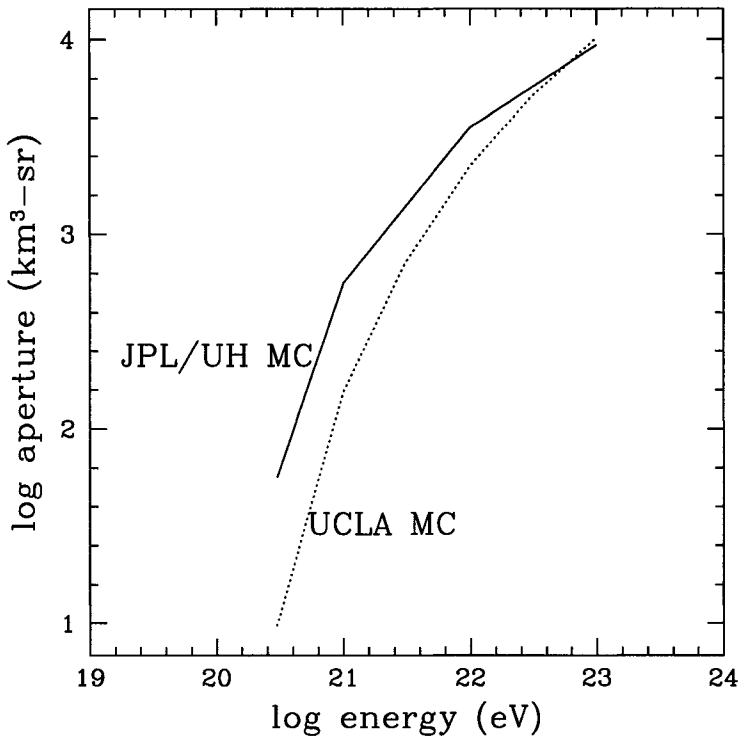

Figure 4.22: Apertures for UCLA (dotted) and JPL/UH (solid) Monte Carlos.

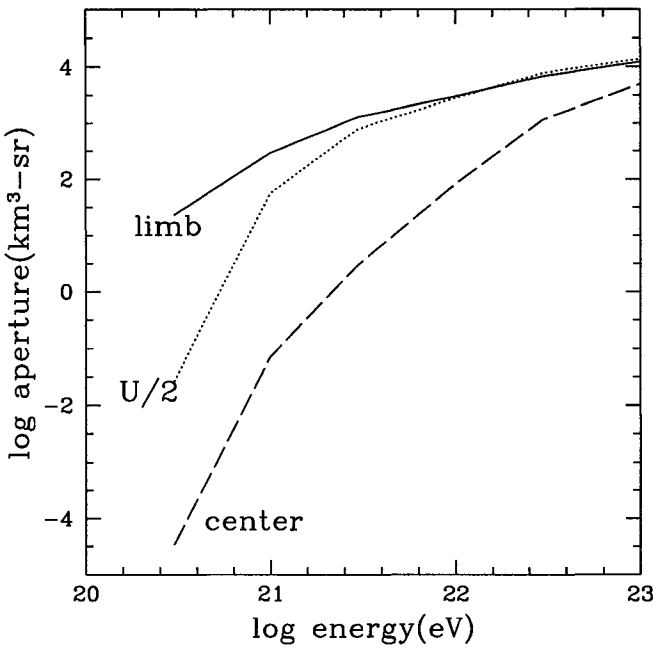

Figure 4.23: Apertures for the three pointing choices: limb focused, half-limb(U/2) defocused, and center defocused.

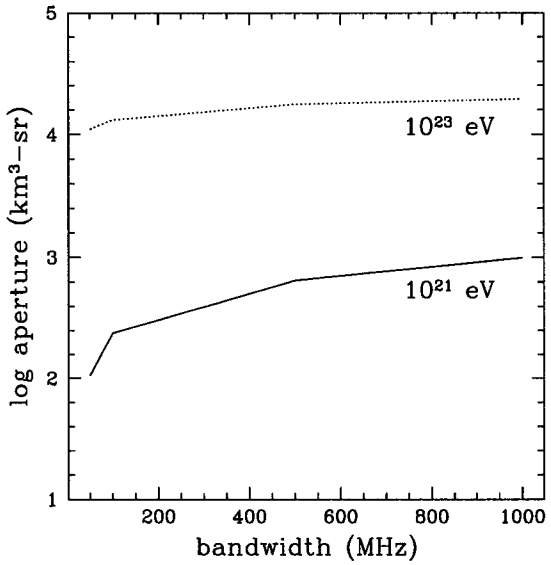

Figure 4.24: Aperture vs. bandwidth for two energies. Pointing mode and frequency are the nominal values for GLUE.

steeper at low energies, indicating that bandwidth is more important for improving aperture at low energies than at high energies. Figure 4.25 shows the scaling with frequency. The aperture is higher at lower frequencies, where the attenuation length is longer.

4.6.8 Inelasticity and Flavor Fraction At Threshold

Figure 4.26 a shows the fraction of each neutrino flavor that contributes to the sum of weighted hits in the MC as a function of energy. At the lowest energy (3.16×10^{20} eV), the fraction of ν_e events is much higher than the fraction of ν_τ and ν_μ events. At the highest energy (10^{23} eV) each flavor contributes equally.

Figure 4.26 b shows the weighted average of the inelasticity parameter y at each energy, for ν_e and non-ν_e events. The inelasticity falls with increasing energy

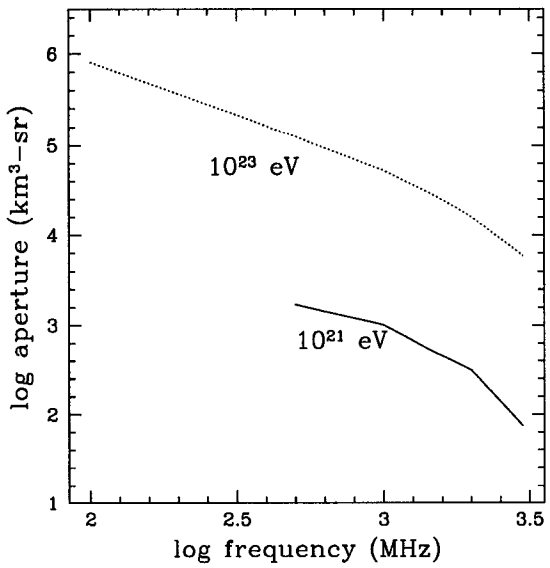

Figure 4.25: Aperture vs. frequency for two energies. Pointing mode and bandwidth are the nominal values for GLUE.

for both types of events, and the average inelasticity is higher for non-ν_e than for ν_e events.

4.6.9 Checks on Solid Angle and Volume

We want to understand our effective solid angle and volume based on a factorization of V and $d\Omega$. This is not a well-defined problem, so there is no unique factorization to use. Also, this method may be incorrect because the product of integrals is not necessarily equal to the integral of the product, but it does give us a basis for comparison.

We divide the two-dimensional space of the neutrino's direction angles, $\cos\theta_\nu$ and ϕ_ν into a grid (the numbers quoted here use 30 bins each; this number can vary). We define the solid angle by an iterative process. We identify the bin with

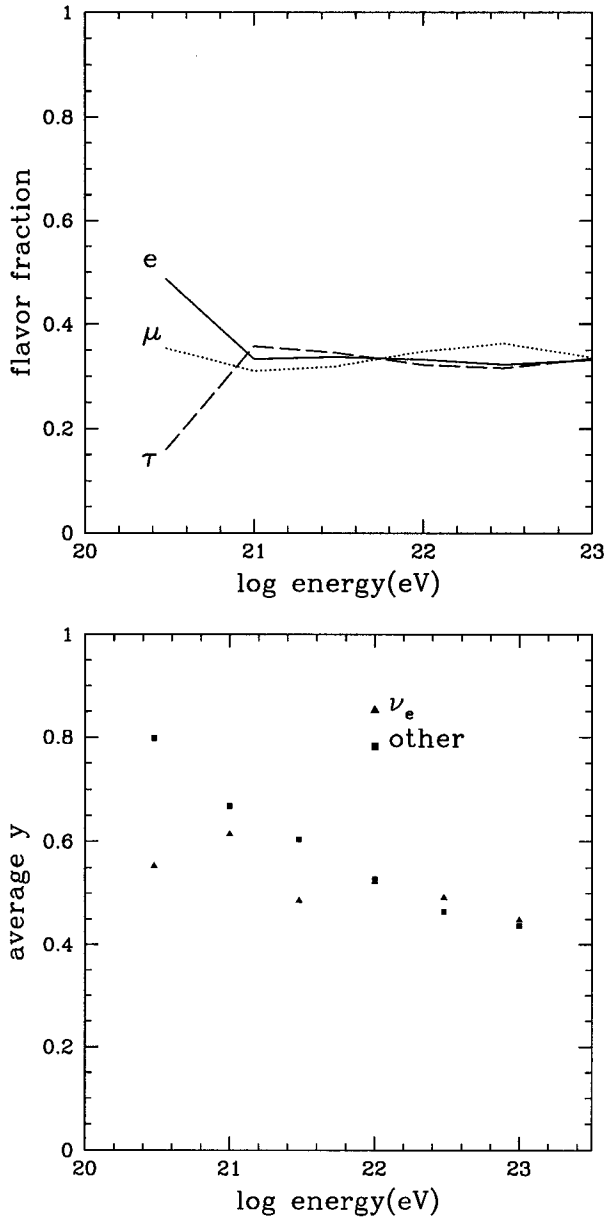

Figure 4.26: Top: Weighted flavor fraction vs. energy for ν_e (solid), ν_μ (dotted) and ν_τ (dashed). Bottom: weighted average inelasticity vs. energy for ν_e events (squares) and non-ν_e events (triangles).

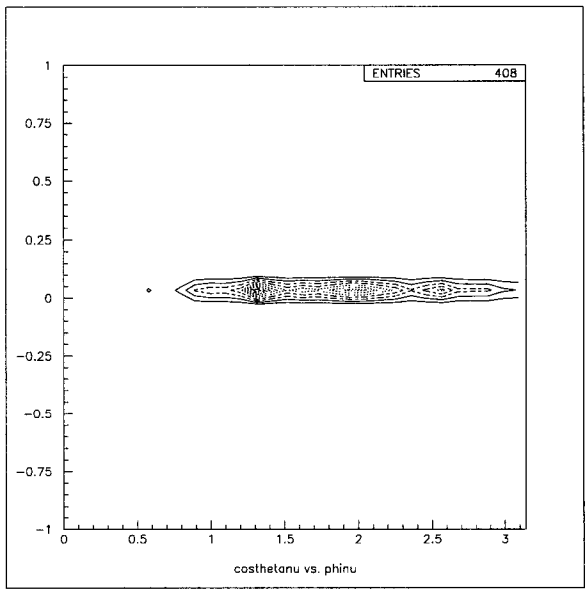

Figure 4.27: Contour plot of the weights in $\cos(\theta_\nu)$ vs. ϕ_ν grid, 10^{22} eV neutrino. The angles are in the reference frame where the normal vector at the neutrino's entrance point is the z-axis, so the concentration at $\cos(\theta) = 0$ indicates skimming events.

the highest weight and add it to a running sum. This process is continued for the next largest bin, etc. until the running sum of weights equals 90% of the total sum of weights in all bins in the grid. The fraction of bins which contributes to this sum, times 4π, is defined as the effective solid angle. Figure 4.27 shows a contour plot of weights in this grid for a 10^{22} eV neutrino.

Similarly, we defined an effective volume for each energy, using a 3-dimensional grid in $\cos\theta$, ϕ and depth, where θ and ϕ are the position angles of the neutrino's entrance to the moon's surface. Figure 4.28 shows scatter plots of the three combinations of $\cos\theta$, ϕ and depth for a 10^{22} eV neutrino.

In order to estimate km^3-sr, we multiply the solid angle for a small patch (about 1 square degree) by the effective volume. At 10^{22} eV, the solid angle for

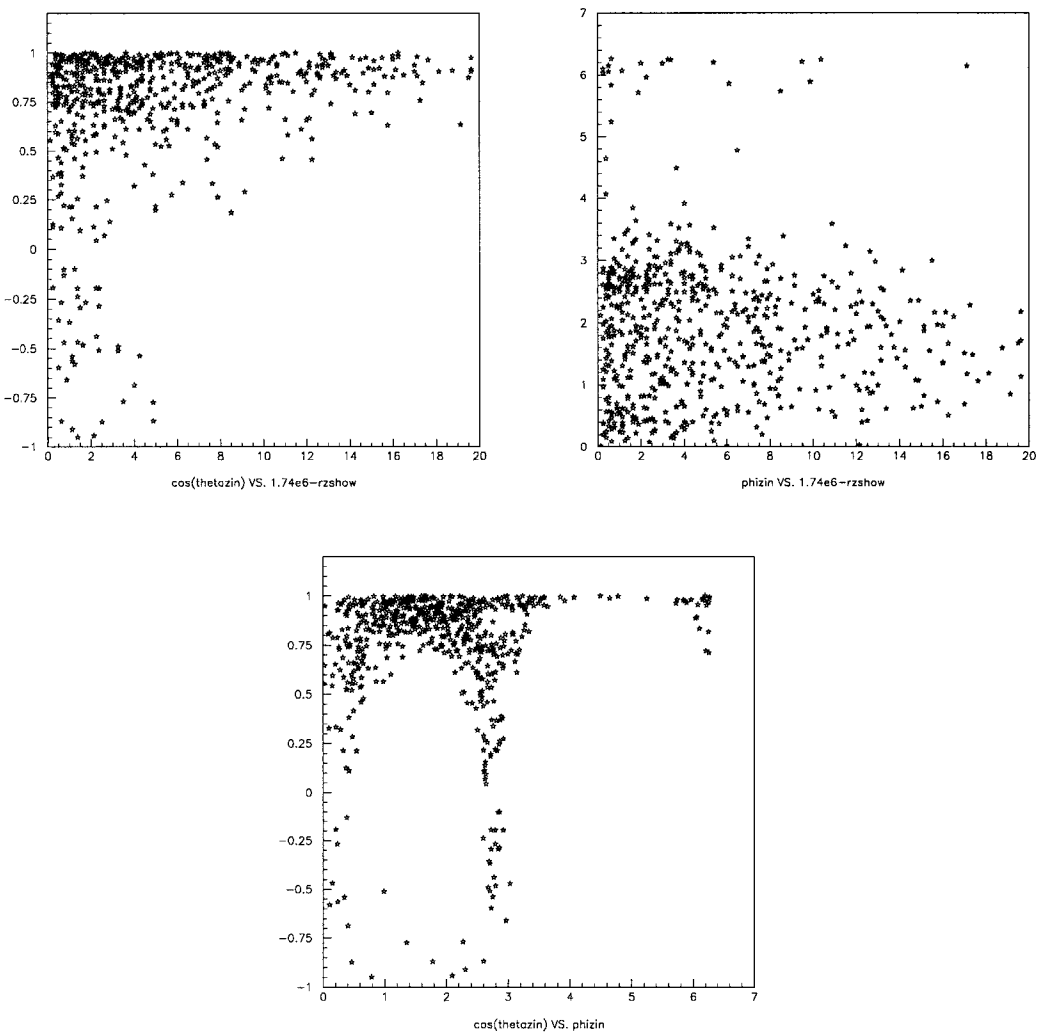

Figure 4.28: Clockwise from top left: cosθ vs. shower depth, ϕ vs. shower depth, and cosθ vs. ϕ for a 10^{22} eV neutrino. These are only events which count as hits. The concentration at phi= 0 and π and cosθ = 1 implies concentration at the limb and the upper part of the moon, which we expect from a telescope in the Northern hemisphere looking above the center of the moon.

a small patch at the moon upper limb is .009 sr. The effective volume is about 200,000 km^3. The product is then 1800 km^3-sr. The full MC at this energy gives 2700 km^3-sr, so there is order-of-magnitude agreement.

4.6.10 Conclusions

The agreement between the two MCs is better above 10^{21} eV, although there is still disagreement at the threshold energies. At threshold, small differences in the calculation appear as large differences in the aperture. The best pointing configuration is at the limb.

4.7 Upper Limits from GLUE

The number of events that a given neutrino specific intensity $I_E^i(E)$ produces in a given experiment is given by

$$N = [\sum_{i=1}^{3} \int_{E_1}^{E_2} \alpha^i(E) I_E^i(E) dE] \Delta t, \tag{4.20}$$

where i is the sum is over the three neutrino species and α is the aperture (in this case the volumetric aperture divided by the interaction length, or effective area-solid angle). Note that the specific intensity has units of 1/(energy*time*area*solid angle).

The topological defect model from Yoshida [15], which is the most optimistic, predicts 0.3 neutrinos in 123 hours of livetime at GLUE. Therefore the livetime would have to be increased by a factor of 3 in order for the model to predict 1 neutrino. However, this is impractical to achieve given that Goldstone's primary responsibility for spacecraft telecommunications limits the amount of time available for the GLUE experiment.

4.8 GLUE Expansion Study (CELENE)

I undertook to study the possibility of expanding the Goldstone experiment to a facility with more telescopes and more dedicated time for astronomy. In my study I used the parameters of the Australia Telescope Compact Array (6 antennas, 22 m). The tentative name of the expanded experiment is the Čerenkov Lunar Emission by Neutrinos Experiment (CELENE).

For CELENE, we assume that we have six 22-meter antennas, each giving LCP and RCP signals. These 12 channels are each assumed to have 530 MHz bandwidth, and can be further subdivided into high and low frequency channels with 265 MHz bandwidth each. The frequency is assumed to be 1.5 GHz. The antenna temperatures are taken to be 100 K, pointing at the limb. The amplitude cut is taken to be 2 sigma. The MC is run for 123 hours, the same livetime as we have at GLUE.

Figure 4.29 shows the aperture of GLUE compared to the aperture of CELENE for the same livetime. There is an improvement of almost an order of magnitude for all energies, but no serious improvement in the energy threshold.

The Yoshida topological defects model predicts 3 neutrinos in 123 hours of livetime with the CELENE configuration. No other model predicts even 1 neutrino.

A proposal for three nights at the Array was accepted for the fall 2003 observing period. However, at this time most of the GLUE collaborators were in Antarctica for the ANITA-lite experiment [61]. In addition to this, we discovered that it was difficult to get the full analog bandwidth from all six telescopes to one location in order to form our trigger. Usually, the bandwidth is split into narrow channels and digitized before being sent to the control room. Given the

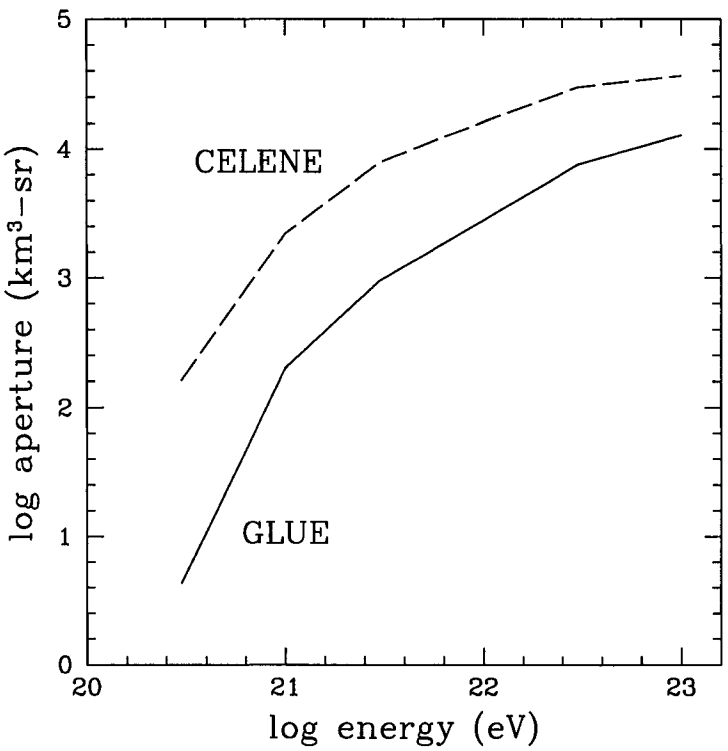

Figure 4.29: Apertures for GLUE (solid) and CELENE (dashed).

complication and the lack of personnel available at the time, it was decided not to proceed with CELENE. ANITA is a better investment of time and energy, since it improves on CELENE's energy threshold and aperture (see Section 6).

4.9 Conclusions from Lunar Neutrino Experiment

The Goldstone experiment demonstrates that the radio technique is robust, with no false positives, and gave us valuable experience with radio hardware and the techniques for radio detection Monte Carlos. However, the experiment itself has too high of an energy threshold to detect any but exotic neutrino flux models. In order to study more likely models such as the GZK flux prediction, we need a detector with a lower energy threshold. The Goldstone threshold is dominated by the distance to the moon, so in general a lower energy threshold requires a detector that is closer to the medium of detection.

CHAPTER 5

Conceptual and Design Studies for a Salt Neutrino Detector

5.1 Introduction

Askar'yan [24] mentioned rock salt as another potential medium of detection. Pure rock salt has a very long attenuation length in the radio. Chiba *et al.* [58] collected a variety of rock salt samples from mines and measured their attenuation properties. They found that the absorption length at 1 GHz is between 40 and 400 m. However they stress that *in situ* measurements at a given site are necessary to determine if it can be used for a salt neutrino detector (SND). It is impractical to purify enough salt to form a km^3 scale detector, so we must determine the effects of impurities at naturally occurring sites.

5.2 Salt Formation Measurements

In 2000 and 2001, we made two *in situ* measurements of the radio attenuation properties of salt formations.

5.2.1 WIPP

Our first candidate site was the Waste Isolation Pilot Plant (WIPP) in Carlsbad, New Mexico [59]. This is a 2150 ft. deep facility in a 2000-foot-thick salt formation which the Department of Energy is using to store transuranic waste from nuclear weapons research facilities. WIPP also has support for scientific research.

We used pre-existing boreholes in the ceiling of Room 6 in the facility. We placed RF-balanced copper dipoles in the boreholes by attaching them to rigid heliax cable. The antennas were raised to depths ranging from 6 ft to 18 ft into the hole. We mixed a pulse from a Marconi pulse generator (varying from 90 to 500 MHz) with a 50 ns square signal and sent the resulting pulse train from one dipole to the other. We had three boreholes in the room and a fourth in a connecting corridor. Figure 5.1 shows the relative positions of the boreholes. The distance between a pair of holes ranged from 72 to 147 ft. The receiving dipole remained in the same borehole throughout the run while the transmitting dipole was placed in the other three holes. The receiving hole is denoted hole E. The transmitting holes are F (d = 75 ft), G (d = 147 ft) and H (d = 104 ft), where d is the distance from the hole to hole E. Figure 5.2 shows the transmitted and received pulses at WIPP. Clear signals were seen in the receiving antenna only up to 200 MHz. Cross-correlation later showed a clear received signal up to 400 MHz, but data was not taken above 300 MHz in all three holes.

We also made attempts to measure attenuation through one of the supporting pillars and also in horizontal boreholes in one of the walls, but we did not see any clear signals.

The critical parameter is the field attenuation length, a, which is the length over which the intensity of the electric field falls to $1/e$ of its original value.

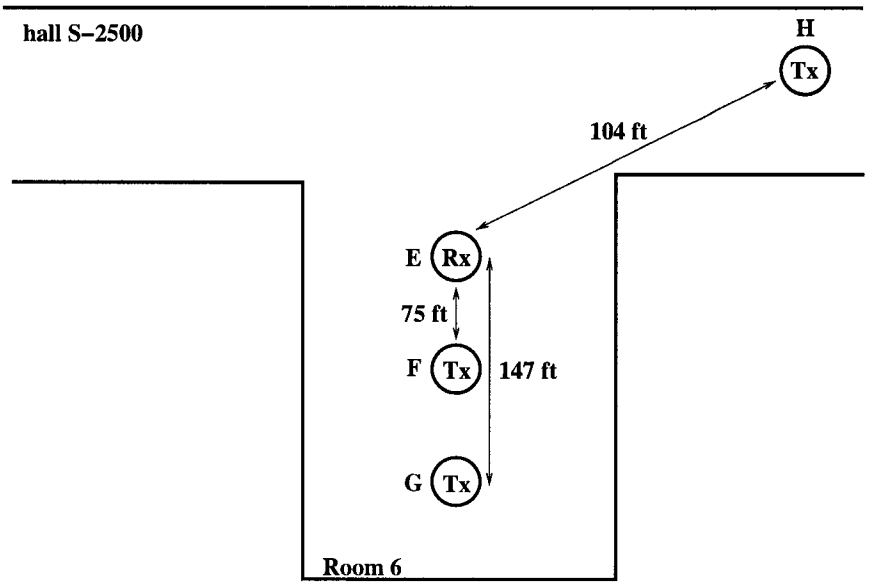

Figure 5.1: Plan diagram of relative positions of ceiling boreholes used at WIPP. The receiving dipole remained in hole E; the transmitting dipoles were in holes F,G and H.

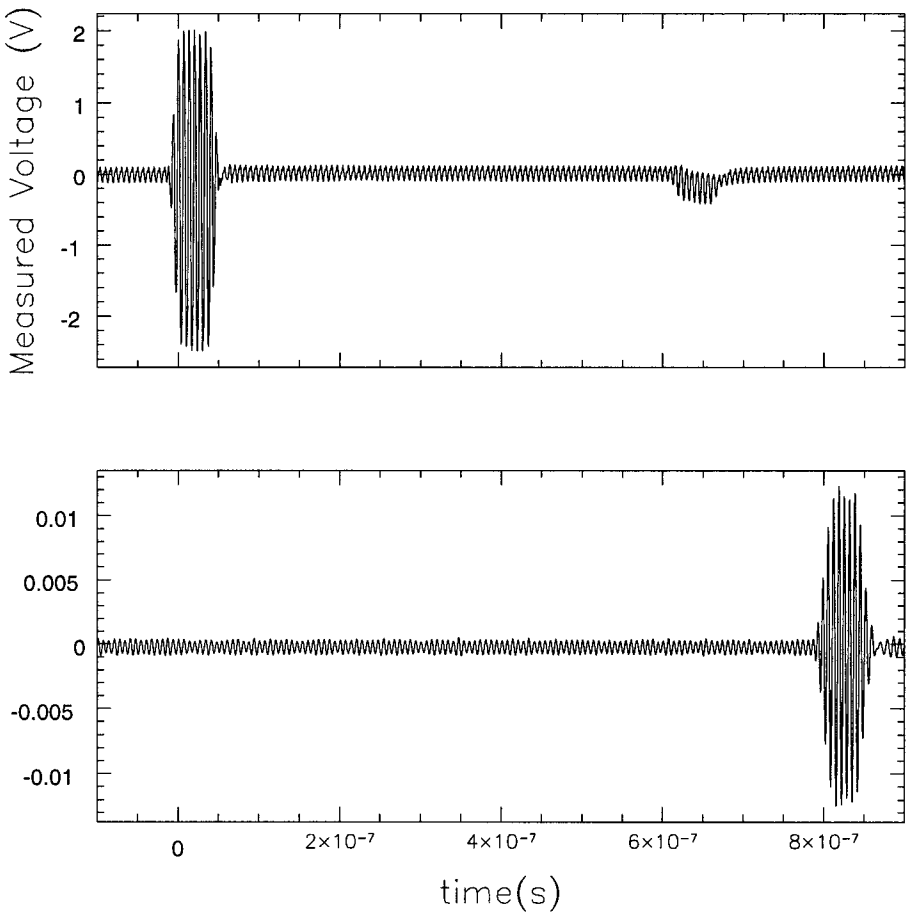

Figure 5.2: Transmitted (top) and received (bottom) pulses at WIPP.

The attenuation length is calculated by comparing the measurements from two different transmitting holes. Let V_1 be the received voltage transmitted from hole 1, and V_2 be the received voltage transmitted from hole 2. Let d_1 be the distance from the receiving hole to hole 1, and d_2 be the distance from the receiving hole to hole 2. Then the attenuation length a is given by

$$\frac{V_1}{V_2}\frac{d_1}{d_2} = \exp\left[-\frac{(d_1 - d_2)}{a}\right] \tag{5.1}$$

Another common parameter for describing the attenuation properties of a material is the loss tangent δ, given by

$$\tan\delta = \frac{\lambda}{2\pi n a} \tag{5.2}$$

where n is the index of refraction, which we measured to be 2.82±0.06 at 150 MHz. Note that the index of refraction is 2.4 in pure salt [58].

Figure 5.3 shows the measured attenuation length versus frequency for the three pairs of transmitting holes. The error bars are the largest in the H and G pair, because their distance to E is very similar and therefore there is not enough length difference to make a good attenuation measurement. For the more reliable pairs, the attenuation length is shown to be less than 10 m. A map of the strata seen in core samples of the salt formation shows clay impurities in the material as well as brine which we observed. This accounts for the low values of the measured attenuation length. The attenuation length is far too small to make the WIPP formation practical for a cubic kilometer detector.

5.2.2 Hockley

Our second candidate site is a diapir, the Hockley salt dome. It is actively mined by the United Salt Company at a depth of 460 m. The top of the dome

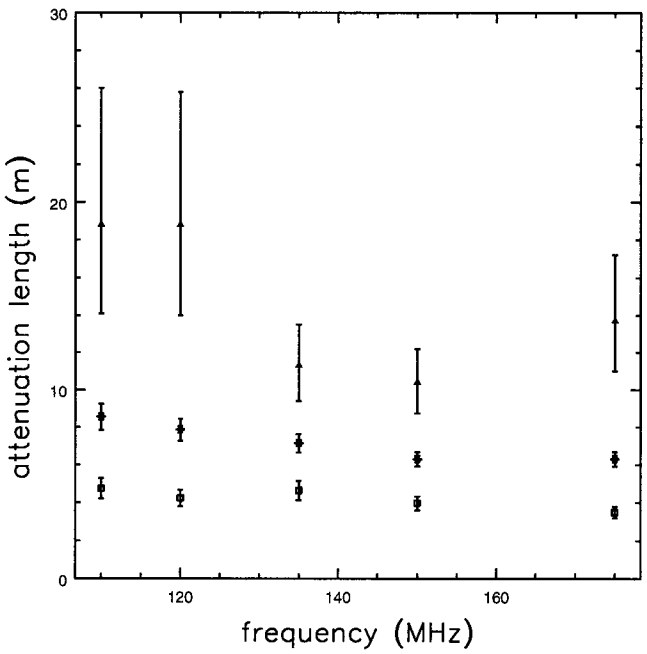

Figure 5.3: Attenuation length vs. frequency at WIPP - triangles: holes H and G, squares: holes H and F, stars: holes G and F.

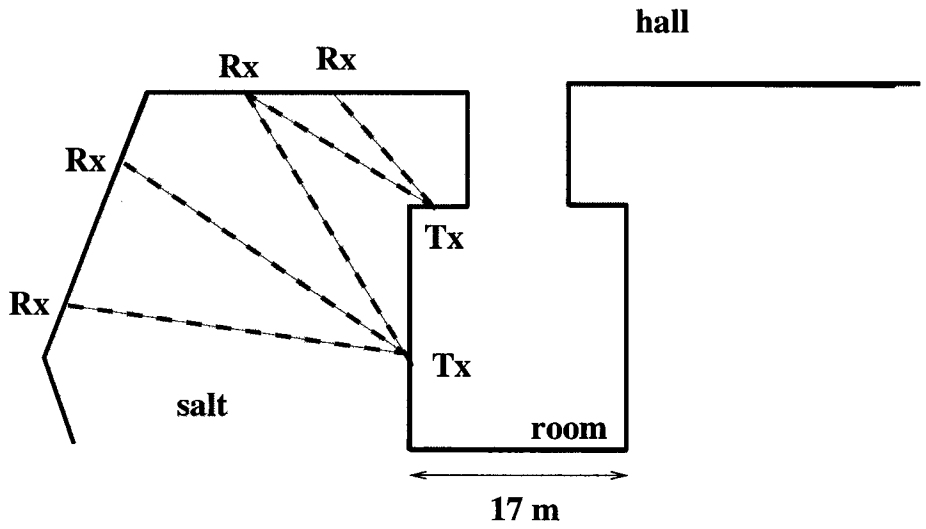

Figure 5.4: Transmitting and receiving positions at Hockley for June 27, 2001.

is 300 m below the local surface and the dome is an inverted teardrop structure which extends as much as 10 km down. At mine level the horizontal cross section of the structure is approximately 3.6 by 2.9 km.

We made our measurements at Hockley from June 25 to June 27, 2001. Most of the analysis is from June 27, which we denote "day 3". We did not have boreholes at Hockley, so we placed our antennas in contact with the salt surface along the walls to transmit signals through the salt, as shown in Figure 5.4. We used a half-wave dipole tuned to peak at 150 MHz, which also worked at the full-wave resonance at 300 MHz. We also used a directional UHF bowtie antenna array at 750 MHz. We transmitted signals through "pillars" in the mine which were from 100 to 300 feet wide. The signals were the same kind used at WIPP as shown in Figure 5.2.

The first-order analysis is to compare the expected received power in the dipole to the measured received power. The Friis formula for the relationship

between transmitted (T_x) and received (R_x) power in an antenna is given by

$$\frac{P_{R_x}}{P_{T_x}} = \frac{A_{T_x} A_{R_x}}{\lambda^2 R^2} \tag{5.3}$$

where A is the effective area of the transmitting or receiving antenna, λ is the wavelength and R is the distance between the two antennas. Recasting this equation in terms of the voltage measured:

$$\frac{V_{R_x}}{V_{T_x}} = \sqrt{\frac{A_{T_x} A_{R_x}}{\lambda^2 R^2}} \tag{5.4}$$

Noting that $A_{T_x} = A_{R_x}$ and multiplying both sides by R, we have

$$\frac{V_{R_x}}{V_{T_x}} R = \frac{A}{\lambda} \tag{5.5}$$

From Kraus [60], the effective area of a half-wave dipole is $0.13\lambda^2$. For a full-wave dipole in the thin dipole approximation, the effective area is $0.048\lambda^2$. The dipoles used at Hockley are half-wave at 150 MHz and full wave at 300 MHz, so at 150 MHz,

$$\frac{V_{R_x}}{V_{T_x}} R = 0.13\lambda \tag{5.6}$$

while at 300 MHz,

$$\frac{V_{R_x}}{V_{T_x}} R = 0.048\lambda \tag{5.7}$$

I define $\xi_{150} = \frac{V_{R_x}}{V_{T_x}} R$ at 150 MHz, and ξ_{300} is the same at 300 MHz. Figure 5.5 show the ξ_{150} and ξ_{300} values plotted versus distance for the data from day 3, which is divided into six sets based on the relative positions of the transmitting and receiving antennas. The solid line in the figures shows the absolute value for ξ_{150} and ξ_{300} given by the Friis formula. The data points are corrected for the attenuation in the heliax cables, for the amplifiers, and for reflections. At 150 MHz, about 1/3 of the power in the transmitting antenna is reflected back. The reflections for the 300 MHz data were not seen because the record length was

accidentally set too short in those data sets for which we recorded the transmitting antenna data at 300 MHz (sometimes this data was not saved in the interest of time). So the same reflection power is assumed for 300 MHz. Note that the Friis formula assumes a dipole pattern, which wasn't quite right at Hockley because the antenna pattern was half in salt and half in air. The data points are consistent, within an order of magnitude, with the value given by the Friis formula, which assumes no attenuation. Therefore the data is consistent with a very long attenuation length, since little or no attenuation is seen over 40 meters.

The attenuation length changes with frequency, so the next step is to use ξ_{150} to normalize ξ_{300}. The ratio of the received to transmitted voltage in an antenna should fall off as

$$V_{Rx} \propto V_{Tx} \exp\left[-\frac{d}{a}\right] \tag{5.8}$$

where d is the distance between the transmitting and receiving antennas and a is the field attenuation length. The loss tangent δ is given by Equation 5.2. If the loss tangent is approximately flat with respect to frequency, which we expect from previous measurements at WIPP, then the field attenuation length is proportional to the wavelength. That is, the attenuation length at 300 MHz is half of the attenuation length at 150 MHz. Then

$$\frac{\xi_{300}}{\xi_{150}} = \exp\left[-\frac{d}{a_{150}}\right] \tag{5.9}$$

If the measured distances d are greater than λ_{150} then we would expect the ratio on the left hand side of Equation 5.9 to fall exponentially over that range of distances.

Figure 5.6 shows the ratio ξ_{300}/ξ_{150} as a function of distance. We obtain the four points by taking all of the points from day 3 in a certain distance bin and taking the average of the voltage ratio. The error bars are given by the root-mean-square of the voltage ratio divided by $\sqrt{N-1}$, where N is the number of

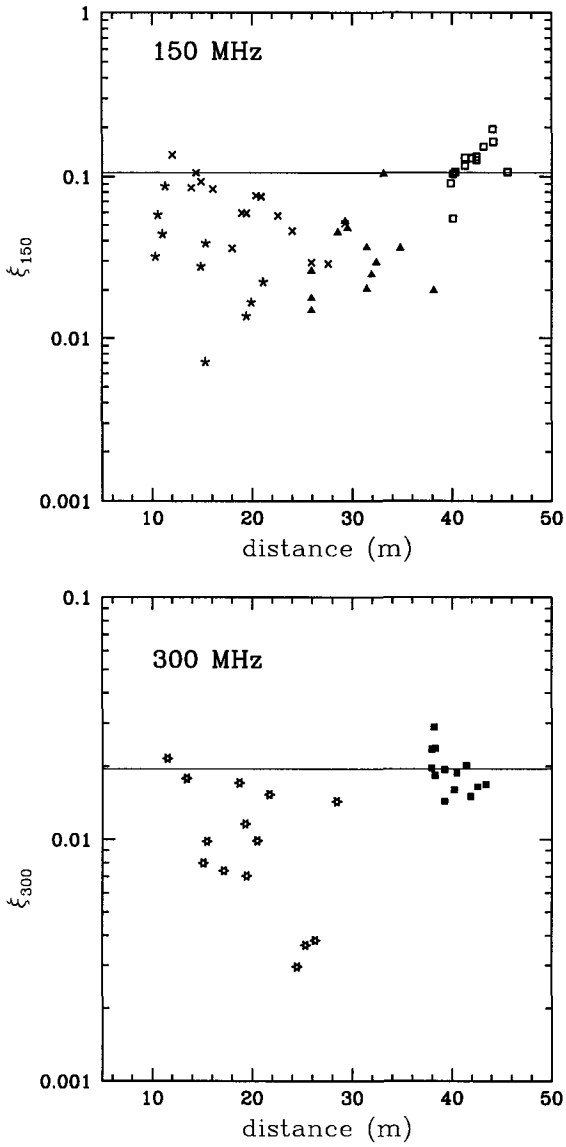

Figure 5.5: Top: Friis formula measurement at Hockley, 150 MHz, from day 3. Triangles are data set 1, squares are data set 2, stars are set 3, and crosses are set 4. Bottom: Friis formula measurement at Hockley, 300 MHz from day 3. Stars are set 5, squares are set 6.

data points. The first point is normalized to be equal to 1. The points are fairly flat as a function of distance, not falling exponentially. This indicates that the attenuation length is longer than the distances in this range. A fit to the data is extremely uncertain, but indicates an attenuation length of at least 300 m.

We also measured the noise environment in the mine, which we expect to be thermal, since the overburden of rock should eliminate any RFI from the surface. We measured the noise environment at the Hockley site using the same short dipole used at 150 MHz. We calculated that the system temperature of our apparatus was 770 K including front-end amplifier noise (263 K) , cables (1.2 dB at 310 K), and 310 K salt filling the antenna aperture. We observed no departure from uniform power in the power spectrum. We could not observe any difference between observing the salt through an antenna versus a 50 Ω load at the front-end amplifier input. We could have detected excess power from the salt (above its blackbody temperature) of order 100 K if it were present. Hence we conclude the noise environment may be characterized as fluctuations of a 310 K blackbody spectrum. On rare occasions we could see clear RFI due to the use of walkie-talkies by local mining crews. Such events in a salt detector would be easily removed by offline analysis but could cause a high trigger rate. To keep the trigger rate low, a salt detector in the mine might require tuned notch filters for the communication frequencies in use at the facility. Figure 5.7 shows the thermal noise spectrum.

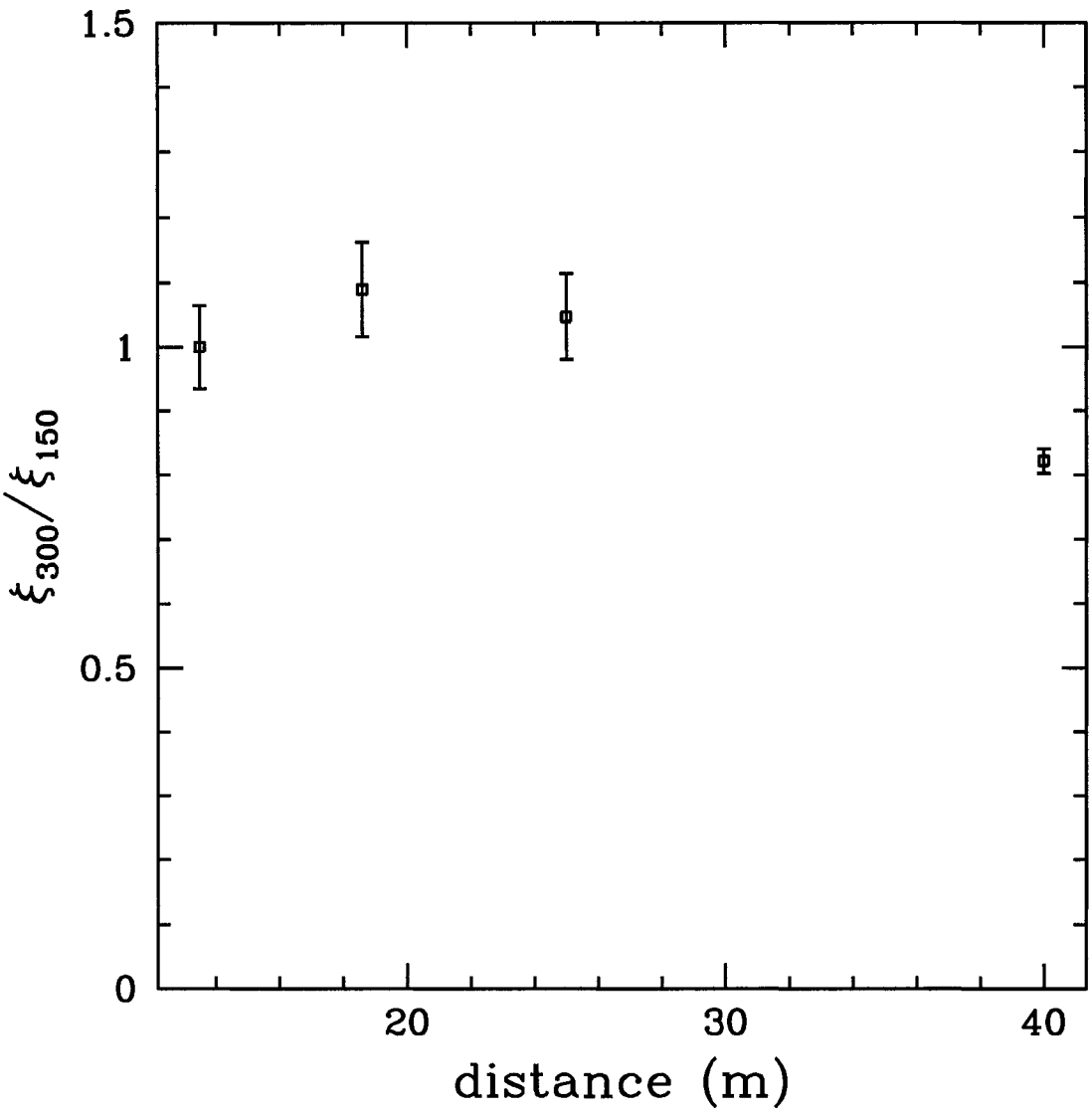

Figure 5.6: The ratio of peak-to-peak voltages at Hockley for 300 and 150 MHz vs. distance.

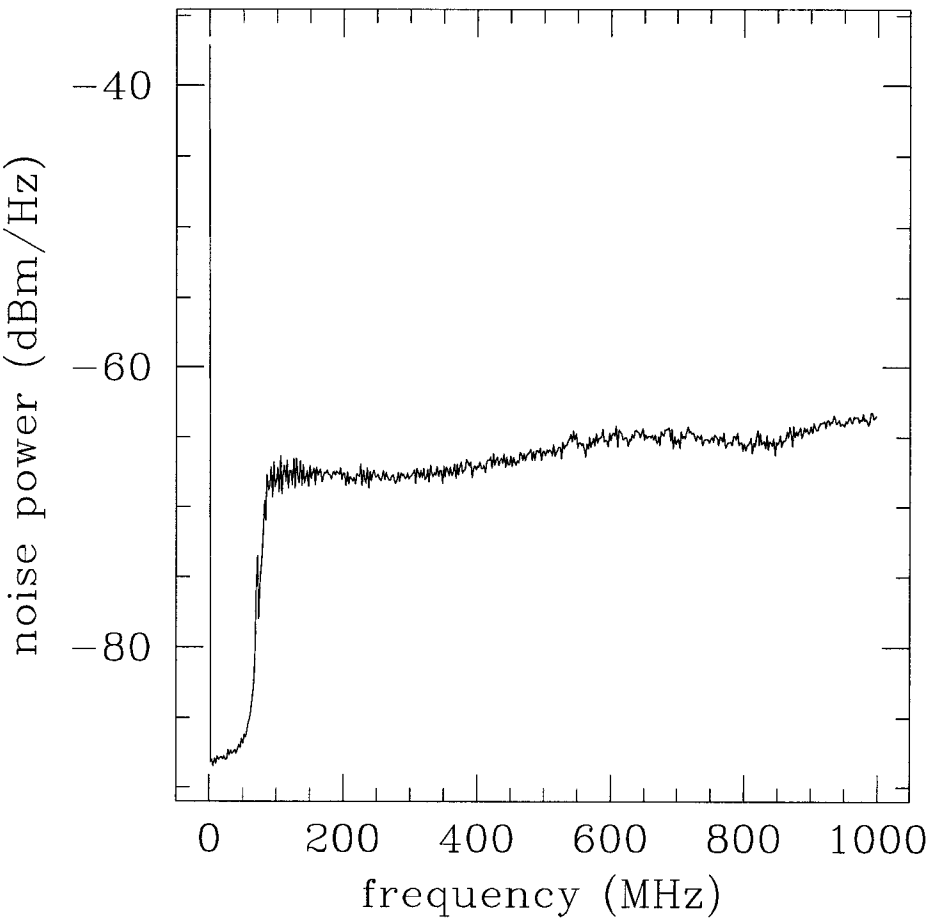

Figure 5.7: Thermal noise spectrum at Hockley.

5.3 Design Studies for a Salt Dome Shower Array (SALSA)

In 2003 we developed a Monte Carlo study of the aperture of an array of antennas in a salt formation, which is based on the GLUE Monte Carlo. In this section I discuss the Monte Carlo, the calculated aperture, the expected trigger rates from thermal noise and the expected numbers of neutrinos from various models.

5.3.1 Salt Detector Monte Carlo

The Monte Carlo for a salt neutrino detector is somewhat simpler than for GLUE, since we do not need to account for refraction or the Fresnel coefficient. We model the salt formation as a cube of salt 8 km to a side with a concentric cube of 1000 antennas 2 km to a side. The salt formation begins 500 m below the Earth's surface.

First we choose a random neutrino interaction point within the volume in Cartesian coordinates. The interaction point is flat in x, y, and z. Since the linear dimensions of the detector are much smaller than the interaction length of neutrinos in this energy regime, we assume that the neutrino is equally likely to interact anywhere in the detector. The neutrino direction is chosen flat in $\cos\theta$ and flat in ϕ. Having chosen the neutrino's interaction point and trajectory, we proceed to determine its entrance point on the Earth's surface, and its entrance point in the salt formation.

We consider the effects of the path that the neutrino takes through the earth. The earth is modeled with a very simple three-layer density profile:

$$\text{crust: } \rho = 2900\text{kg/m}^3, 6330\text{km} < r < 6370\text{km}$$

$$\text{mantle: } \bar{\rho} = 4650\text{kg/m}^3, 3464\text{km} < r < 6330\text{km}$$

$$\text{core: } \rho = 14000\text{kg/m}^3, 0\text{km} < r < 3464\text{km}$$

It will be seen that a more sophisticated density profile is probably not necessary, since the most significant events come from chords through the crust.

Each individual chord is given a column density $c(\text{kg/m}^2) = c\rho$, where c is the chord length in meters from the neutrino's entrance point in the Earth to its interaction point and ρ is the average density over that chord. First, we determine whether the neutrino will in fact interact in this chord, given that the interaction lengths at these energies are of the same order of magnitude as the radius of the Earth and therefore interaction cannot be assumed. We assign a weight to each event based on the length of its chord in terms of the interaction length:

$$weight1 = 1 - \exp(-c/\tau)$$

where c is the length of the chord in kg/m^2 and τ is the interaction length.

If the neutrino interacts in this chord, then we assign the interaction point a weight. Neutrinos which interact near the beginning of their chords (downgoing) have a higher weight than those which interact near the ends of their chords (upcoming). Since we force the neutrino to interact inside the salt formation, the weight is

$$weight2 = \frac{\exp(s/\tau) - 1}{\exp(c/\tau) - 1}$$

where s is the length in kg/m^2 through the salt, and c is the length in kg/m^2 of the total chord from the neutrino's entrance in the Earth to its interaction point.

Now we loop over all the antennas in the cubic volume to find their distance from the interaction point. We calculate the viewing angle θ_V of the shower,

which is the angle between the direction from antenna to interaction point and the neutrino direction. The electric field of the shower is calculated using Jaime Alvarez's parameterization (private communication):

$$E(\mathrm{V/m/MHz@1m}) = 8.49 \times 10^{-11} \frac{E_\nu}{10^{12}} \frac{\nu}{1\mathrm{MHz}} \frac{1}{1+(\frac{\nu}{\nu_0})^{1.5}} \tag{5.10}$$

where $\nu_0 = 1300$ MHz. We convert V/m/MHz@1m to V/m/MHz by dividing by the distance to the antenna.

The LPM effect and interaction type, and the corresponding shower width $\Delta\theta$, are calculated as in the GLUE Monte Carlo in Section 4.6. Given that we know the Cherenkov angle θ_C and viewing angle θ_V from above, we use the parameterization of the cone thickness (modeled by Alvarez-Muniz *et al.* [51] as a Gaussian) to calculate the electric field seen:

$$\mathrm{V/m/MHz} \rightarrow \mathrm{V/m/MHz} \times \exp(-\ln(2)(\frac{\theta_C - \theta_V}{\Delta\theta})^2)$$

We then scale by the attenuation factor in salt, given that we know the distance from antenna to interaction point:

$$\mathrm{V/m/MHz} = \mathrm{V/m/MHz} \times \exp(-\mathrm{distance/attenlength}) \tag{5.11}$$

where the attenuation length in salt, taken from the Hockley measurement, is 300 m $\times(300$ MHz$/\nu)$.

Now we calculate the antenna response. We assume the antennas are circularly polarized. The effective height of the antenna is

$$h_{eff} = \lambda/\pi$$

We assume the bandwidth $\Delta\nu$ is 50% of the frequency. The antenna voltage is then

$$V = \mathrm{V/m/MHz} \frac{1}{2} h_{eff} \frac{\Delta\nu}{10^6} \frac{\cos(\frac{\pi}{2}\cos\theta)}{\sin\theta}$$

where θ is the polar angle of the shower with respect to the vertically oriented antenna.

We then calculate the 1 σ noise:

$$V_{noise} = \sqrt{Rk_bT\Delta\nu}$$

where $R = 50\Omega$. We add a Gaussian fluctuation with $\sigma = V_{noise}$ to each antenna voltage. Any event whose voltage V is then above $6 \times V_{noise}$ in four or more antennas counts as a "hit".

To get the effective aperture of the detector, we multiply the physical aperture (volume$\times 4\pi$) by the ratio $weight/N_{int}$ where $weight$ is the sum of $weight1 * weight2$ for all "hits" and N_{int} is the number of neutrinos that would interact in the salt if the rest of the Earth was not present. This ratio is determined separately for ν_e, ν_μ and ν_τ.

5.3.1.1 MC Results

Figure 5.8 shows the aperture for all three neutrino flavors. At the lowest energies, electron neutrinos dominate the sensitivity, but the sensitivity is the same for all three flavors at the higher energies. Figure 5.9 shows the event weight ($weight1 * weight2$) as a function of $\cos\theta$. Note that $\cos\ \theta = -1$ corresponds to an event coming from directly above, and $\cos\theta = 1$ to an event coming from directly below. There are two competing effects in the weighting. The value of $weight1$ is higher for up-coming events, since they have longer chords. The value of $weight2$ is higher for downgoing events, since these neutrinos interact near the beginning of their chord. The effect of $weight2$ wins and therefore virtually all sensitivity is from downgoing events. However, it can be seen from Figure 5.9 that there is a tail of events at lower energies which is coming from slightly below

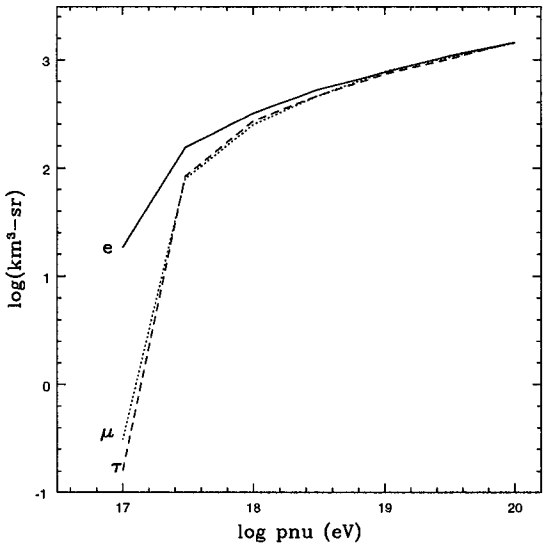

Figure 5.8: The aperture in km^3-sr for electron (solid), muon (dotted) and tau (dashed) neutrinos.

the horizon.

5.3.2 Thermal Trigger Rates

To determine the thermal trigger rates, we use Poisson statistics. We want to calculate the rate of an n-fold coincidence, given individual hit rates (singles rates) Γ and a coincidence window Δt. We assume that one antenna opens a coincidence window, and then we wait for $n-1$ hits in the window. The probability of $\geq n$ hits out of M antennas is therefore the rate at which a single antenna will open up a coincidence window, $M\Gamma$, times the probability of at least $n-1$ hits within the window, $P(\geq n-1)$. As a reminder, given an expected number of events μ within a given time, the probability of n events within that time is

$$P(n|\mu) = \mathrm{e}^{-\mu}\frac{\mu^n}{n!}$$

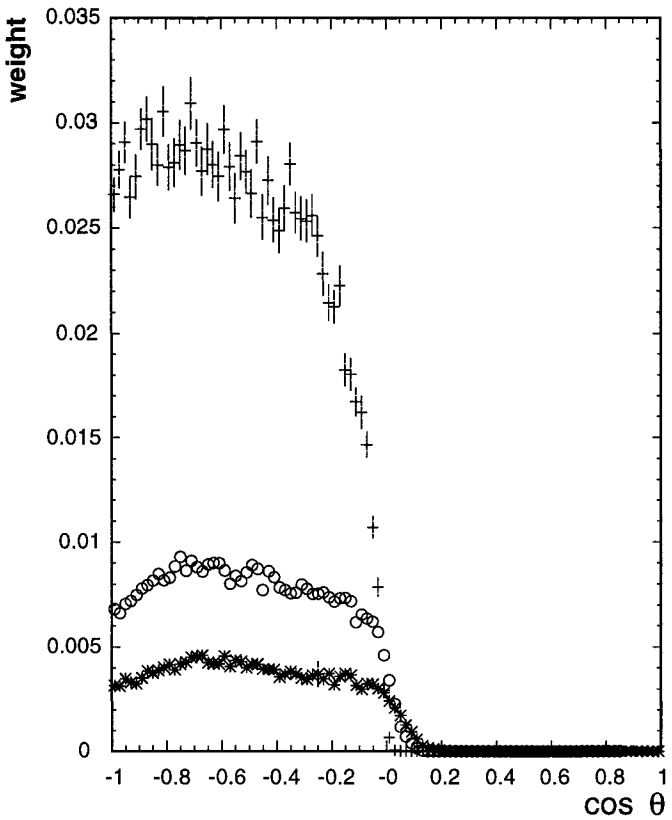

Figure 5.9: Histogram of $weight1 * weight2$ vs. $\cos\theta$ for all hits at 10^{17} eV (stars), 10^{18} eV (circles) and 10^{20} eV (crosses) eV.

First we must determine the singles rate of an individual antenna. We assume two polarization channels (*i.e.* a helical antenna). Each channel has a singles rate $\Gamma = a_m \Delta\nu$, where a_m is the area under the (high) Gaussian tail for $m\sigma$ and $\Delta\nu$ is the bandwidth of the antenna. The rate Γ_1 at which an individual antenna sees a signal above $m\sigma$ in both channels is

$$\Gamma_1 = \Gamma P_1 = \Gamma \mu e^{-\mu}$$

where $\mu = a_m \Delta\nu \times \Delta t$. We take the local coincidence gate Δt to be 20 ns and the bandwidth to be 75 MHz.

The rate of $\geq n$ antennas firing within a global coincidence gate is given by $M\Gamma_1 \times P(\geq n-1)$ as aforementioned. If $n = 1$ then the rate is simply $M\Gamma_1$. Generally speaking, the probability of exactly $n-1$ antennas out of $M-1$ firing is

$$P(n-1) = (1-P_0)^{n-1}(P_0)^{M-n}\binom{M-1}{n-1}$$

where P_0 is the probability that any given antenna does not fire. In the approximation that M is much greater than n and that μ is much less than 1, the probability of $n-1$ antennas firing within the window reduces to

$$P(n-1) = e^{-\mu}\frac{\mu^{n-1}}{(n-1)!}$$

where $\mu = M\Gamma_1 \Delta T$, where ΔT is the global coincidence gate which we take to be 10 μs, and Γ_1 is determined above.

The probability of $\geq n$ antennas firing is then $1 - P(0) - P(1) - ...P(n-1)$.

Figure 5.10 shows the calculated thermal trigger rate for various values of σ and number of hits required. Even with double precision, the MC cannot calculate a nonzero value for 4 or 5 hits at 5σ, so these values are not plotted. A

Table 5.1: Predicted Event Rates per year in a Salt Neutrino Detector

model	WB	TD 1	TD 2	GZK(1)	GZK(2)
number	88	98	126464	76	242

4-fold coincidence at 6σ, the nominal value, would have a thermal trigger rate of essentially zero. If the threshold is reduced to 4σ, then the thermal coincidence rate is 25 nHz (less than 1 per year) for 4-fold coincidence and 69 μHz for a 3-fold coincidence. Other effects will probably limit the trigger rate.

It should be noted that lowering the threshold gives us significant improvement in sensitivity at low energies. The aperture (for electron neutrinos) is 17 km^3-sr at 10^{17} eV for a 4-fold 6σ coincidence. The aperture increases to 78 km^3-sr for a 4-fold 4σ coincidence, and 102 km^3-sr for a 3-fold 4σ coincidence. At the highest energies there is only about a 10% difference because the trigger efficiency is already high.

5.3.3 Predicted Event Rates at SALSA

Table 5.1 shows the predicted numbers from the WB bound [14], topological defects [15] and the GZK flux [16] for 3 years of livetime with SALSA. In particular, the GZK model [16] shows at least 76 neutrinos per year.

5.4 Conclusions

A neutrino telescope in a salt dome would have a low enough energy threshold to be sensitive to the most likely fluxes of EHE neutrinos. Such an experiment would be background-free and could in principle have a 100% duty cycle. The

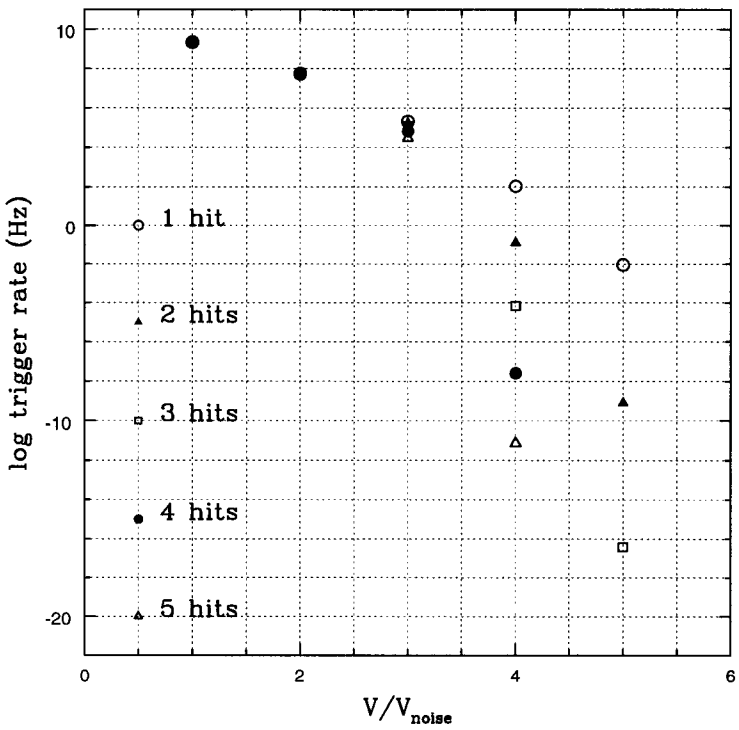

Figure 5.10: The expected thermal trigger rate plotted against the signal significance required for a hit, with separate curves depending on the number of hits required.

experiment should see a large number of GZK neutrinos, even assuming a low GZK flux, in a single year of running. The experiment also has better angular resolution, since the polarization information is sensitive to the relative orientation of the antenna and the neutrino direction (see Section 2.2.5).

CHAPTER 6

Overall Conclusions and Status of Radio Neutrino Detection

The Askar'yan effect has been demonstrated to exist with the expected properties of coherence, 100% linear polarization, the expected absolute energy scale and band-limited pulse structure. The GLUE experiment utilized the Askar'yan effect to set upper limits on top-down models for EHE neutrino production, as well as providing valuable experience with radio hardware and Monte Carlo techniques which will be used on future experiments. We have measured an attenuation length at the Hockley salt dome of more than 300 m, which would make the site or a similar formation suitable for a cubic kilometer detector array. The salt dome array would have an excellent chance of seeing GZK neutrinos in a year of livetime, with no background.

The next radio-based experiment will be the Antarctic Transient Impulsive Antenna (ANITA) [61]. In this experiment, balloon-borne radio antennas search for coherent Cherenkov pulses from neutrinos interacting in the Antarctic ice sheet. Because the balloon flies at an altitude of about 40 km, it has a lower energy threshold than GLUE. ANITA is sensitive to about 10 times more raw volume than GLUE since the Antarctic ice sheet is 3 km thick compared the 10–20 m thickness of the regolith. Also, ANITA will accrue about 10 times more livetime than GLUE in three flights. ANITA is sensitive to the GZK flux and

should see 4–10 GZK neutrinos in three flights.

Figures 6.1,6.2, and 6.3 show the volumetric aperture multiplied by the livetime (or estimated livetime for future and ongoing experiments) for RICE, GLUE, ANITA, and SALSA, for electron, muon and tau neutrinos respectively. The figures also show the aperture of IceCube, an optical experiment using PMTs buried in the Antarctic ice, and Figure 6.3 shows the aperture of Auger, which is sensitive to tau neutrinos only. IceCube and SALSA access complementary energy regimes, since more power is carried in the radio at high energies than at low.

In conclusion, proposed radio-based neutrino telescopes should be able to see neutrinos from the GZK flux using the radio technique within 10 years of this writing.

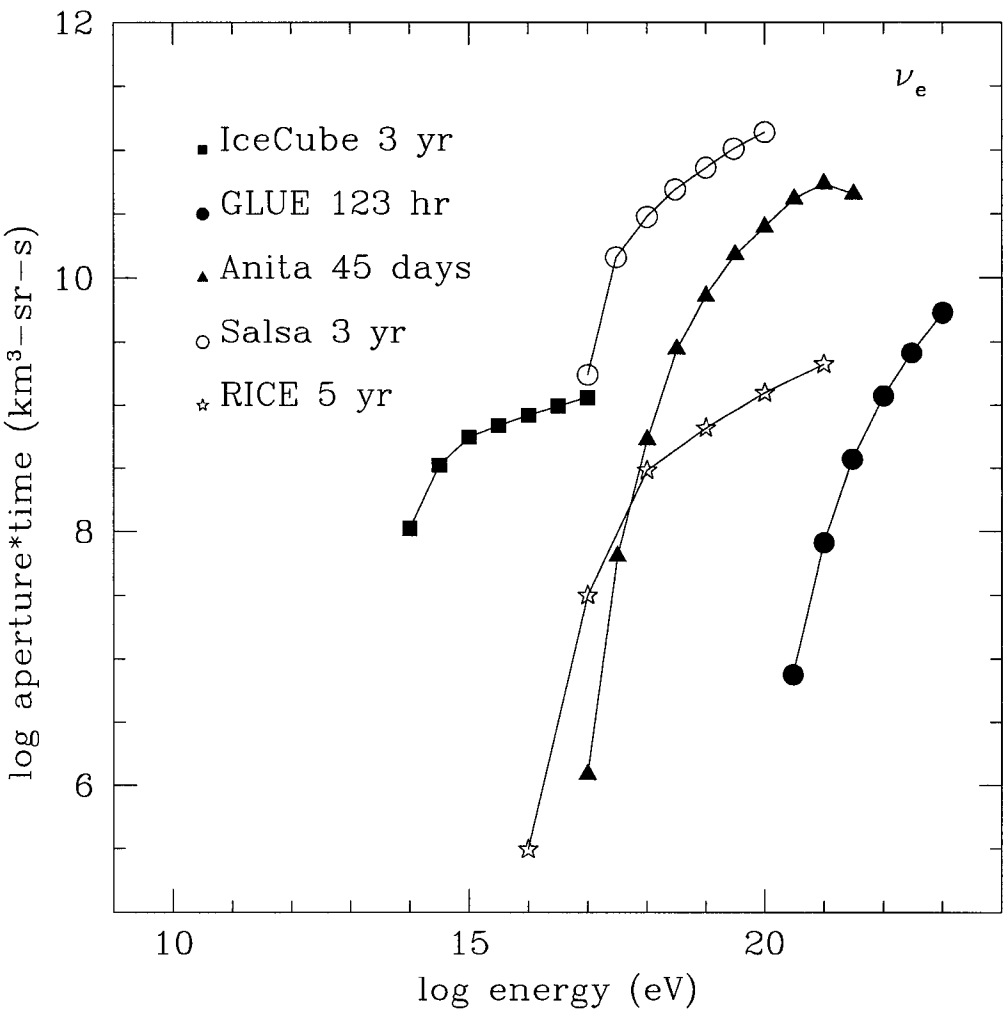

Figure 6.1: Volumetric aperture times livetime for five experiments. Squares: IceCube. Filled circles: GLUE. Triangles: ANITA. Open circles: SALSA. Stars: RICE. Figure is for electron neutrinos only.

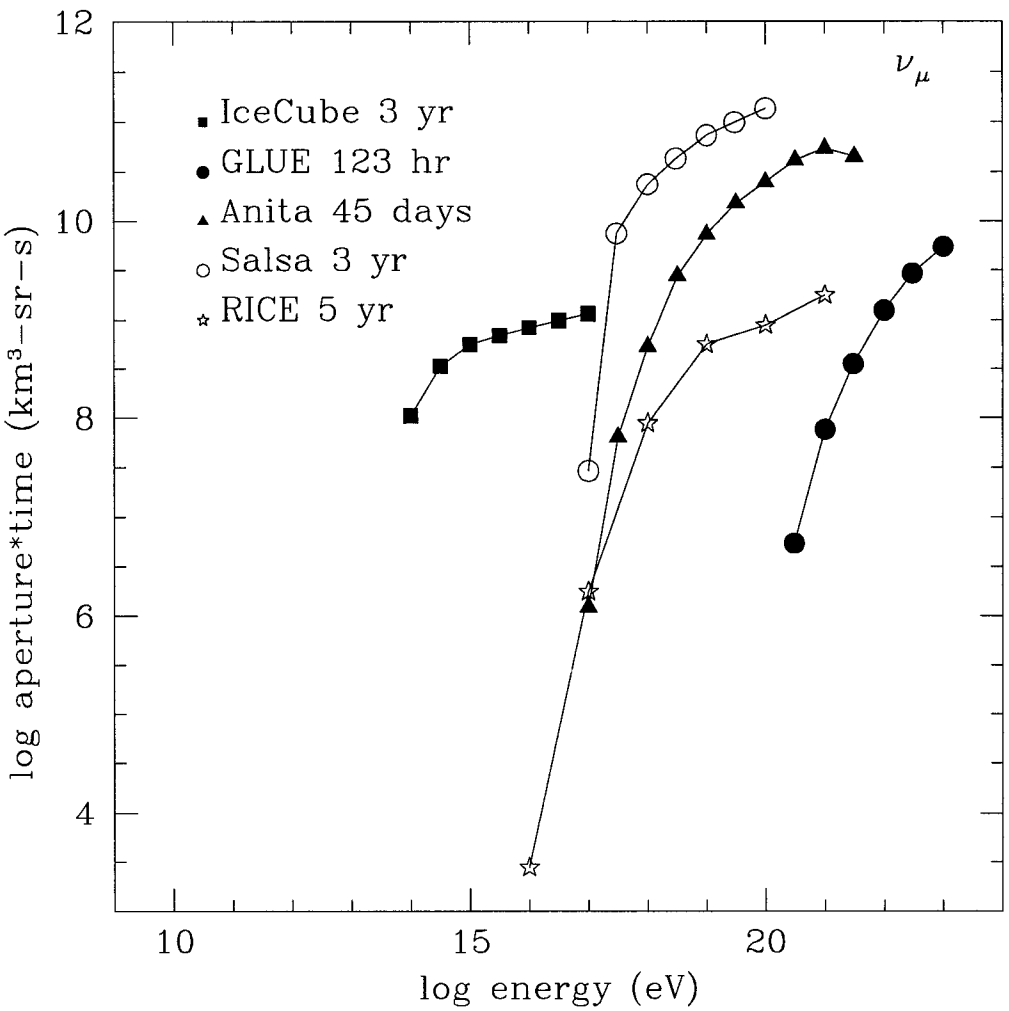

Figure 6.2: Volumetric aperture times livetime for five experiments. Squares: IceCube. Filled circles: GLUE. Triangles: ANITA. Open circles: SALSA. Stars: RICE. Figure is for muon neutrinos only.

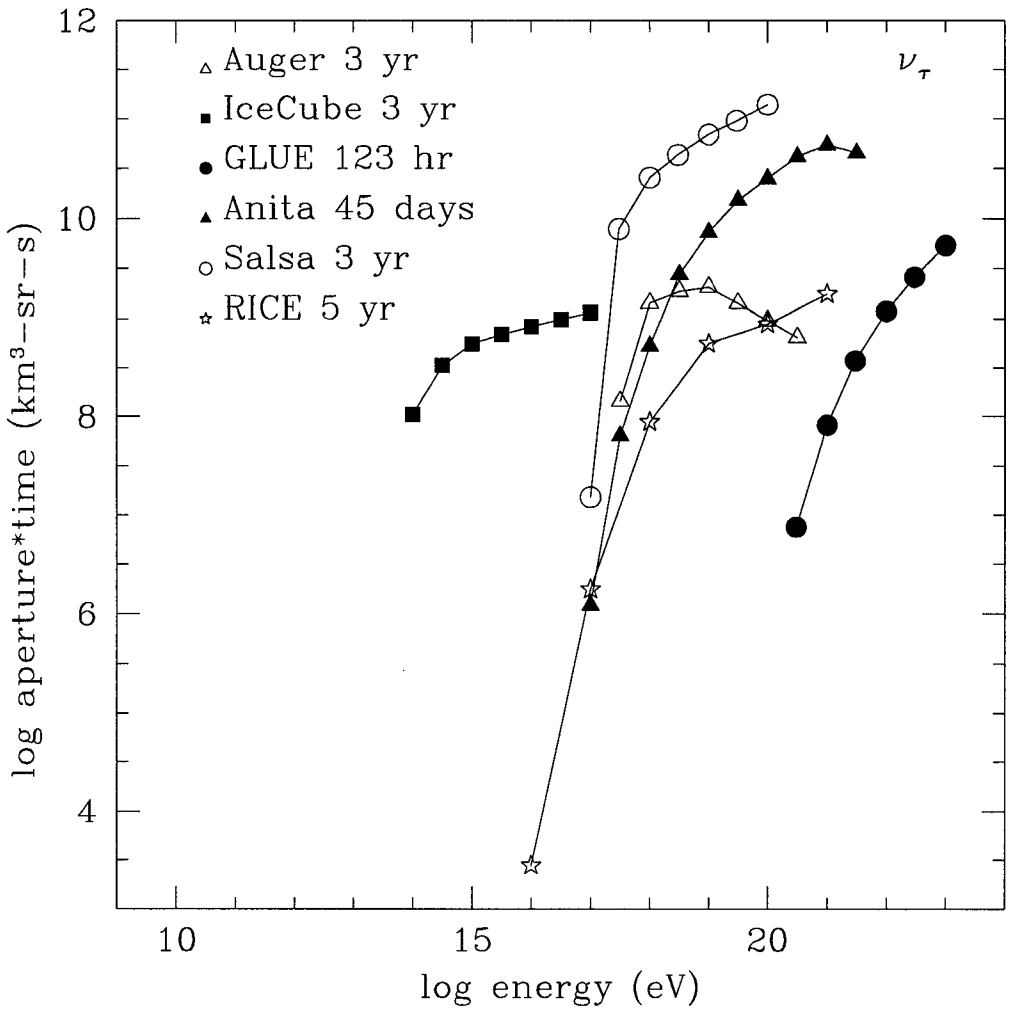

Figure 6.3: Volumetric aperture times livetime for five experiments. Squares: IceCube. Filled circles: Auger: Open triangles. GLUE. Triangles: ANITA. Open circles: SALSA. Stars: RICE. Figure is for tau neutrinos only.

APPENDIX A

Fresnel Coefficient for a Spherical Wave

For the GLUE Monte Carlo, we need to understand the behavior of an electric field from a Cherenkov cone passing through a dielectric boundary. First I review the Fresnel coefficients for the "textbook" plane wave case. Then I discuss the behavior of rays from a point source, using ray-tracing to parameterize the actual behavior of the wave.

A.1 Fresnel Coefficients

The boundary conditions of Maxwell's equations dictate the change in the amplitude of an electric field passing through a dielectric boundary. For full discussion see, for example, Born and Wolf [52] §1.5.3, Griffiths [53] § 8.2.5, and Marion [54] § 6.3. The ratio of transmitted to incident electric field, $E_T/E_I = t$, is given for two cases: when the electric field is parallel to the plane of incidence ($t_{||}$) and when the electric field is perpendicular to the plane of incidence ($t_{\perp}$). Because the plane of incidence is perpendicular to the plane of the boundary, $t_{||}$ is somewhat confusingly called the "pokey" case, since it intersects the boundary at only one point, whereas $t_{\perp}$ is called the "slappy" case. The two cases are illustrated in Figure A.1.

These are the Fresnel transmission coefficients:

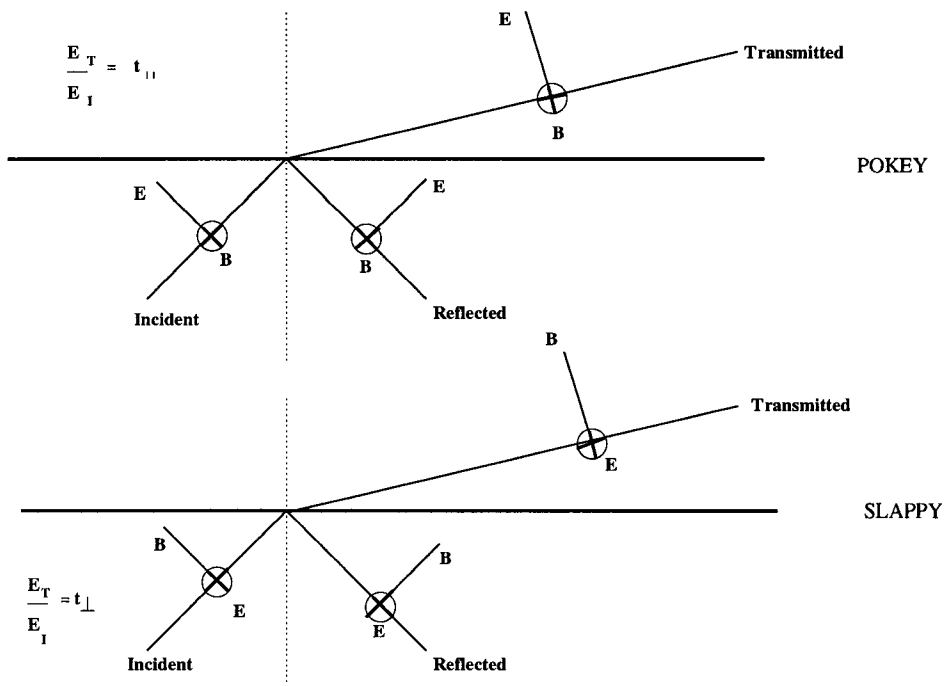

Figure A.1: Diagram of electric field for "pokey" and "slappy" cases, and the corresponding Fresnel transmission coefficients. The plane of incidence is the plane of the page. Note that for the "pokey" case the Fresnel transmission coefficient is $t_{||}$ and for the "slappy" case the coefficient is $t_{\perp}$.

$$t_{\|} = \frac{2\sin\theta_T \cos\theta_I}{\sin(\theta_I + \theta_T)\cos(\theta_I - \theta_T)} \tag{A.1}$$

$$t_{\perp} = \frac{2\sin\theta_T \cos\theta_I}{\sin(\theta_I + \theta_T)} \tag{A.2}$$

The corresponding reflection coefficients ($r = E_R/E_I$) are

$$r_{\|} = \frac{\tan(\theta_I - \theta_T)}{\tan(\theta_I + \theta_T)} \tag{A.3}$$

$$r_{\perp} = \frac{\sin(\theta_I - \theta_T)}{\sin(\theta_I + \theta_T)} \tag{A.4}$$

The angles θ are between the normal of the boundary and the direction of propagation; subscript I is the incident field and subscript T is the transmitted or refracted field. Some discussions (including Jackson [55]) use R for the refracted field, but I think this causes unnecessary confusion with the reflected field.

A.2 Intensity Coefficients: Plane Wave Case

The average Poynting flux $\langle S \rangle$ of a monochromatic electromagnetic plane wave, which is the average power per unit area, is given by

$$\langle S \rangle = \frac{1}{2}\sqrt{\frac{\epsilon}{\mu}}|E|^2 \tag{A.5}$$

For the general form of the intensity of a monochromatic electromagnetic wave see Griffiths §8.2.3.

The law of energy conservation requires that the incident power be equal to the reflected and transmitted power. Thus $\langle S_I \rangle A_I = \langle S_R \rangle A_R + \langle S_T \rangle A_T$, where A

is area. Using eq. A.5, assuming that μ doesn't change across the boundary and taking $n = \sqrt{\epsilon}$, we have

$$n_I E_I^2 A_I = n_R E_R^2 A_R + n_T E_T^2 A_T \tag{A.6}$$

Using $n_R = n_I$ and $A_R = A_I$, and dividing through by E_I^2,

$$\frac{E_T^2}{E_I^2} = \frac{n_I A_I}{n_T A_T}\left(1 - \frac{E_R^2}{E_I^2}\right) = \frac{n_I A_I}{n_T A_T}(1 - r_{\|,\perp}^2) \tag{A.7}$$

or

$$\frac{E_T}{E_I} = \sqrt{\frac{n_I A_I}{n_T A_T}(1 - r_{\|,\perp}^2)} \tag{A.8}$$

where $r = r_{\|}$ for the "pokey" case and $r = r_{\perp}$ for the "slappy" case.

The ratio A_I/A_T describes the spreading of the rays after refraction. The rays may spread in two directions: the tangential direction (in the plane of incidence) and the sagittal direction (perpendicular to the plane of incidence). The setup of the problem is analogous to the problem of astigmatism in optics, as shown in Pedrotti [56] §5-5. I take $A_I/A_T = d_I^s d_I^t / d_T^s d_T^t$, where d^s is the sagittal distance and d^t the tangential distance between rays. Note that the distance between two parallel rays does not depend on the distance from the interface.

For parallel rays, there is no change in the sagittal distance. The tangential distance change is exactly equal to $d_I^t/d_T^t = \cos\theta_I / \cos\theta_T$. It can be seen that t and r defined in Equations A.1–A.4 exactly satisfy Eq. A.8.

Figure A.2 shows t as a function of angle for n = 1.73. Note that the electric field strength is greater in the transmitted wave than in the incident wave. The field strength increases because the medium of incidence has a higher index of refraction than the medium of transmission and because the distance between parallel rays decreases after refraction.

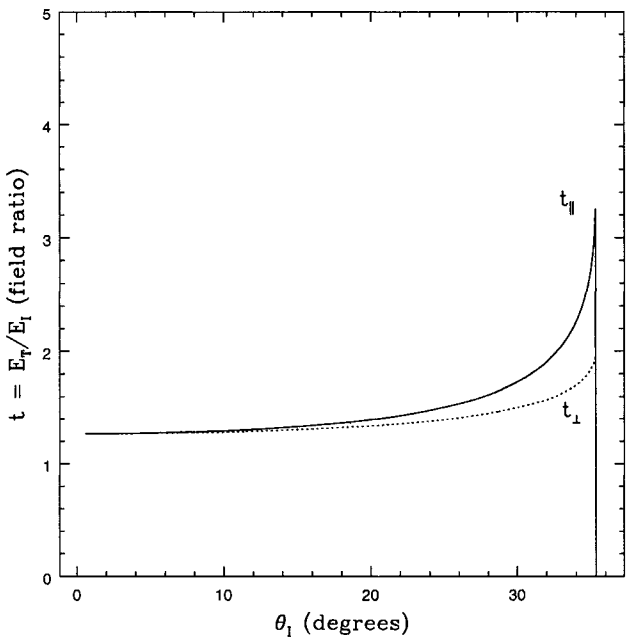

Figure A.2: Electric field ratio E_T/E_I for "pokey" and "slappy" cases, n = 1.73.

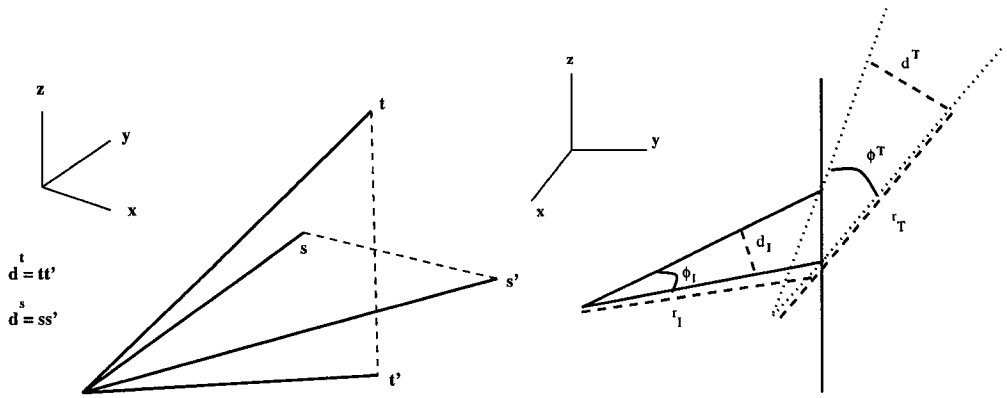

Figure A.3: Left: tangential and sagittal rays. Right: change in distance between tangential rays after refraction.

A.3 Point Source Case

The plane wave case holds for parallel rays. In the MC we assume that the rays originate from one point, spreading out in a cone with an opening angle equal to the Cherenkov angle. The cone also has a thickness of about 1°. Whereas distance between parallel rays decreases after refraction, the distance between rays from a point source increases.

I wrote a small program to trace two rays originating from the same point through an interface. (For the theoretical underpinnings of ray tracing see Hecht [57], §4.2.3.) For simplicity I ignore the intensity modulation over the width of the cone. The index of refraction before the interface is 1.73 and the index of refraction after the interface is 1. The interface is parallel to the x-z plane.

As shown in Figure A.3, the upper and lower (tangential) rays are refracted through the interface. The width of the cone is fixed at 1°, but θ_{cone}, the angle between the axis of the cone and the y-axis, was studied from 0.0 to 0.6163 radians (after which rays totally internally reflect).

I also investigate rays spreading in the x-direction (sagittal) with a width of 1° and a height in z midway between the upper and lower rays. Note that the x and z axes can be arbitrarily rotated so that the rays lie in the x-y or z-y planes.

I define the distance between two rays originating from the same point as the length of a line segment perpendicular to the bisecting ray. The ratio of distances between refracted and un-refracted rays is related to the distance from the interface by referring to the opening angle ϕ between the rays:

$$\frac{d_T}{d_I} = \frac{r_T \tan(\phi_T/2)}{r_I \tan(\phi_I/2)} \tag{A.9}$$

I define the following quantities:

$$\xi^s = \frac{d_T^s r_I}{d_I^s r_T} = \frac{\tan(\phi_T^s/2)}{\tan(\phi_I^s/2)} \tag{A.10}$$

$$\xi^t = \frac{d_T^t r_I}{d_I^t r_T} = \frac{\tan(\phi_T^t/2)}{\tan(\phi_I^t/2)} \tag{A.11}$$

Taking equation 8 and setting $A_I/A_T = d_I^s d_I^t / d_T^s d_T^t$,

$$\frac{E_T}{E_I} = \sqrt{\frac{n_I}{n_T}\frac{d_I^s d_I^t}{d_T^s d_T^t}(1 - r_{\parallel,\perp}^2)} \tag{A.12}$$

Multiplying the equation by r_T/r_I,

$$\frac{E_T r_T}{E_I r_I} = \sqrt{\frac{n_I}{n_T}\frac{d_I^s r_T}{d_T^s r_I}\frac{d_I^t r_T}{d_T^t r_I}(1 - r_{\parallel,\perp}^2)} = \sqrt{\frac{n_I}{n_T}\frac{1 - r_{\parallel,\perp}^2}{\xi^s \xi^t}} \tag{A.13}$$

Table A.1 lists the values of ξ^s and ξ^t for GLUE. In the GLUE MC we always use the "pokey" case, $r = r_{\parallel}$. The ratio $E_T r_T / E_I r_I$ decreases with increasing angle, because of the increase in areas after refraction.

Table A.1: Behavior with respect to incidence angle for GLUE for the "pokey" case.

angle (radians)	ξ^t	ξ^s
0.001	1.73	1.49
0.10	1.75	1.48
0.20	1.81	1.46
0.30	1.93	1.42
0.40	2.18	1.37
0.5	2.80	1.30
0.52	3.06	1.29
0.54	3.43	1.27
0.56	4.03	1.26
0.58	5.25	1.24
0.585	5.81	1.24
0.588	6.27	1.23
0.590	6.65	1.23
0.592	7.13	1.23
0.595	8.16	1.23

A.4 Comparison with Analytical Form

Consider Eq. A.8. If A is replaced with the area of a spherical wave front, $A = r^2 d\Omega$, then Eq. A.8 becomes

$$\frac{E_T}{E_I} = \sqrt{\frac{n_I r_I^2 d\Omega_I}{n_T r_T^2 d\Omega_T}(1 - r_{\parallel,\perp}^2)} \tag{A.14}$$

Pulling the r factors to the left side,

$$\frac{E_T r_T}{E_I r_I} = \sqrt{\frac{n_I d\Omega_I}{n_T d\Omega_T}(1 - r_{\parallel,\perp}^2)} = \sqrt{\frac{n_I \sin\theta_I d\theta_I d\phi_I}{n_T \sin\theta_T d\theta_T d\phi_T}(1 - r_{\parallel,\perp}^2)} \tag{A.15}$$

Assuming that $d\phi$ does not change and differentiating Snell's law to obtain $d\theta_I/d\theta_T$,

$$\frac{E_T r_T}{E_I r_I} = \sqrt{\frac{\tan\theta_I}{\tan\theta_T}(1 - r_{\parallel,\perp}^2)} \tag{A.16}$$

which is the analytic form obtained by Dave Seckel (private communication).

Looking at the ray-tracing form of Eq. A.13, one can consider the sagittal ratio ξ^s to be $d\phi_T/d\phi_I$ and the tangential distance ratio ξ^t to be $\sin\theta_T d\theta_T / \sin\theta_I d\theta_I$. This is approximately true for small angles, since $\tan\phi \approx \phi$ for small ϕ. Then you recover the form of Eq. A.15.

Figure A.4 shows the analytical form and the form obtained from ray-tracing. They agree to within about 10%. The ray-tracing provides only a rough estimate of the area (as a square, rather than a segment of a sphere) which probably accounts for the difference. There may also be a difference related to the fact that sagittal rays spread, but $d\phi$ is assumed to be constant through the boundary, so the forms are not exactly equivalent. However, for a source that is much closer to the interface than the detector (definitely true for GLUE), the rays appear to exit the surface from one point, and one can always rotate into the appropriate ϕ, so the analytic form should hold.

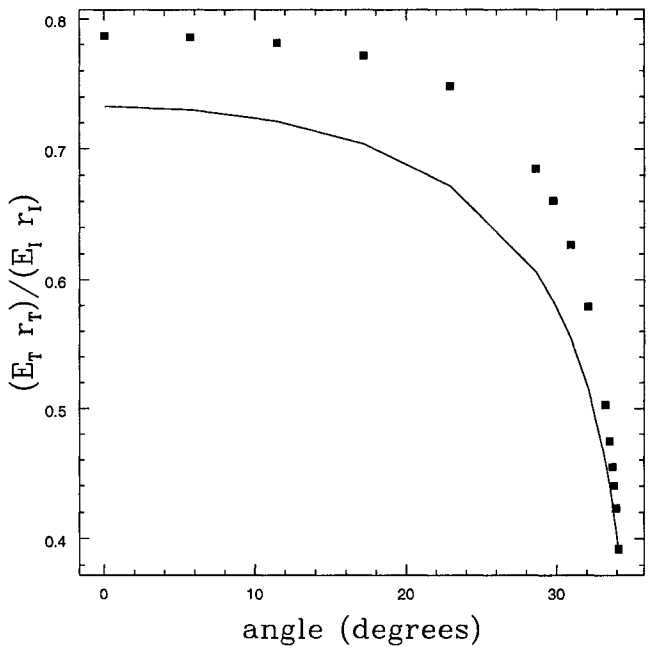

Figure A.4: Analytic form (solid line) and form from ray tracing (dots), for n = 1.73.

References

[1] L. Bergstrom and A. Goodbar, *Cosmology and Particle Physics*, John Wiley and Sons in conjunction with Praxis Publishing, West Sussex, England (1999).

[2] L. Drury, Rep. Prog. Phys. 46, 973 (1983) and R. Blandford & D. Eichler, Phys. Rept. 154, 1 (1987).

[3] J. Zweerink *et al.* (for WHIPPLE), ApJ 490, L141 (1997) and F. Aharonian *et al.* (for HEGRA), Astron. & Astrophys. 327, L5 (1997).

[4] For acceleration of protons see K. Mannheim, Astron. & Astrophys. 267, 67 (1993). For acceleration of electrons see C. Dermer and R. Schlickeiser, Science 257, 1642 (1992).

[5] G. Fishman and C. Meegan, Ann. Rev. Astron. Astroph., 33, 415 (1995).

[6] M. Metzger *et al.*, Nature, 387, 879 (1997)

[7] K. Stanek *et al.*, ApJ 591, L17 (2003).

[8] M. Kamionkowsky and A. Kosowsky, Ann. Rev. Nucl. Part. Phys., 49, 77 (1999).

[9] R. Protheroe and T. Stanev, PRL 77, 18 (1996).

[10] P. Bhattacherjee and G. Sigl, Phys.Rept. 327, 109-247 (2000).

[11] K. Greisen, Phys. Rev. Lett. 16, 748 (1966); G. Zatsepin and V. Kuzmin, JETP Lett. 4, 78 (1966).

[12] H. Dai and S. Yoshida, J.Phys. G24, 905-938 (1998).

[13] http://www.auger.org/

[14] J. Bahcall and E. Waxman, Phys.Rev. D59, 023002 (1999).

[15] S. Yoshida *et al.*, Phys.Rev.Lett. 81, 5505-5508 (1998); and R. Protheroe & T. Stanev, Phys.Rev.Lett. 77, 3708-3711 (1996).

[16] R. Engel, D. Seckel and T. Stanev, Phys.Rev. D64, 093010 (2001).

[17] Cross sections from K. Nakamura *et al.*, Nucl.Phys. A721 (2003) 549-552. Flux from J. Bahcall and C. Peña-Garay, hep-ph/0404061.

[18] Cross section from P. Lipari, Nucl.Phys.Proc.Suppl. 112, 274-287 (2002). Flux from Y. Liu, L. Derome and M. Buenerd, Phys.Rev. D67, 073022 (2003).

[19] R. Gandhi, Nucl.Phys.Proc.Suppl. 91, 453-461 (2000).

[20] http://antares.in2p3.fr/antares/antares.html

[21] J. Blanco-Pillado, R. Vazquez and E. Zas, Phys. Rev. Lett. 78, 3614 (1997).

[22] http://amanda.berkeley.edu

[23] http://icecube.wisc.edu/

[24] G. Askar'yan, Soviet Physics JETP 14, 441 (1962); G. Askar'yan, Soviet Physics JETP 21, 658 (1965).

[25] H. Allen, Prog. in Elem. Part. and Cosmic Ray Physics 10, 171 (1971).

[26] P. Gorham, D. Saltzberg, & P. Schoessow *et al.*,Phys. Rev. E62, 8590 (2000).

[27] G. Frichter *et al.*, Phys. Rev. D 53, 1684 (1996); D. Besson *et al.*, Proc. 26th Intl. Cosmic Ray Conf. v.2, 467 (1999). See also the RICE website at http://kuhep4.phsx.ukans.edu/~riceman/index.html.

[28] K. Kamata, & J. Nishimura, 1958, Suppl. Progr. Theoret. Phys. 6, 93; K. Greisen., 1965, in Prog. Cosmic Ray Physics vol. III, J.G. Wilson ed., (North Holland: Amsterdam) 1.

[29] F. Halzen, T. Stanev and E. Zas, Phys. Rev. D 45, 362 (1992); Alvarez-Muniz, Vasquez and Zas, Phys. Rev. D 62, 063001 (2000).

[30] K. Rohlfs and T. Wilson, *Tools of Radio Astronomy*, 3rd ed. Berlin: Springer-Verlag (2000).

[31] V. L. Ginzburg and V. N. Tsytovich, *Transition Radiation and Transition Scattering*, (New York: Adam Hilger Press), 1990.

[32] T. Takahashi *et al.*, Phys. Rev. E **50**, 4041 (1994).

[33] Y. Shibata *et al.*, Phys. Rev. E50, 1479 (1994).

[34] D. Morrison & T. Own, 1987 *The Planetary System*, (Addison-Wesley: Reading,MA).

[35] G. Olhoeft & D. Strangway, 1975, Earth Plan. Sci. Lett. 24, 394.

[36] J. Alvarez-Muniz and E. Zas, Proceedings of First International Workshop on Radio Detection of High Energy Particles, AIP # 579, p.128.

[37] R. Dagkesamanskii, & I. Zheleznyk, 1989, JETP 50, 233.

[38] T. Hankins, R. Ekers & J. O'Sullivan, 1996, MNRAS 283, 1027.

[39] N. Soboleva, "Measurement of the polarization of lunar radio emission on a wavelength of 3.2 cm", Soviet astronomy - AJ, 6 (6), 873, (1963)

[40] C. Heiles and F. Drake, "The polarization and intensity of thermal radiation from a planetary surface", Icarus 2, 281 (1963).

[41] 2001 Astronomical Almanac.

[42] E. Fomalont and M. Wright, "Interferometry and Aperture Synthesis", in "Galactic and Extra-Galactic Astronomy", 1st edition, 1974.

[43] http://dsnra.jpl.nasa.gov/Antennas/Antennas.html

[44] P. Gorham, K. Liewer, C. Naudet, D. Saltzberg & D. Williams, Proceedings of First International Workshop on Radio Detection of High Energy Particles, AIP # 579, p.177.

[45] B. Smith, Journal of Geophysical Research, 72, 16 (1967).

[46] J. Foley, A. van Dam, S. Feiner and J. Hughes, Computer Graphics: Principles and Practice, 2nd Ed., 1996, p.756-758.

[47] R. Gandhi *et al.*, Astropart.Phys. 5, 81-110 (1996).

[48] Review of Particle Physics, Particle Data Group (1998) p.169.

[49] J. Alvarez-Muniz *et al.*, Phys.Rev. D62 (2000) 063001.

[50] J. Alvarez-Muniz and E. Zas, Phys.Lett. B434 (1998) 396-406.

[51] J. Alvarez-Muniz and E. Zas, Phys.Lett. B411 (1997) 218-224.

[52] M. Born and E. Wolf, Principles of Optics, 4th edition.

[53] D. Griffiths, Introduction to Electrodynamics, second edition.

[54] M. Heald and J. Marion, Classical Electrodynamic Radiation, second edition.

[55] J. Jackson, Classical Electrodynamics, third edition.

[56] F. Pedrotti and L. Pedrotti, Introduction to Optics, second edition.

[57] E. Hecht, Optics, second edition.

[58] M. Chiba *et al.*, Proceedings of First International Workshop on Radio Detection of High Energy Particles, AIP # 579.

[59] http://www.wipp.carlsbad.nm.us

[60] J. Kraus, *Antennas* 2nd ed., McGraw-Hill, Boston (1988).

[61] http://www.ps.uci.edu/~anita/index.html